

TNO Defence Research

TI  
Le TD 94-0176

0

Phone +31 70 326 42 21

TNO-report  
FEL-94-B062

copy no.

title:

Analysis & synthesis of (SAR) waveguide phased array  
antennas  
(ESA contract no. 10134/93/NL/PB)

**AD-A285 336**

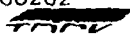


DTIC  
ELECTE  
OCT 05 1994

S D

**TDCK RAPPORTENCENTRALE**

Frederikkazerne, gebouw 140  
v/d Burchlaan 31 MPC 16A  
TEL. : 070-3166394/6395  
FAX. : (31) 070-3166202  
Postbus 90701



TNO Defence Research

TI  
L: TD 94-0170

Oude Waalsdorperweg 63  
2597 AK The Hague  
P O Box 96864  
2509 JG The Hague  
The Netherlands

Fax +31 70 328 09 61  
Phone +31 70 326 42 21

0

TNO-report  
FEL-94-B062

copy no.:

title:

Analysis & synthesis of (SAR) waveguide phased array  
antennas  
(ESA contract no. 10134/93/NL/PB)

author(s):

H.J. Visser

date:

February 1994

**TDCK** RAPPORTCENTRALE

Frederikkazerne, gebouw 140  
v/d Burchlaan 31 MPC 16A  
TEL.: 070-3166394/6395  
FAX.: (31) 070-3166202  
Postbus 90701  
2509 LS Den Haag **TDCK**

classification

classified by : G.A. van der Spek

classification date : February 1, 1994

title : Ongerubriceerd

managementuittreksel : Ongerubriceerd

abstract : Ongerubriceerd

report text : Ongerubriceerd

appendix A : Ongerubriceerd

no. of copies : 30

no. of pages : 116 (incl. appendix,  
excl. RDP & distribution list)

no. of appendices : 1

All information which is classified according to Dutch regulations shall be treated by the recipient in the same way as classified information of corresponding value in his own country. No part of this information will be disclosed to any party.

The classification designation Ongerubriceerd is equivalent to Unclassified, Stg. Confidentieel is equivalent to Confidential and Stg. Geheim is equivalent to Secret.

A-1

All rights reserved.  
No part of this publication may be reproduced and/or published by print, photoprint, microfilm or any other means without the previous written consent of TNO.

In case this report was drafted on instructions, the rights and obligations of contracting parties are subject to either the 'Standard Conditions for Research Instructions given to TNO', or the relevant agreement concluded between the contracting parties.

Submitting the report for inspection to parties who have a direct interest is permitted.

© TNO

94-31721  


Netherlands organization for applied scientific research

TNO Defence Research consists of the TNO Physics and Electronics Laboratory, the TNO Prins Maurits Laboratory and the TNO Institute for Perception



The Standard Conditions for Research Instructions given to TNO, as filed at the Registry of the District Court and the Chamber of Commerce in The Hague shall apply to all instructions given to TNO

## MANAGEMENTUITTREKSEL

titel : Analysis & synthesis of (SAR) waveguide phased array antennas  
(ESA contract no. 10134/93/NL/PB)

auteur(s) : Ir. H.J. Visser

datum : februari 1994

opdrachtnr. : -

IWP-nr. : 710

rapportnr. : FEL-94-B062

Dit rapport beschrijft methoden voor de analyse en synthese van golfpijp phased array antennas alsmede enkele ontwerpen van C-band SAR dubbel gepolariseerde golfpijp phased array antennas. Analyse en synthese kunnen gebruikt worden voor enkel gepolariseerde (rechthoekige) golfpijp phased array antennas alsmede voor dubbel gepolariseerde (vierkante) golfpijp phased array antennas. Analyse en synthese staan de aanwezigheid van irissen in de golfpijp uitmondungen en de aanwezigheid van een dielektrische plaat voor de antenne apertuur toe. Irissen en dielektrische plaat worden toegepast voor Wide Angle Impedance Matching.

De gerapporteerde werkzaamheden vloeien voort uit werkpakket 1000 van ESA contract Nr. 10134/93/NL/PB.

Begonnen wordt met een literatuurstudie gewijd aan dubbel gepolariseerde golfpijpstralers, resulterend in de keuze van de vierkante open golfpijp. Na een grondige beschrijving van de mode matching analysemethode voor een oneindige golfpijp array - eindigheidseffecten inbegrepen-, die de basis vormt van al de verder beschreven analyse- en synthese-methoden, wordt de nauwkeurigheid van de analyse software gevalideerd middels vergelijk met metingen aan twee gerealiseerde antennas. Deze antennas bevatten gecentreerde irissen in de golfpijputmondungen en een dielektrische plaat voor de antenne apertuur voor impedantie-aanpassingsdoeleinden. Een antennasynthesemethode, gebruik makend van simulated annealing en downhill simplex technieken, wordt vervolgens beschreven en verschillende antenne-ontwerpen, gebaseerd op een enkel element in een oneindige array omgeving, worden gepresenteerd. Deze ontwerpen zijn gesynthetiseerd met en zonder de aanwezigheid van een aanpassingsstructuur en voor rechthoekige alsmede driehoekige array roosters. Vervolgens worden de ontwerpen van subarrays gepresenteerd die alle voldoen aan de door ESA gegeven en in het rapport genoemde specificaties. Getoond wordt het grote belang van het meenemen van de array omgeving in het ontwerp van een subarray. Een microstrip patch golfpijp exciter en een microstrip subarray voedingsnetwerk worden besproken en de diepte van de golfpijpstraler wordt afgeschat. Gekozen is voor de realisatie van een rechthoekig rooster array met golfpijpen van 2,5 cm diepte zonder irissen en zonder dielektrische plaat, gegroepeerd in lineaire 8 elements subarrays.

Deze realisatie zal alleen dan plaatsvinden als ESA, na vergelijk met een concurrerende patch antenne optie - aangeboden door de universiteit van Karlsruhe -, beslist in het voordeel van FEL-TNO. Deze beslissing zal plaatsvinden op review meeting 1, 9 februari 1994.

**CONTENTS**

1	INTRODUCTION	5
2	LITERATURE STUDY ON WAVEGUIDE RADIATORS	7
2.1	Quadruple-ridge loaded waveguides	7
2.2	Wheeler lab square waveguide	8
2.3	Open-ended square waveguide	8
3	ANTENNA ANALYSIS TOOLS	9
3.1	Mode matching	9
3.2	Antenna geometry	9
3.3	Electromagnetic field representation	11
3.4	Transfer properties & matching	19
3.5	Finiteness effects	33
4	SOFTWARE VALIDATION	39
4.1	CAISSA antenna	39
4.2	EXPAR test antenna	41
5	ANTENNA SYNTHESIS TOOLS	45
5.1	Simulated annealing	46
5.2	Downhill simplex method	47
5.3	Continuous optimisation by simulated annealing	48
6	BASIC ANTENNA DESIGNS OF CANDIDATE SOLUTIONS	51
6.1	Number of elements in subarray	51
6.2	Rectangular grid with matching structure	53
6.3	Rectangular grid without matching structure	56
6.4	Triangular grid with matching structure	59
6.5	Triangular grid without matching structure	61
7	DESIGN OF THE SUBARRAY	63
7.1	Subarray design strategy	63
7.2	Subarray designs	70
7.3	Choice subarray design	84
8	WAVEGUIDE EXCITER & SUBARRAY FEEDING NETWORK	85
8.1	Preliminary waveguide exciter design	85
8.2	Space qualified waveguide exciter design	88
8.3	Subarray feeding network design	89

9	RADIATING PLANE THICKNESS	95
9.1	Attenuation constant	95
9.2	Attenuation levels	96
9.3	Depth waveguide radiators	98
10	CONCLUDING REMARKS	101
11	ACKNOWLEDGEMENTS	103
12	REFERENCES	105

## APPENDIX A: HELPFUNCTIONS USED IN MATCHING EQUATIONS

## 1 INTRODUCTION

Future spaceborne SAR (Synthetic Aperture Radar) systems should feature wider bandwidth, scanning capability in azimuth and elevation, and above all they should provide full polarisation information because polarimetry is one of the most promising tools for the interpretation of radar signatures.<sup>1</sup>

Current advanced spaceborne SAR systems are not able to acquire the full polarisation matrix and do not have sufficient polarisation purity. Breadboard results from a current state of the art system show only 17 dB polarisation isolation.

New radiating board concepts should therefore be investigated for providing higher polarisation purity, larger bandwidths and low losses fulfilling the necessary electrical and mechanical demands required for space application.

This report describes the development of a high performance waveguide radiating element in an array environment for application in future spaceborne active phased array antennas. Described are the tasks as laid down in workpackage 1100 due to ESA contract no. 10134/93/NL/PB [1]. Key features of the element in the array environment are: Increased signal bandwidth, low ohmic losses, high polarisation purity and utilisation of low mass technology suitable for use in space.

Specifications of the antenna are given by [2, 3]:

- **Number of ports per subarray** : 2 (one per polarisation)
- **Frequency** : 5300 MHz
- **Bandwidth** : 100 MHz (operational)  
± 25 MHz (margin)
- **Scan volume** : ± 15° (elevation)  
± 2° (azimuth)
- **Polarisation** : Dual polarisation  
H and V (baseline) with  
agility (TBC)
- **Co to cross polarisation for each scan direction for each port** : > 20 dB (25 dB goal)
- **Complex ratio of copolarisations for each scan direction after calibration on boresight within** : Modulus ± 0.3 dB  
Phase ± 3°
- **Input reflection coefficient "S<sub>ij</sub>" for each port** : < -15 dB
- **Isolation "S<sub>i,i+1</sub>" between 2 ports of subarray** : > 30 dB
- **Maximum value of "active" reflection coefficient over scan volume for each port** : < -12.5 dB (< -15 dB goal)
- **Absolute copolarisation gain variations over range of polarisation states** : ± 0.4 dB (± 0.3 dB goal)

<sup>1</sup> Polarimetry - a technique used in microwave remote sensing - consists of transmitting horizontally and vertically polarised waves, and measuring both polarisations of the return signal. A target polarisation matrix is formed, and the return from any other incident polarisation could then be readily synthesized. This technique has been used for image enhancement and target discrimination in synthetic aperture radars.

- **Ohmic line loss in subarray** : < 1 dB/m
- **Aperture efficiency<sup>2</sup>** : > 85 % (> 90 % goal)

In order to fulfill these requirements, the design of such an element in an array environment has to be carried out by accurate modelling and not by experimental methods. Experimental design of advanced phased array antennas is a very time consuming and therefore costly process which does not guarantee an optimum solution. Especially when the requirements become more stringent, acceptable designs can hardly be obtained by experimental methods. Good theoretical solutions are needed to make the antenna design simple, accurate and efficient. Computational methods are therefore preferred because they allow the optimisation of the various antenna dimensions and the determination of tolerances in a simple way.

*The emphasis in this report is on the used software tools for the antenna development and the related mathematics because of the paramount importance of accurate software tools for developing future spaceborne SAR phased array antennas.*

This report starts with a literature study on waveguide radiators, resulting in the choice of the open ended square waveguide. After that, a description of the mode matching method used for analysing a single waveguide element in an infinite array environment will be discussed.

The reason for presenting this rather detailed description is given by the importance of this method. All software tools described in this report rely heavily on this mode matching analysis method.

The mode matching analysis yields reflection and transmission coefficients for a single waveguide element in an infinite array environment. Throughout the report, mathematical derivations of other antenna parameters will be given where needed.

After the description of our used analysis method, the report deals with software validation, antenna synthesis tools, first designs of SAR antennas, subarray designs, the design of a waveguide exciter and subarray feeding network and information on the radiating plane thickness.

---

<sup>2</sup> Aperture Efficiency = 
$$\frac{\text{Embedded Subarray Gain at Input Port}}{\frac{4\pi \text{ Subarray Aperture}}{\lambda^2}}$$

## 2 LITERATURE STUDY ON WAVEGUIDE RADIATORS

Of the possible dual polarised antenna elements, the microstrip patch radiator and - to a lesser extent - the open-ended square and circular waveguide radiator are the most commonly encountered ones in the literature.

Other reported dual polarised elements are crossed dipoles [4, 5], printed log-periodic antennas and flared slot (notch) antennas [6].

The problems associated with microstrip patch radiators, i.e. small frequency bandwidth, high losses and high sensitivity to tolerances, both on dimensional and on material parameters, do not exist for waveguide radiators. This is due to the inherent wide bandwidth characteristics of the latter. So waveguide radiators are strong candidates in the design of a spaceborne SAR phased array antenna.

Waveguide radiators known to realise dual polarisation are: Quadruple-ridge loaded waveguides [7], Wheeler lab square waveguide [8], circular open-ended waveguides [9] and square open-ended waveguides [10].

### 2.1 Quadruple-ridge loaded waveguides

The transverse geometry of quadruple-ridged square and circular waveguides is shown in figure 1 [8]:

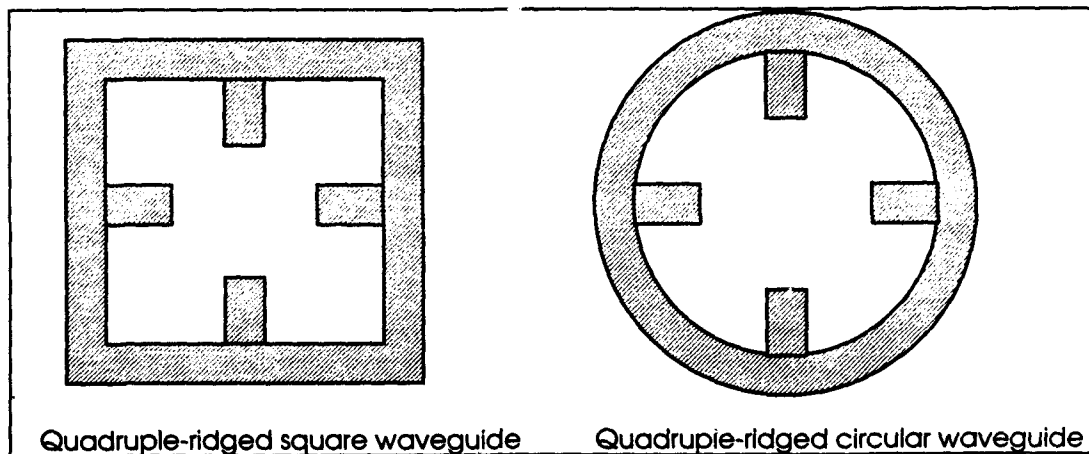


Figure 1: *Transverse geometry of quadruple-ridged square and circular waveguides*

There are two reasons why the quadruple-ridged waveguides are not suitable for our purpose. First: Quadruple-ridged loading of square waveguides does not improve bandwidth and in the case of quadruple-ridged loading of circular waveguides, the bandwidth is only moderately broadened [7]. Second: The method of excitation of the element is extremely difficult to implement at high frequencies, as stated in [8].



## 2.2 Wheeler lab square waveguide

A sketch of the Wheeler lab element is shown in figure 2 [8]:

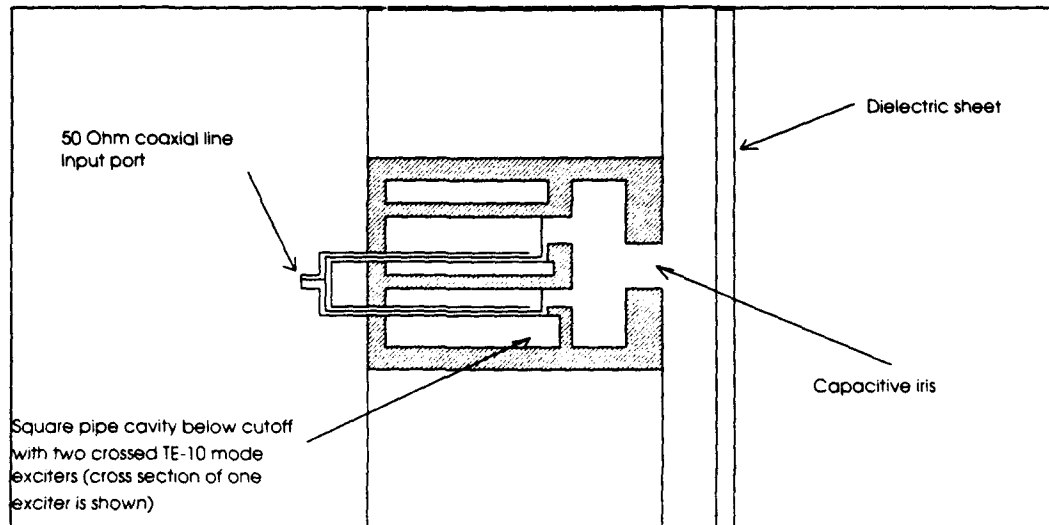


Figure 2: Sketch of Wheeler lab element

This Wheeler lab element is an unloaded square waveguide with aperture dimensions less than  $\lambda_h/2$ , where  $\lambda_h$  is the wavelength at the highest operating frequency.

Due to the reported poor cross polarisation behaviour [8] and the mechanical complexity, this element is not suitable for our purposes.

## 2.3 Open-ended square waveguide

Although, as stated in [9], circular waveguides seem to be the best choice, because of reported better matching characteristics over a scan volume of a 60 degrees half-angle cone, we prefer open-ended square waveguides.

This because of the relatively small scan volume required [1], because a 20 percent bandwidth design has been demonstrated [11], because the ease in construction and because of the long standing experience of TNO-FEL with rectangular waveguides [12], combined with the availability of in house developed accurate software for analysing and synthesising open-ended square and rectangular waveguide phased array antennas.

### 3 ANTENNA ANALYSIS TOOLS

In order to gain knowledge in the field of polarimetric phased array antennas, at TNO-FEL a FORTRAN code for an IBM type Personal Computer is developed to analyse phased array antennas consisting of rectangular or square cross-section open-ended waveguides.

The analysis method described in the following, results in the reflection and transmission coefficients of a single waveguide radiator in an infinite array environment as well as the transverse electromagnetic fields inside and outside the antenna element.

#### 3.1 Mode matching

The waveguide phased array characteristics are determined by assuming that the array is two dimensional infinite with uniform amplitude excitation and linear phase taper, so permitting the use of a unit cell approach, which considerably simplifies the analysis. The unit cell is the smallest area in which the array can be subdivided.

On this unit cell a mode matching method is applied. The field problem is solved at the terminal plane (i.e. the waveguide aperture) by applying the boundary conditions that the tangential components of electric and magnetic fields are continuous across this interface.

First, the representations of the tangential electric field when  $z \downarrow 0$  and  $z \uparrow 0$  are matched to the tangential electric field in the aperture at  $z = 0$ . Next the representation of the tangential magnetic field when  $z \downarrow 0$  is matched to the one as  $z \uparrow 0$ , yielding an infinite system of linear equations which can be solved numerically by truncating it. This results in the unit cell reflection and transmission coefficients.

#### 3.2 Antenna geometry

The array is assumed to be two dimensional infinite and placed in the plane  $z = 0$  of a Cartesian coordinate system  $x, y, z$  (see figure 3):

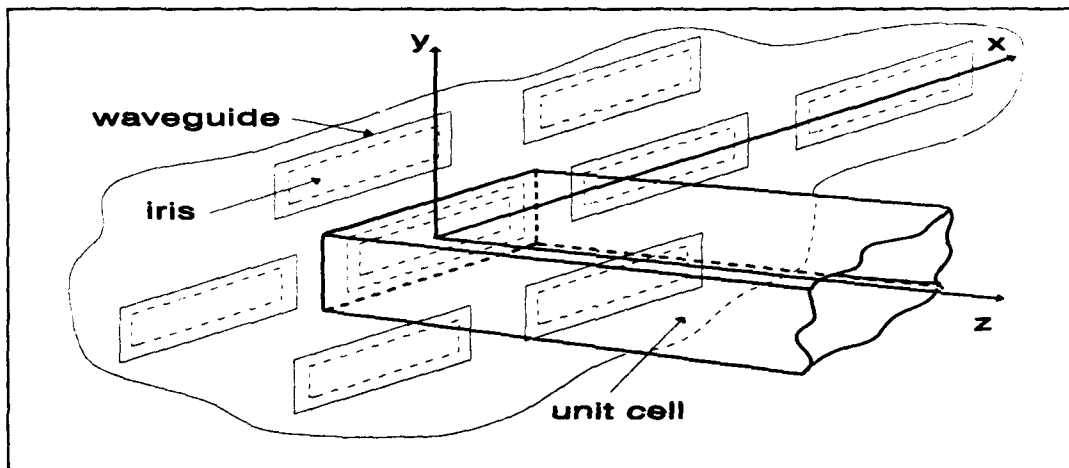


Figure 3: Array configuration

The array elements are waveguides of rectangular or square cross section. Centred irises (used for impedance matching) can be placed in the waveguide apertures. Because of the infiniteness of the structure, edge effects are neglected and due to the periodicity of the configuration, coupling effects are the same for each of the elements, so permitting the assumption of unit cells into which each element individually radiates. The problem has to be solved for a single unit cell only. The geometry of the unit cell is shown in figure 4. This unit cell contains the centre element  $p=0, q=0$  (arbitrary choice).

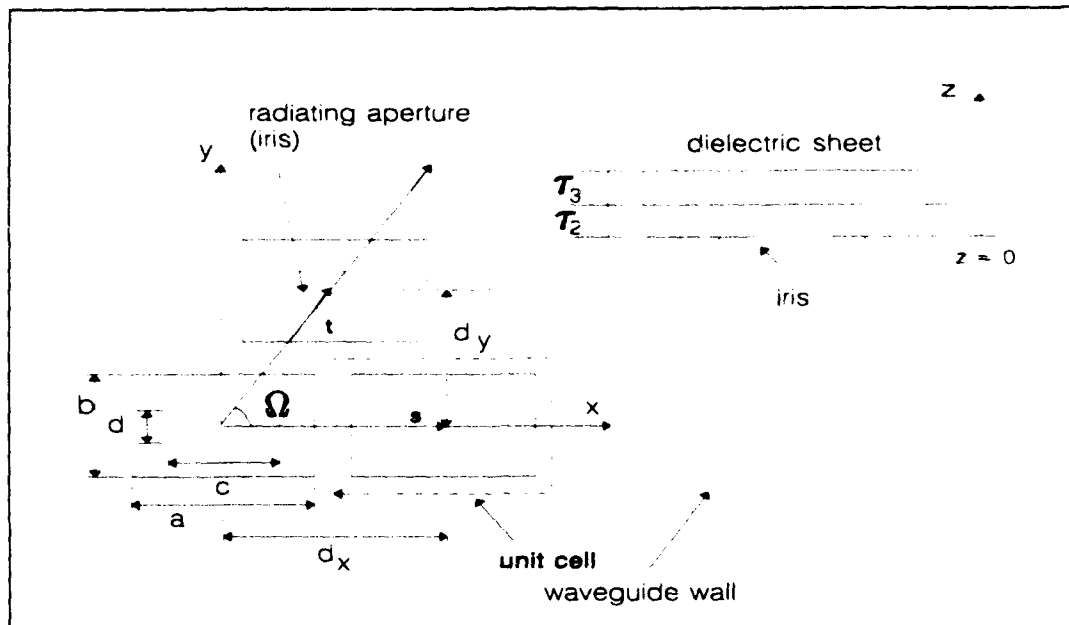


Figure 4: Geometry of array and unit cell

The grid is described by the vectors  $s$  and  $t$ .

In front of the waveguide apertures, a dielectric sheet can be placed. Irises and dielectric sheet are used to compensate for inefficiencies due to coupling effects. A side-view of the unit cell, containing the matching structure, is shown in figure 5.

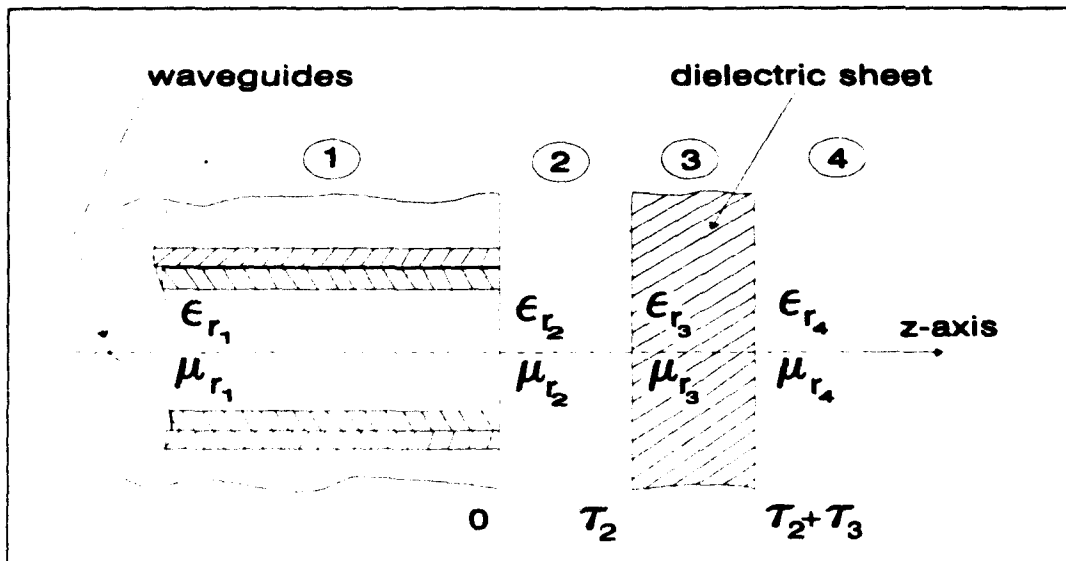


Figure 5: Geometry of dielectric matching structure and surroundings

$\epsilon_r, ; i = 1, 2, 3, 4$  denotes the relative electromagnetic permittivity in the shown subdomains of the antenna.  $\mu_r, ; i = 1, 2, 3, 4$  denotes the relative electromagnetic permeability in the shown subdomains of the antenna.

### 3.3 Electromagnetic field representation

The electromagnetic fields will be described in terms of modes. A complete knowledge of the axial components of a mode is sufficient to determine all field components of this mode. As far as the field equations are concerned, the problem can be separated in scalar problems in the transverse plane.

In the remainder an  $\exp(-j\omega t)$  time dependence is assumed ( $\omega = 2\pi f$ ) and waves propagate according to  $\exp(-jk_z z)$  for increasing  $z$ .  $k_z$  is the axial wavenumber.

For TE-modes, the axial H-field components satisfy the two dimensional Helmholtz equation:

$$(\nabla_T \cdot \nabla_T + k_T^2) h_z^{\pm} = 0 \quad (3.3.1)$$

For TM-modes, the axial E-field components satisfy the two dimensional Helmholtz equation:

$$(\nabla_T \cdot \nabla_T + k_T^2) e_z^{\pm} = 0 \quad (3.3.2)$$

where the subscript T stands for the transversal part of a parameter. So  $k_T$  is the transversal wavenumber.

### 3.3.1 Waveguide modes

The aim of this paragraph is to find solutions for (3.3.1) and (3.3.2) in the waveguide region of the antenna and to derive expressions for the transverse fields.

#### 3.3.1.1 TE-modes

As a solution for (3.3.1) take:

$$h_z^{\pm} = I^{(1)\pm} \cos\left[k_x\left(x + \frac{a}{2}\right)\right] \cos\left[k_y\left(y + \frac{b}{2}\right)\right] \quad (3.3.3)$$

The separation constants  $k_x$  and  $k_y$  are related to the axial wavenumber  $\gamma^{(1)}$  by:

$$k_T^2 = k_x^2 + k_y^2 = \omega^2 \epsilon_0 \mu_0 - \gamma^{(1)2} \quad (3.3.4)$$

with  $\epsilon_0$  and  $\mu_0$  free space electromagnetic permittivity and electromagnetic permeability, respectively.

$I^{(1)\pm}$  are mode amplitude coefficients.

Imposing the boundary conditions leads to:

$$k_{T_{mn}}^2 = \left(\frac{m\pi}{a}\right)^2 + \left(\frac{n\pi}{b}\right)^2; (m, n) \neq (0, 0) \quad (3.3.5a)$$

$$h_{z_{mn}}^{(1)\pm} = I_{mn}^{(1)\pm} \cos\left[\frac{m\pi}{a}\left(x + \frac{a}{2}\right)\right] \cos\left[\frac{n\pi}{b}\left(y + \frac{b}{2}\right)\right] \quad (3.3.5b)$$

The axial wavenumber is given by:

$$Y_{mn}^{(1)} = \begin{cases} \left[ k_0^2 - \left( \frac{m\pi}{a} \right)^2 - \left( \frac{n\pi}{b} \right)^2 \right]^{\frac{1}{2}}, & k_0^2 > \left( \frac{m\pi}{a} \right)^2 + \left( \frac{n\pi}{b} \right)^2 \\ -j \left[ -k_0^2 + \left( \frac{m\pi}{a} \right)^2 + \left( \frac{n\pi}{b} \right)^2 \right]^{\frac{1}{2}}, & k_0^2 < \left( \frac{m\pi}{a} \right)^2 + \left( \frac{n\pi}{b} \right)^2 \end{cases} \quad (3.3.6a)$$

with:

$$k_0 = \omega(\epsilon_0 \mu_0)^{\frac{1}{2}} \quad (3.3.6b)$$

Further:

$$Y_{H_{mn}}^{(1)} = \frac{Y_{mn}^{(1)}}{\omega \mu_0}; Z_{H_{mn}}^{(1)} = \frac{1}{Y_{H_{mn}}^{(1)}} \quad (3.3.7)$$

### 3.3.1.2 TM-modes

Applying the same procedure as in paragraph 3.3.1.1 leads to:

$$k_{Tm}^2 = \left( \frac{m\pi}{a} \right)^2 + \left( \frac{n\pi}{b} \right)^2 \quad (3.3.8a)$$

$$e_{z_{mn}}^{(1)\pm} = \overline{T_{mn}^{(1)\pm}} \sin \left[ \frac{m\pi}{a} \left( x + \frac{a}{2} \right) \right] \sin \left[ \frac{n\pi}{b} \left( y + \frac{b}{2} \right) \right] \quad (3.3.8b)$$

Further:

$$Z_{E_{mn}}^{(1)} = \frac{\gamma_{mn}^{(1)}}{\omega \epsilon_0}; Y_{E_{mn}}^{(1)} = \frac{1}{Z_{E_{mn}}^{(1)}} \quad (3.3.9)$$

with the axial wavenumber given by (3.3.6).

### 3.3.1.3 Transverse field components

The transverse field components of electric and magnetic field strengths are given by [12]:

$$e_{y_{mn}}^{(1)\pm} = \left( \frac{j}{k_{T_{mn}}^2} \right) \left[ \omega \mu_0 \left( \frac{n\pi}{b} \right) I_{mn}^{(1)\pm} \mp \gamma_{mn}^{(1)} \left( \frac{m\pi}{a} \right) \overline{I_{mn}^{(1)\pm}} \right] C_m \left( \frac{x}{a} \right) S_n \left( \frac{y}{b} \right) \quad (3.3.10a)$$

$$e_{x_{mn}}^{(1)\pm} = \left( \frac{j}{k_{T_{mn}}^2} \right) \left[ -\omega \mu_0 \left( \frac{m\pi}{a} \right) I_{mn}^{(1)\pm} \mp \gamma_{mn}^{(1)} \left( \frac{n\pi}{b} \right) \overline{I_{mn}^{(1)\pm}} \right] S_m \left( \frac{x}{a} \right) C_n \left( \frac{y}{b} \right) \quad (3.3.10b)$$

$$h_{x_{mn}}^{(1)\pm} = \left( \frac{j}{k_{T_{mn}}^2} \right) \left[ \pm \gamma_{mn}^{(1)} \left( \frac{m\pi}{a} \right) I_{mn}^{(1)\pm} + \omega \epsilon_0 \left( \frac{n\pi}{b} \right) \overline{I_{mn}^{(1)\pm}} \right] S_m \left( \frac{x}{a} \right) C_n \left( \frac{y}{b} \right) \quad (3.3.10c)$$

$$h_{y_{mn}}^{(1)\pm} = \left( \frac{j}{k_{T_{mn}}^2} \right) \left[ \pm \gamma_{mn}^{(1)} \left( \frac{n\pi}{b} \right) I_{mn}^{(1)\pm} - \omega \epsilon_0 \left( \frac{m\pi}{a} \right) \overline{I_{mn}^{(1)\pm}} \right] C_m \left( \frac{x}{a} \right) S_n \left( \frac{y}{b} \right) \quad (3.3.10d)$$

with:

$$C_i(\xi) \equiv \cos \left[ i\pi \left( \xi + \frac{1}{2} \right) \right]; i = 0, 1, 2, \dots; -\frac{1}{2} < \xi < \frac{1}{2} \quad (3.3.11a)$$

$$S_i(\xi) \equiv \sin \left[ i\pi \left( \xi + \frac{1}{2} \right) \right]; i = 1, 2, 3, \dots; -\frac{1}{2} < \xi < \frac{1}{2} \quad (3.3.11b)$$

### 3.3.2 Fields in the terminal plane

The field distribution in the radiating aperture plays a vital role in the analysis of the configuration and should be chosen carefully. In van Schaik [12], the field is expressed as a complete orthogonal sequence of expansion functions. Two different expansions are described. Since the expansion developed by Lee [13] violates the edge conditions and will limit the permissible iris dimensions (Smolders [14]), we choose an expansion in Chebyshev polynomials that satisfy the edge conditions (but will lead to more CPU time consumption). With this choice, the tangential electric field in the radiating aperture of the centre element is written as:

$$E_x(\text{aperture}) = \sum_{l_w} A_{l_w} CT_l \left( \frac{x}{c} \right) ST_w \left( \frac{y}{d} \right) \quad (3.3.12a)$$

$$E_y(\text{aperture}) = \sum_{l_w} B_{l_w} ST_l \left( \frac{x}{c} \right) CT_w \left( \frac{y}{d} \right) \quad (3.3.12b)$$

with:

$$CT_i(\xi) = \left[ 1 - (2\xi)^2 \right]^{-\frac{1}{2}} \begin{cases} \cos[i \arcsin(2\xi)]; i = 0, 2, 4, \dots \\ -j \sin[i \arcsin(2\xi)]; i = 1, 3, 5, \dots \end{cases} \quad (3.3.13a)$$

$$ST_i(\xi) = \begin{cases} -j \sin[i \arcsin(2\xi)]; i = 2, 4, 6, \dots \\ \cos[i \arcsin(2\xi)]; i = 1, 3, 5, \dots \end{cases} \quad (3.3.13b)$$

and  $A_{l_w}$ ,  $B_{l_w}$  coefficients to be determined.

### 3.3.3 Grating modes in the radiating domain

Due to the periodicity of the array structure, the following relation holds for any Cartesian field component in each sub-domain (see figure 5) located in the region  $z > 0$ .



$$\left\{ e^{(n)z} (r_T + r_{T_n}), h^{(n)z} (r_T + r_{T_n}) \right\} = \left\{ e^{(n)z} (r_T), h^{(n)z} (r_T) \right\} \exp[j(p\Psi_s + q\Psi_t)] \quad (3.3.14)$$

$\Psi_s$  and  $\Psi_t$  denote incremental phase shifts between two adjacent elements in the directions of  $\mathbf{s}$  and  $\mathbf{t}$ , respectively.

### 3.3.3.1 TE-modes

As a solution of (3.3.1) take:

$$h_z^{(n)z} = T^{(n)z} \exp(-j\bar{k}_T \cdot \bar{r}_T) \quad (3.3.15)$$

with:

$$\bar{k}_T = \bar{k}_{T_{pq}} = \bar{b}_1(\Psi_s + 2p\pi) + \bar{b}_2(\Psi_t + 2q\pi) \quad (3.3.16a)$$

$$\bar{b}_1 = \frac{\bar{t} \times \hat{i}_z}{S} \quad (3.3.16b)$$

$$\bar{b}_2 = \frac{\hat{i}_z \times \bar{s}}{S} \quad (3.3.16c)$$

$$S = \hat{i}_z \cdot (\bar{s} \times \bar{t}) \quad (3.3.16d)$$

Each set of values  $p$  and  $q$  specifies a wave component, called a *grating mode*, so:

$$h_{z_{pq}}^{(n)z} = T_{pq}^{(n)z} \exp(-j\bar{k}_{T_{pq}} \cdot \bar{r}_T) \quad (3.3.17)$$

The transverse wave vector corresponding to the direction of scan  $(\theta_0, \varphi_0)$  is given by:

$$\bar{k}_{T_{00}} = k_0 [\sin(\theta_0) \cos(\varphi_0) \hat{i}_x + \sin(\theta_0) \sin(\varphi_0) \hat{i}_y] \quad (3.3.18)$$

The phase shifts can be determined from:

$$\Psi_s = \bar{k}_{T_{0w}} \bullet \bar{s} = k_0 \cdot s \cdot \sin(\theta_0) \cos(\varphi_0) \quad (3.3.19a)$$

$$\Psi_s = k_0 \cdot t \cdot \sin(\theta_0) [\cos(\Omega) \cos(\varphi_0) + \sin(\Omega) \sin(\varphi_0)] \quad (3.3.19b)$$

In Cartesian coordinates:

$$\bar{k}_{T_{pq}} = [(\Psi_s + 2p\pi) / s] \hat{i}_x + [(\Psi_s + 2q\pi) / t \sin(\Omega) - (\Psi_s + 2p\pi) / s \tan(\Omega)] \hat{i}_y \quad (3.3.20)$$

Combining the results:

$$h_{z_{pq}}^{(n)z} = T_{pq}^{(n)z} \exp[-j(u_{p0}x + v_{pq}y)] \quad (3.3.21)$$

with:

$$u_{p0} = k_0 \sin(\theta_0) \cos(\varphi_0) + 2p\pi / s \quad (3.3.22a)$$

$$v_{pq} = k_0 \sin(\theta_0) \sin(\varphi_0) + 2q\pi / t \sin(\Omega) - 2p\pi / s \tan(\Omega) \quad (3.3.22b)$$

The axial wavenumber  $\gamma_{pq}^{(n)}$  is given by:

$$\gamma_{pq}^{(n)} = \begin{cases} (k_0^2 \epsilon_r - u_{p0}^2 - v_{pq}^2)^{\frac{1}{2}}; k_0^2 \epsilon_r > u_{p0}^2 + v_{pq}^2 \\ -j(-k_0^2 \epsilon_r + u_{p0}^2 + v_{pq}^2)^{\frac{1}{2}}; k_0^2 < u_{p0}^2 + v_{pq}^2 \end{cases} \quad (3.3.23)$$

Further:

$$Y_{H_{pq}}^{(n)} = \gamma_{pq}^{(n)} / \omega \mu_0; Z_{H_{pq}}^{(n)} = \frac{1}{Y_{H_{pq}}^{(n)}} \quad (3.3.24)$$

### 3.3.3.2 TM-modes

Analogous to the procedure in paragraph 3.3.3.1:

$$e_{z_{pq}}^{(n)\dagger} = \overline{T_{pq}^{(n)\dagger}} \exp[-j(u_{p0}x + v_{pq}y)] \quad (3.3.25)$$

Further:

$$Z_{E_{pq}}^{(n)} = \gamma_{pq}^{(n)} / \omega \epsilon_r \epsilon_0; Y_{E_{pq}}^{(n)} = \frac{1}{Z_{E_{pq}}^{(n)}} \quad (3.3.26)$$

with the axial wavenumber given by (3.3.23)

### 3.3.3.3 Transverse field components

The transverse components of the electric and magnetic field strengths are given by [10]:

$$e_{x_{pq}}^{(n)\dagger} = \left( -\omega \mu_0 v_{pq} T_{pq}^{(n)\dagger} \mp \gamma_{pq}^{(n)} u_{p0} \overline{T_{pq}^{(n)\dagger}} \right) X_{pq} / k_{T_{pq}}^2 \quad (3.3.27a)$$

$$e_{y_{pq}}^{(n)\dagger} = \left( \omega \mu_0 u_{p0} T_{pq}^{(n)\dagger} \mp \gamma_{pq}^{(n)} v_{pq} \overline{T_{pq}^{(n)\dagger}} \right) X_{pq} / k_{T_{pq}}^2 \quad (3.3.27b)$$

$$h_{x_{pq}}^{(n)\dagger} = \left( \mp \gamma_{pq}^{(n)} u_{p0} T_{pq}^{(n)\dagger} + \omega \epsilon_r \epsilon_0 v_{pq} \overline{T_{pq}^{(n)\dagger}} \right) X_{pq} / k_{T_{pq}}^2 \quad (3.3.27c)$$

$$h_{y_{pq}}^{(n)\dagger} = \left( \mp \gamma_{pq}^{(n)} v_{pq} T_{pq}^{(n)\dagger} - \omega \epsilon_r \epsilon_0 u_{p0} \overline{T_{pq}^{(n)\dagger}} \right) X_{pq} / k_{T_{pq}}^2 \quad (3.3.27d)$$

with:

$$X_{pq} \equiv \exp[-j(u_{pq}x + v_{pq}y)] \quad (3.3.28)$$

### 3.4 Transfer properties & matching

For analysing the electromagnetic properties of the dielectric matching structure, in each subdomain, wave matrices and transfer matrices are introduced. A wave matrix is a column matrix that contains the components of the mode in the direction of increasing  $z$ , and the components of the mode in the direction of decreasing  $z$ :

$$[\Psi^{(n)}(z)] = \begin{bmatrix} \Psi^{(n)+}(z) \\ \Psi^{(n)-}(z) \end{bmatrix}; n = 2, 3, 4 \quad (3.4.1)$$

#### 3.4.1 Transfer matrices

The subdomains and their quantities are shown in figure 6.

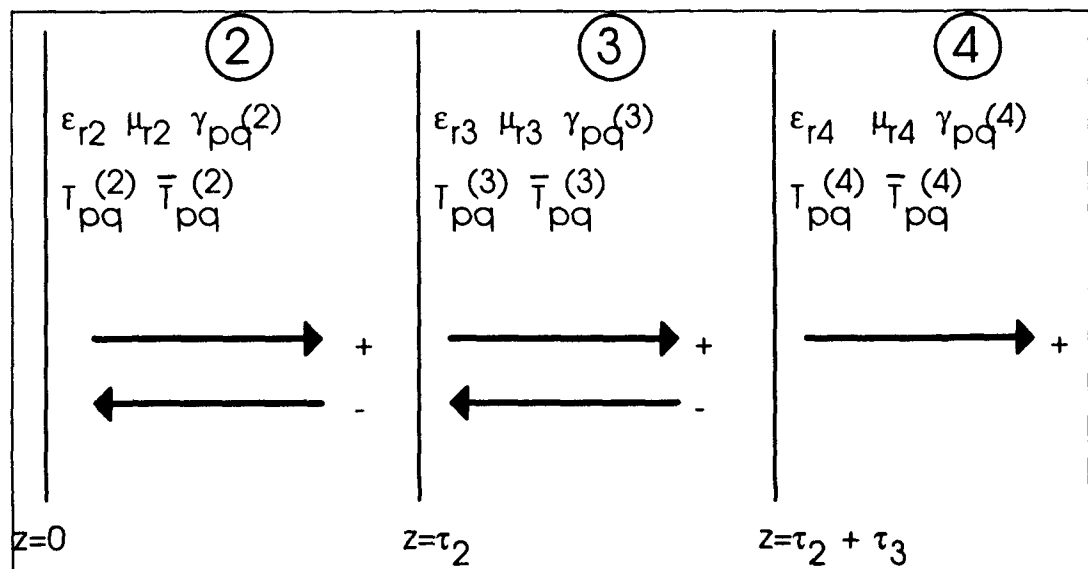


Figure 6: Quantities in the various subdomains ( $n=2,3,4$ ) of  $z>0$

The transfer matrix of the section  $0 < z < \tau_2$  ( $[TR^{(2)}(\tau_2)]$ ) follows from:

$$\lim_{z \downarrow 0} [\Psi^{(2)}(z)] = [TR^{(2)}(\tau_2)] \lim_{z \uparrow \tau_2} [\Psi^{(2)}(z)] \quad (3.4.2)$$

The transfer matrix of the section  $\tau_2 < z < \tau_2 + \tau_3$  ( $[TR^{(3)}(\tau_3)]$ ) follows from:

$$\lim_{z \downarrow \tau_2} [\Psi^{(3)}(z)] = [TR^{(3)}(\tau_3)] \lim_{z \uparrow \tau_2 + \tau_3} [\Psi^{(3)}(z)] \quad (3.4.3)$$

The transfer matrix of the transition from subdomain 2 to subdomain 3 ( $[TR_{2 \rightarrow 3}]$ ) follows from:

$$\lim_{z \uparrow \tau_2} [\Psi^{(2)}(z)] = [TR_{2 \rightarrow 3}] \lim_{z \downarrow \tau_2} [\Psi^{(3)}(z)] \quad (3.4.4)$$

The transfer matrix of the transition from subdomain 3 to subdomain 4 ( $[TR_{3 \rightarrow 4}]$ ) follows from:

$$\lim_{z \uparrow \tau_2 + \tau_3} [\Psi^{(3)}(z)] = [TR_{3 \rightarrow 4}] \lim_{z \downarrow \tau_2 + \tau_3} [\Psi^{(4)}(z)] \quad (3.4.5)$$

The aim of the remainder is to express  $\{T_{pq}^{(2)*}, \overline{T_{pq}^{(2)*}}\}$  in terms of  $\{T_{pq}^{(4)*}, \overline{T_{pq}^{(4)*}}\}$ .

### 3.4.1.1 TE-modes

$[\Psi^{(n)}]$  is taken to be:

$$[\Psi^{(n)}] = \begin{bmatrix} H_{z_{pq}}^{(n)*} \\ H_{z_{pq}}^{(n)*} \end{bmatrix} \quad (3.4.6)$$

With the above, we get:

$$\lim_{z \downarrow 0} \begin{bmatrix} H_{z_{pw}}^{(2)*} \\ H_{z_{pw}}^{(2)*} \end{bmatrix} = [TR^{H}_{2 \rightarrow 4}] \lim_{z \downarrow \tau_2 + \tau_3} \begin{bmatrix} H_{z_{pw}}^{(4)*} \\ H_{z_{pw}}^{(4)*} \end{bmatrix} \quad (3.4.7)$$

with:

$$[TR^{H}_{2 \rightarrow 4}] = [TR^{(2)}(\tau_2)] [TR^{H}_{2 \rightarrow 3}] [TR^{(3)}(\tau_3)] [TR^{H}_{3 \rightarrow 4}] \quad (3.4.8)$$

The transfer matrices  $[TR^{(2)}(\tau_2)]$  and  $[TR^{(3)}(\tau)]$  are given by:

$$[TR^{(n)}(\tau_n)] = \begin{bmatrix} \exp(j\gamma_{pq}^{(n)}\tau_n) & 0 \\ 0 & \exp(-j\gamma_{pq}^{(n)}\tau_n) \end{bmatrix}; n = 2, 3 \quad (3.4.9)$$

The transfer matrices  $[TR^{H}_{2 \rightarrow 3}]$  and  $[TR^{H}_{3 \rightarrow 4}]$  follow from the continuity of the tangential components of the electric and magnetic field strengths across the interfaces  $z = \tau_2$  and  $z = \tau_2 + \tau_3$ :

$$\lim_{z \uparrow \tau_2} \{\bar{E}_T^{(2)}, \bar{H}_T^{(2)}\} = \lim_{z \downarrow \tau_2} \{\bar{E}_T^{(3)}, \bar{H}_T^{(3)}\} \quad (3.4.10a)$$

$$\lim_{z \uparrow \tau_2 + \tau_3} \{\bar{E}_T^{(3)}, \bar{H}_T^{(3)}\} = \lim_{z \downarrow \tau_2 + \tau_3} \{\bar{E}_T^{(4)}, \bar{H}_T^{(4)}\} \quad (3.4.10b)$$

This leads to:

$$[TR^{H}_{2 \rightarrow 3}] = \frac{1}{2Y_{H_{pw}}^{(2)}} \begin{bmatrix} Y_{H_{pw}}^{(2)} + Y_{H_{pw}}^{(3)} & Y_{H_{pw}}^{(2)} - Y_{H_{pw}}^{(3)} \\ Y_{H_{pw}}^{(2)} - Y_{H_{pw}}^{(3)} & Y_{H_{pw}}^{(2)} + Y_{H_{pw}}^{(3)} \end{bmatrix} \quad (3.4.11a)$$

$$[TR^{H}_{3 \rightarrow 4}] = \frac{1}{2Y_{H_{pw}}^{(3)}} \begin{bmatrix} Y_{H_{pw}}^{(3)} + Y_{H_{pw}}^{(4)} & Y_{H_{pw}}^{(3)} - Y_{H_{pw}}^{(4)} \\ Y_{H_{pw}}^{(3)} - Y_{H_{pw}}^{(4)} & Y_{H_{pw}}^{(3)} + Y_{H_{pw}}^{(4)} \end{bmatrix} \quad (3.4.11b)$$

Further:

$$\lim_{z \downarrow 0} \begin{bmatrix} H_{z_{pq}}^{(2)*} \\ H_{z_{pq}}^{(2)*} \end{bmatrix} = \begin{bmatrix} T_{pq}^{(2)*} \exp[-j(u_{p0}x + v_{pq}y)] \\ T_{pq}^{(2)*} \exp[-j(u_{p0}x + v_{pq}y)] \end{bmatrix} \quad (3.4.12a)$$

$$\lim_{z \downarrow \tau_2 + \tau_3} \begin{bmatrix} H_{z_{pq}}^{(4)*} \\ H_{z_{pq}}^{(4)*} \end{bmatrix} = \begin{bmatrix} T_{pq}^{(4)*} \exp[-j(u_{p0}x + v_{pq}y + \gamma_{pq}^{(4)}(\tau_2 + \tau_3))] \\ 0 \end{bmatrix} \quad (3.4.12b)$$

Now, the mode amplitude coefficients  $\{T_{pq}^{(2)*}\}$  can be expressed in terms of mode amplitude coefficients  $\{T_{pq}^{(4)*}\}$ :

$$T_{pq}^{(2)*} = F_{pq} T_{pq}^{(4)*} \quad (3.4.13a)$$

$$T_{pq}^{(2)*} = G_{pq} T_{pq}^{(4)*} \quad (3.4.13b)$$

with:

$$F_{pq} = \left\{ \begin{array}{l} (Y_{H_{pq}}^{(2)} + Y_{H_{pq}}^{(3)})(Y_{H_{pq}}^{(3)} + Y_{H_{pq}}^{(4)}) \exp[j(\gamma_{pq}^{(2)}\tau_2 + \gamma_{pq}^{(3)}\tau_3)] + \\ (Y_{H_{pq}}^{(2)} - Y_{H_{pq}}^{(3)})(Y_{H_{pq}}^{(3)} - Y_{H_{pq}}^{(4)}) \exp[j(\gamma_{pq}^{(2)}\tau_2 - \gamma_{pq}^{(3)}\tau_3)] \end{array} \right\} \exp[-j\gamma_{pq}^{(4)}(\tau_2 + \tau_3)] / 4Y_{H_{pq}}^{(2)}Y_{H_{pq}}^{(3)} \quad (3.4.14a)$$

$$G_{pq} = \left\{ \begin{array}{l} (Y_{H_{pq}}^{(2)} - Y_{H_{pq}}^{(3)})(Y_{H_{pq}}^{(3)} + Y_{H_{pq}}^{(4)}) \exp[-j(\gamma_{pq}^{(2)}\tau_2 - \gamma_{pq}^{(3)}\tau_3)] + \\ (Y_{H_{pq}}^{(2)} + Y_{H_{pq}}^{(3)})(Y_{H_{pq}}^{(3)} - Y_{H_{pq}}^{(4)}) \exp[-j(\gamma_{pq}^{(2)}\tau_2 + \gamma_{pq}^{(3)}\tau_3)] \end{array} \right\} \exp[-j\gamma_{pq}^{(4)}(\tau_2 + \tau_3)] / 4Y_{H_{pq}}^{(2)}Y_{H_{pq}}^{(3)} \quad (3.4.14b)$$

### 3.4.1.2 TM-modes

Analogous to the procedure in the previous paragraph:

$$\overline{T}_{pq}^{(2)*} = \overline{F}_{pq} \overline{T}_{pq}^{(4)*} \quad (3.4.15a)$$

$$\overline{T}_{pq}^{(2)*} = \overline{G}_{pq} \overline{T}_{pq}^{(4)*} \quad (3.4.15b)$$

with:

$$\overline{F}_{pq} = \left\{ \begin{array}{l} (Z_{E_{\nu}}^{(2)} + Z_{E_{\nu}}^{(3)})(Z_{E_{\nu}}^{(3)} + Z_{E_{\nu}}^{(4)}) \exp[j(\gamma_{pq}^{(2)}\tau_2 + \gamma_{pq}^{(3)}\tau_3)] + \\ (Z_{E_{\nu}}^{(2)} - Z_{E_{\nu}}^{(3)})(Z_{E_{\nu}}^{(3)} - Z_{E_{\nu}}^{(4)}) \exp[j(\gamma_{pq}^{(2)}\tau_2 - \gamma_{pq}^{(3)}\tau_3)] \end{array} \right\} \exp[-j\gamma_{pq}^{(4)}(\tau_2 + \tau_3)] / 4Z_{E_{\nu}}^{(2)}Z_{E_{\nu}}^{(3)} \quad (3.4.16a)$$

$$\overline{G}_{pq} = \left\{ \begin{array}{l} (Z_{E_{\nu}}^{(2)} - Z_{E_{\nu}}^{(3)})(Z_{E_{\nu}}^{(3)} + Z_{E_{\nu}}^{(4)}) \exp[-j(\gamma_{pq}^{(2)}\tau_2 - \gamma_{pq}^{(3)}\tau_3)] + \\ (Z_{E_{\nu}}^{(2)} + Z_{E_{\nu}}^{(3)})(Z_{E_{\nu}}^{(3)} - Z_{E_{\nu}}^{(4)}) \exp[-j(\gamma_{pq}^{(2)}\tau_2 + \gamma_{pq}^{(3)}\tau_3)] \end{array} \right\} \exp[-j\gamma_{pq}^{(4)}(\tau_2 + \tau_3)] / 4Z_{E_{\nu}}^{(2)}Z_{E_{\nu}}^{(3)} \quad (3.4.16b)$$

### 3.4.2 Matching

The representations of the tangential electric and magnetic field as  $z \downarrow 0$  will be matched to the ones in the aperture at  $z = 0$ ; the representations of the tangential electric and magnetic field as  $z \uparrow 0$  will be matched to the ones in the aperture at  $z = 0$ . This results in the following equations [12, 15]:

$$\left[ -\omega\mu_0\nu_{pq}(F_{pq} + G_{pq})\overline{T}_{pq}^{(4)*} - \gamma_{pq}^{(2)}u_{p0}(\overline{F}_{pq} - \overline{G}_{pq})\overline{T}_{pq}^{(4)*} \right] F_1 F_2 / k_{T_{pq}}^2 = \sum_{lw} A_{lw} F_7 F_8; w \neq 0 \quad (3.4.17a)$$



$$\left[ \omega \mu_0 \mu_{p0} (F_{pq} + G_{pq}) T_{pq}^{(4)*} - \gamma_{pq}^{(2)} \nu_{pq} (\overline{F}_{pq} - \overline{G}_{pq}) \overline{T}_{pq}^{(4)*} \right] F_1 F_2 / k_{T_{pq}}^2 = \sum_{lw} B_{lw} F_3 F_{10}; l \neq 0 \quad (3.4.17b)$$

$$j \left[ \omega \mu_0 \left( \frac{n\pi}{b} \right) (I_{mn}^{(1)*} + I_{mn}^{(1)}) - \gamma_{mn}^{(1)} \left( \frac{m\pi}{a} \right) (\overline{I}_{mn}^{(1)*} - \overline{I}_{mn}^{(1)}) \right] F_3 F_4 / k_{T_{mn}}^2 = \sum_{lw} A_{lw} F_{11} F_{12}; w, n \neq 0 \quad (3.4.17c)$$

$$j \left[ -\omega \mu_0 \left( \frac{m\pi}{a} \right) (I_{mn}^{(1)*} + I_{mn}^{(1)}) - \gamma_{mn}^{(1)} \left( \frac{n\pi}{b} \right) (\overline{I}_{mn}^{(1)*} - \overline{I}_{mn}^{(1)}) \right] F_5 F_6 / k_{T_{mn}}^2 = \sum_{lw} B_{lw} F_{13} F_{14}; l, m \neq 0 \quad (3.4.17d)$$

$$\sum_{mn} j \left[ \gamma_{mn}^{(1)} \left( \frac{m\pi}{a} \right) (I_{mn}^{(1)*} - I_{mn}^{(1)}) + \omega \epsilon_0 \left( \frac{n\pi}{b} \right) (\overline{I}_{mn}^{(1)*} + \overline{I}_{mn}^{(1)}) \right] F_{13} F_{14} / k_{T_{mn}}^2 = \quad (3.4.17e)$$

$$\sum_{pq} \left[ -\gamma_{pq}^{(2)} \nu_{pq} (F_{pq} - G_{pq}) T_{pq}^{(4)*} + \omega \epsilon_0 \nu_{pq} (\overline{F}_{pq} + \overline{G}_{pq}) \overline{T}_{pq}^{(4)*} \right] F_{15} F_{16} / k_{T_{pq}}^2$$

$$\sum_{mn} j \left[ \gamma_{mn}^{(1)} \left( \frac{n\pi}{b} \right) (I_{mn}^{(1)*} - I_{mn}^{(1)}) - \omega \epsilon_0 \left( \frac{m\pi}{a} \right) (\overline{I}_{mn}^{(1)*} + \overline{I}_{mn}^{(1)}) \right] F_{11} F_{12} / k_{T_{mn}}^2 = \quad (3.4.17f)$$

$$\sum_{pq} \left[ -\gamma_{pq}^{(2)} \nu_{pq} (F_{pq} - G_{pq}) T_{pq}^{(4)*} - \omega \epsilon_0 \mu_{p0} (\overline{F}_{pq} + \overline{G}_{pq}) \right] F_{17} F_{18} / k_{T_{pq}}^2$$

F<sub>1</sub> to F<sub>18</sub> are defined in appendix A.

### 3.4.3 Matrix representation

The matching of the representation of the tangential electric field as  $z \downarrow 0$  to the one in the aperture at  $z = 0$  yields a system of the form:

$$T = C^{(1)} A \quad (3.4.18)$$

T being a column matrix containing the free space transmission coefficients.

The matching of the representation of the tangential electric field as  $z \uparrow 0$  to the one in the aperture at  $z = 0$  yields a system of the form:

$$R = D^{(1)}A + D^{(2)}I \quad (3.4.19)$$

$R$  being a column matrix containing the waveguide reflection coefficients.  $I$  is a column matrix containing the waveguide excitation coefficients.

The matching of the representation of the tangential magnetic field as  $z \downarrow 0$  to the one in the aperture at  $z = 0$  yields a system of the form:

$$U^{(1)}T = U^{(2)}I + U^{(3)}R \quad (3.4.20)$$

In the above,  $A$ ,  $I$ ,  $R$  and  $T$  are column matrices formed by

$\{A_{l_w}, B_{l_w}\}$ ,  $\{I_{mn}^{(1)}, \overline{I_{mn}^{(1)}}\}$ ,  $\{I_{mn}^{(1)}, \overline{I_{mn}^{(1)}}\}$ ,  $\{T_{pq}^{(4)}, \overline{T_{pq}^{(4)}}\}$ , respectively. The other matrices are matrices of known coefficients.

Substitution of (3.4.18) and (3.4.19) in (3.4.20) results in:

$$[W^{(1)} - W^{(2)}]A = B^{(1)} \quad (3.4.21)$$

with:

$$W^{(1)} = U^{(1)}C^{(1)} \quad (3.4.22)$$

$$W^{(2)} = U^{(3)}D^{(2)} \quad (3.4.23)$$

$$B^{(1)} = U^{(4)}I \quad (3.4.24)$$

$$U^{(4)} = U^{(2)} + U^{(3)}D^{(2)} \quad (3.4.25)$$

The matching procedure leads to an infinite system of linear equations with  $\{A_{l_w}, B_{l_w}\}$  as unknowns. This system can be solved numerically by truncating it. Once equation (3.4.21) is solved for  $A$ , the unknown column matrices  $T$  and  $R$  are obtained upon substituting  $A$  in (3.4.18) and (3.4.19), respectively.

### 3.4.3.1 Derivation of C<sup>(1)</sup>

After some mathematical manipulation of equations (3.4.17a,b) [13], we get:

$$T_{pq}^{(4)*} = \sum_{lw} C_{pqlw}^{(1a)} A_{lw} + \sum_{lw} C_{pqlw}^{(1b)} B_{lw} \quad (3.4.26a)$$

$$\overline{T}_{pq}^{(4)*} = \sum_{lw} \overline{C}_{pqlw}^{(1a)} A_{lw} + \sum_{lw} \overline{C}_{pqlw}^{(1b)} B_{lw} \quad (3.4.26b)$$

with:

$$C_{pqlw}^{(1a)} = -\left(k_{T_{pw}}^2 / F_1 F_2 \omega \mu_0\right) \left[ (u_{p0}^2 + v_{pq}^2) (F_{pq} + G_{pq}) \right]^{-1} v_{pq} F_7 F_8; w \neq 0 \quad (3.4.27a)$$

$$C_{pqlw}^{(1b)} = \left(k_{T_{pw}}^2 / F_1 F_2 \omega \mu_0\right) \left[ (u_{p0}^2 + v_{pq}^2) (F_{pq} + G_{pq}) \right]^{-1} u_{p0} F_9 F_{10}; l \neq 0 \quad (3.4.27b)$$

$$\overline{C}_{pqlw}^{(1a)} = -\left(k_{T_{pw}}^2 / F_1 F_2 \gamma_{pq}^{(2)}\right) \left[ (u_{p0}^2 + v_{pq}^2) (\overline{F}_{pq} - \overline{G}_{pq}) \right]^{-1} u_{p0} F_7 F_8; w \neq 0 \quad (3.4.27c)$$

$$\overline{C}_{pqlw}^{(1b)} = -\left(k_{T_{pw}}^2 / F_1 F_2 \gamma_{pq}^{(2)}\right) \left[ (u_{p0}^2 + v_{pq}^2) (\overline{F}_{pq} - \overline{G}_{pq}) \right]^{-1} v_{pq} F_9 F_{10}; l \neq 0 \quad (3.4.27d)$$

Or:

$$T = C^{(1)} A \quad (3.4.28)$$

with:

$$T = \begin{bmatrix} T^{(4)*} & -\rho_{\max, -q \max} \\ \vdots & \vdots \\ T^{(4)*} & \rho_{\max, q \max} \\ \bar{T}^{(4)*} & -\rho_{\max, -q \max} \\ \vdots & \vdots \\ \bar{T}^{(4)*} & \rho_{\max, q \max} \end{bmatrix} \quad (3.4.29a)$$

$$A = \begin{bmatrix} A_{00} \\ \vdots \\ A_{l \max, w \max} \\ B_{00} \\ \vdots \\ B_{l \max, w \max} \end{bmatrix}; \text{ first half: } w \neq 0, \text{ second half: } l \neq 0 \quad (3.4.29b)$$

$$C^{(1)} = \begin{bmatrix} C^{(1a)} & -\rho_{\max, -q \max, 0, 0} & \dots & C^{(1a)} & -\rho_{\max, -q \max, l \max, w \max} & C^{(1b)} & -\rho_{\max, -q \max, 0, 0} & \dots & C^{(1b)} & -\rho_{\max, -q \max, l \max, w \max} \\ \vdots & \vdots & \ddots & \vdots & \vdots & \vdots & \vdots & \ddots & \vdots & \vdots \\ C^{(1a)} & \rho_{\max, q \max, 0, 0} & \dots & C^{(1a)} & \rho_{\max, q \max, l \max, w \max} & C^{(1b)} & \rho_{\max, q \max, 0, 0} & \dots & C^{(1b)} & \rho_{\max, q \max, l \max, w \max} \\ \bar{C}^{(1a)} & -\rho_{\max, -q \max, 0, 0} & \dots & \bar{C}^{(1a)} & -\rho_{\max, -q \max, l \max, w \max} & \bar{C}^{(1b)} & -\rho_{\max, -q \max, 0, 0} & \dots & \bar{C}^{(1b)} & -\rho_{\max, -q \max, l \max, w \max} \\ \vdots & \vdots & \ddots & \vdots & \vdots & \vdots & \vdots & \ddots & \vdots & \vdots \\ \bar{C}^{(1a)} & \rho_{\max, q \max, 0, 0} & \dots & \bar{C}^{(1a)} & \rho_{\max, q \max, l \max, w \max} & \bar{C}^{(1b)} & \rho_{\max, q \max, 0, 0} & \dots & \bar{C}^{(1b)} & \rho_{\max, q \max, l \max, w \max} \end{bmatrix}$$

first quadrant :  $w \neq 0$

second quadrant :  $l \neq 0$

third quadrant :  $w \neq 0$

fourth quadrant :  $l \neq 0$

(3.4.29c)

### 3.4.3.2 Derivation of $D^{(1)}$ and $D^{(2)}$

After some mathematical manipulation of equations (3.4.17c,d) [13], we get:

$$I_{mn}^{(1)*} = \sum_{lw} D^{(1a)}_{mnlw} A_{lw} + \sum_{lw} D^{(1b)}_{mnlw} B_{lw} - I_{mn}^{(1)*} \quad (3.4.30a)$$

$$\overline{I}_{mn}^{(1)*} = \sum_{lw} \overline{D}^{(1a)}_{mnlw} A_{lw} + \sum_{lw} \overline{D}^{(1b)}_{mnlw} B_{lw} + \overline{I}_{mn}^{(1)*} \quad (3.4.30b)$$

with:

$$D^{(1a)}_{mnlw} = -j(k_{T_{mn}}^2 / \omega\mu_0) \left[ \left\{ \left( \frac{m\pi}{a} \right)^2 + \left( \frac{n\pi}{b} \right)^2 \right\} F_3 F_4 \right]^{-1} \left( \frac{n\pi}{b} \right) F_{11} F_{12}; w, n \neq 0 \quad (3.4.31a)$$

$$D^{(1b)}_{mnlw} = j(k_{T_{mn}}^2 / \omega\mu_0) \left[ \left\{ \left( \frac{m\pi}{a} \right)^2 + \left( \frac{n\pi}{b} \right)^2 \right\} F_5 F_6 \right]^{-1} \left( \frac{m\pi}{a} \right) F_{13} F_{14}; l, m \neq 0 \quad (3.4.31b)$$

$$\overline{D}^{(1a)}_{mnlw} = -j(k_{T_{mn}}^2 / \gamma_{mn}^{(1)}) \left[ \left\{ \left( \frac{m\pi}{a} \right)^2 + \left( \frac{n\pi}{b} \right)^2 \right\} F_3 F_4 \right]^{-1} \left( \frac{m\pi}{a} \right) F_{11} F_{12}; w, n \neq 0 \quad (3.4.31c)$$

$$\overline{D}^{(1b)}_{mnlw} = -j(k_{T_{mn}}^2 / \gamma_{mn}^{(1)}) \left[ \left\{ \left( \frac{m\pi}{a} \right)^2 + \left( \frac{n\pi}{b} \right)^2 \right\} F_5 F_6 \right]^{-1} \left( \frac{n\pi}{b} \right) F_{13} F_{14}; l, m \neq 0 \quad (3.4.31d)$$

Or:

$$R = D^{(1)}A + D^{(2)}I \quad (3.4.32)$$

with:

$$R = \begin{bmatrix} I_{00}^{(1)*} \\ \vdots \\ I_{m \max, n \max}^{(1)*} \\ \bar{I}_{00}^{(1)*} \\ \vdots \\ \bar{I}_{m \max, n \max}^{(1)*} \end{bmatrix}; \text{ first half: } (m, n) \neq (0, 0), \text{ second half: } m \neq 0, n \neq 0 \quad (3.4.33a)$$

$$I = \begin{bmatrix} I_{00}^{(1)*} \\ \vdots \\ I_{m \max, n \max}^{(1)*} \\ \bar{I}_{00}^{(1)*} \\ \vdots \\ \bar{I}_{m \max, n \max}^{(1)*} \end{bmatrix}; \text{ first half: } (m, n) \neq (0, 0), \text{ second half: } m \neq 0, n \neq 0 \quad (3.4.33b)$$

$$D^{(1)} = \begin{bmatrix} D_{0,0,0,0}^{(1a)} & \cdots & D_{0,0,l \max, w \max}^{(1a)} & D_{0,0,0,0}^{(1b)} & \cdots & D_{0,0,l \max, w \max}^{(1b)} \\ \vdots & \ddots & \vdots & \vdots & \ddots & \vdots \\ D_{m \max, n \max, 0,0}^{(1a)} & \cdots & D_{m \max, n \max, l \max, w \max}^{(1a)} & D_{m \max, n \max, 0,0}^{(1b)} & \cdots & D_{m \max, n \max, l \max, w \max}^{(1b)} \\ \bar{D}_{0,0,0,0}^{(1a)} & \cdots & \bar{D}_{0,0,l \max, w \max}^{(1a)} & \bar{D}_{0,0,0,0}^{(1b)} & \cdots & \bar{D}_{0,0,l \max, w \max}^{(1b)} \\ \vdots & \ddots & \vdots & \vdots & \ddots & \vdots \\ \bar{D}_{m \max, n \max, 0,0}^{(1a)} & \cdots & \bar{D}_{m \max, n \max, l \max, w \max}^{(1a)} & \bar{D}_{m \max, n \max, 0,0}^{(1b)} & \cdots & \bar{D}_{m \max, n \max, l \max, w \max}^{(1b)} \end{bmatrix}$$

first quadrant :  $w \neq 0, n \neq 0$

second quadrant :  $l \neq 0, m \neq 0$

third quadrant :  $w \neq 0, m \neq 0, n \neq 0$

fourth quadrant :  $l \neq 0, m \neq 0, n \neq 0$

(3.4.33c)

$$D^{(2)} = \begin{bmatrix} -1 & \dots & 0 & 0 & \dots & 0 \\ \vdots & \ddots & \vdots & \vdots & \ddots & \vdots \\ 0 & \dots & -1 & 0 & \dots & 0 \\ 0 & \dots & 0 & 1 & \dots & 0 \\ \vdots & \ddots & \vdots & \vdots & \ddots & \vdots \\ 0 & \dots & 0 & 0 & \dots & 1 \end{bmatrix} \quad (3.4.33d)$$

### 3.4.3.3 Derivation of $U^{(1)}$ , $U^{(2)}$ and $U^{(3)}$

After some mathematical manipulation of equations (3.4.17e,f) [13], we get:

$$\begin{aligned} \sum_{pq} U^{(1a)}{}_{pqlw} T_{pq}{}^{(4)*} + \sum_{pq} \bar{U}^{(1a)}{}_{pqlw} \bar{T}_{pq}{}^{(4)*} &= \sum_{mn} U^{(2a)}{}_{mnlw} I_{mn}{}^{(1)*} + \sum_{mn} \bar{U}^{(2a)}{}_{mnlw} \bar{I}_{mn}{}^{(1)*} + \\ \sum_{mn} U^{(3a)}{}_{mnlw} I_{mn}{}^{(1)*} + \sum_{mn} \bar{U}^{(3a)}{}_{mnlw} \bar{I}_{mn}{}^{(1)*} & \end{aligned} \quad (3.4.34a)$$

$$\begin{aligned} \sum_{pq} U^{(1b)}{}_{pqlw} T_{pq}{}^{(4)*} + \sum_{pq} \bar{U}^{(1b)}{}_{pqlw} \bar{T}_{pq}{}^{(4)*} &= \sum_{mn} U^{(2b)}{}_{mnlw} I_{mn}{}^{(1)*} + \sum_{mn} \bar{U}^{(2b)}{}_{mnlw} \bar{I}_{mn}{}^{(1)*} + \\ \sum_{mn} U^{(3b)}{}_{mnlw} I_{mn}{}^{(1)*} + \sum_{mn} \bar{U}^{(3b)}{}_{mnlw} \bar{I}_{mn}{}^{(1)*} & \end{aligned} \quad (3.4.34b)$$

with:

$$U^{(1a)}{}_{pqlw} = -\gamma_{pq}{}^{(2)} u_{p0} (F_{pq} - G_{pq}) F_{15} F_{16} / k_{T_{pq}}{}^2; l \neq 0 \quad (3.4.35a)$$

$$\bar{U}^{(1a)}{}_{pqlw} = \omega \epsilon_0 v_{pq} (\bar{F}_{pq} + \bar{G}_{pq}) F_{15} F_{16} / k_{T_{pq}}{}^2; l \neq 0 \quad (3.4.35b)$$

$$U^{(2a)}_{mnlw} = j\gamma_{mn}^{(1)} \left( \frac{m\pi}{a} \right) F_{13} F_{14} / k_{T_{mn}}^2; l \neq 0, m \neq 0 \quad (3.4.35c)$$

$$\bar{U}^{(2a)}_{mnlw} = j\omega\epsilon_0 \left( \frac{n\pi}{b} \right) F_{13} F_{14} / k_{T_{mn}}^2; l \neq 0, m \neq 0 \quad (3.4.35d)$$

$$U^{(3a)}_{mnlw} = -U^{(2a)}_{mnlw}; l \neq 0, m \neq 0 \quad (3.4.35e)$$

$$\bar{U}^{(3a)}_{mnlw} = \bar{U}^{(2a)}_{mnlw}; l \neq 0, m \neq 0 \quad (3.4.35f)$$

$$U^{(1b)}_{pqlw} = -\gamma_{pq}^{(2)} \nu_{pq} (F_{17} - G_{17}) F_{17} F_{18} / k_{T_{pq}}^2; w \neq 0 \quad (3.4.35g)$$

$$\bar{U}^{(1b)}_{pqlw} = \omega\epsilon_0 \mu_{p0} (\bar{F}_{17} + \bar{G}_{17}) F_{17} F_{18} / k_{T_{pq}}^2; w \neq 0 \quad (3.4.35h)$$

$$U^{(2b)}_{mnlw} = j\gamma_{mn}^{(1)} \left( \frac{n\pi}{b} \right) F_{11} F_{12} / k_{T_{mn}}^2; w \neq 0, n \neq 0 \quad (3.4.35i)$$

$$\bar{U}^{(2b)}_{mnlw} = -j\omega\epsilon_0 \left( \frac{m\pi}{a} \right) F_{11} F_{12} / k_{T_{mn}}^2; w \neq 0, n \neq 0 \quad (3.4.35j)$$

$$U^{(3b)}_{mnlw} = -U^{(2b)}_{mnlw}; w \neq 0, n \neq 0 \quad (3.4.35k)$$

$$\bar{U}^{(3b)}_{mnlw} = \bar{U}^{(2b)}_{mnlw}; w \neq 0, n \neq 0 \quad (3.4.35l)$$

Or:

$$U^{(1)}T = U^{(2)}I + U^{(3)}R \quad (3.4.36)$$



with:

$$U^{(1)} = \begin{bmatrix} U^{(1a)}_{-p \max, -q \max, 0, 0} & \cdots & U^{(1a)}_{p \max, q \max, 0, 0} & U^{(1b)}_{-p \max, -q \max, 0, 0} & \cdots & U^{(1b)}_{p \max, q \max, 0, 0} \\ \vdots & \ddots & \vdots & \vdots & \ddots & \vdots \\ U^{(1a)}_{-p \max, -q \max, l \max, w \max} & \cdots & U^{(1a)}_{p \max, q \max, l \max, w \max} & U^{(1b)}_{-p \max, -q \max, l \max, w \max} & \cdots & U^{(1b)}_{p \max, q \max, l \max, w \max} \\ \bar{U}^{(1a)}_{-p \max, -q \max, 0, 0} & \cdots & \bar{U}^{(1a)}_{p \max, q \max, 0, 0} & \bar{U}^{(1b)}_{-p \max, -q \max, 0, 0} & \cdots & \bar{U}^{(1b)}_{p \max, q \max, 0, 0} \\ \vdots & \ddots & \vdots & \vdots & \ddots & \vdots \\ \bar{U}^{(1a)}_{-p \max, -q \max, l \max, w \max} & \cdots & \bar{U}^{(1a)}_{p \max, q \max, l \max, w \max} & \bar{U}^{(1b)}_{-p \max, -q \max, l \max, w \max} & \cdots & \bar{U}^{(1b)}_{p \max, q \max, l \max, w \max} \end{bmatrix}$$

first quadrant :  $l \neq 0$ second quadrant :  $l \neq 0$ third quadrant :  $w \neq 0$ fourth quadrant :  $w \neq 0$ 

(3.4.37a)

$$U^{(2)} = \begin{bmatrix} U^{(2a)}_{0, 0, 0, 0} & \cdots & U^{(2a)}_{m \max, n \max, 0, 0} & \bar{U}^{(2a)}_{0, 0, 0, 0} & \cdots & \bar{U}^{(2a)}_{m \max, n \max, 0, 0} \\ \vdots & \ddots & \vdots & \vdots & \ddots & \vdots \\ U^{(2a)}_{0, 0, l \max, w \max} & \cdots & U^{(2a)}_{m \max, n \max, l \max, w \max} & \bar{U}^{(2a)}_{0, 0, l \max, w \max} & \cdots & \bar{U}^{(2a)}_{m \max, n \max, l \max, w \max} \\ U^{(2b)}_{0, 0, 0, 0} & \cdots & U^{(2b)}_{m \max, n \max, 0, 0} & \bar{U}^{(2b)}_{0, 0, 0, 0} & \cdots & \bar{U}^{(2b)}_{m \max, n \max, 0, 0} \\ \vdots & \ddots & \vdots & \vdots & \ddots & \vdots \\ U^{(2b)}_{0, 0, l \max, w \max} & \cdots & U^{(2b)}_{m \max, n \max, l \max, w \max} & \bar{U}^{(2b)}_{0, 0, l \max, w \max} & \cdots & \bar{U}^{(2b)}_{m \max, n \max, l \max, w \max} \end{bmatrix}$$

first quadrant :  $l \neq 0, m \neq 0$ second quadrant :  $l \neq 0, m \neq 0, n \neq 0$ third quadrant :  $w \neq 0, n \neq 0$ fourth quadrant :  $w \neq 0, m \neq 0, n \neq 0$ 

(3.4.37b)

$$U^{(2)} = \begin{bmatrix} -U_{0,0,0,0}^{(2a)} & \cdots & -U_{m \max, n \max, 0,0}^{(2a)} & \bar{U}_{0,0,0,0}^{(2a)} & \cdots & \bar{U}_{m \max, n \max, 0,0}^{(2a)} \\ \vdots & \ddots & \vdots & \vdots & \ddots & \vdots \\ -U_{0,0,l \max, w \max}^{(2a)} & \cdots & -U_{m \max, n \max, l \max, w \max}^{(2a)} & \bar{U}_{0,0,l \max, w \max}^{(2a)} & \cdots & \bar{U}_{m \max, n \max, l \max, w \max}^{(2a)} \\ -U_{0,0,0,0}^{(2b)} & \cdots & -U_{m \max, n \max, 0,0}^{(2b)} & \bar{U}_{0,0,0,0}^{(2b)} & \cdots & \bar{U}_{m \max, n \max, 0,0}^{(2b)} \\ \vdots & \ddots & \vdots & \vdots & \ddots & \vdots \\ -U_{0,0,l \max, w \max}^{(2b)} & \cdots & -U_{m \max, n \max, l \max, w \max}^{(2b)} & \bar{U}_{0,0,l \max, w \max}^{(2b)} & \cdots & \bar{U}_{m \max, n \max, l \max, w \max}^{(2b)} \end{bmatrix}$$

first quadrant :  $l \neq 0, m \neq 0$

second quadrant :  $l \neq 0, m \neq 0, n \neq 0$

third quadrant :  $w \neq 0, n \neq 0$

fourth quadrant :  $w \neq 0, m \neq 0, n \neq 0$

(3.4.37c)

Now, with equation (3.4.28) the free space transmission coefficients can be calculated and with equation (3.4.32) the waveguide reflection coefficients can be calculated. The waveguide excitation coefficients are fed into column matrix I.

### 3.5 Finiteness effects

Very large phased array antennas, i.e. antennas consisting of thousands of elements, can be analysed perfectly well by an infinite array theory. For medium sized phased array antennas (a couple of hundreds of elements), an infinite array approach will do, but for more detailed information, finiteness effects have to be included in the array behaviour calculations.

It is because of the above reason and because of our subarray design strategy - to be discussed in chapter 7 - that we have developed an approximate method for calculating the behaviour of an element in a medium sized phased array antenna.

Since direct calculation of finite array behaviour is very complicated and very time consuming for arrays consisting of more than say 10 elements, it is expedient to look for an approximate method.

#### 3.5.1 Approximate method

Use is made of the fact that reflection and coupling coefficients are related by Fourier transforms [16]. Reflection coefficients as function of scanangles  $\vartheta_0$  and  $\varphi_0$  are calculated for an element in an infinite array environment.

By integrating these reflection coefficients over the incremental phase shifts between adjacent elements in x and y directions, coupling coefficients between the elements are approximated.

$$S(m,n) = \frac{1}{4\pi^2} \int_{-\pi}^{\pi} \int_{-\pi}^{\pi} \Gamma(\vartheta_0, \varphi_0) e^{jm\psi_x d_x} e^{jn\psi_y d_y} d(\psi_x d_x) d(\psi_y d_y) \quad (3.5.1a)$$

with:

$$\psi_x = k_0 \cdot \sin(\vartheta_0) \cos(\varphi_0) \quad (3.5.1b)$$

$$\psi_y = k_0 \cdot \sin(\vartheta_0) \sin(\varphi_0) \quad (3.5.1c)$$

$$k_0 = \frac{2\pi}{\lambda} \quad (3.5.1d)$$

The indices  $m$  and  $n$  denote the position of the element within the array.  $(m,n) = (0,0)$  is the centre element.

Note - with reference to figure 4 - that for a rectangular grid array, the parameters  $(s,t)$  and  $(d_x, d_y)$  may be interchanged.

With a finite set of so derived coupling coefficients (the number of coefficients equal to the number of elements in the finite array), reflection coefficients are recalculated, yielding the approximate reflection coefficient behaviour of an element in a finite array environment:

$$\Gamma(\vartheta_0, \varphi_0) = \sum_{-M}^M \sum_{-N}^N S(m,n) e^{-jm\psi_x d_x} e^{-jn\psi_y d_y} \quad (3.5.2)$$

with  $M$  and  $N$  defining the (finite) size of the array.

It appears that the error made in this approximation is much less than the error in applying an infinite array approach as will be shown in chapter 4.

### 3.5.2 Finite array properties

In order to discuss the properties of finite arrays we start with a fictive infinite array. The dimensions, with reference to figure 4, are given below. (these dimensions are taken from the design to be presented in paragraph 6.2).

- $s = t = 36.26$  mm
- $a = b = 32.94$  mm

- $c = d = 22.14$  mm
- $\tau_2 = 0$
- $\tau_3 = 0.77$  mm
- $\epsilon_r = 6.36$

Coupling coefficients relative to the centre element ( $m=0, n=0$ ) are calculated for finite arrays with  $-M < m < M$ ,  $-N < n < N$  and  $M=N$ . For  $M=31$ , the amplitude of the coupling coefficients on the main axes of the array are shown in figure 7.

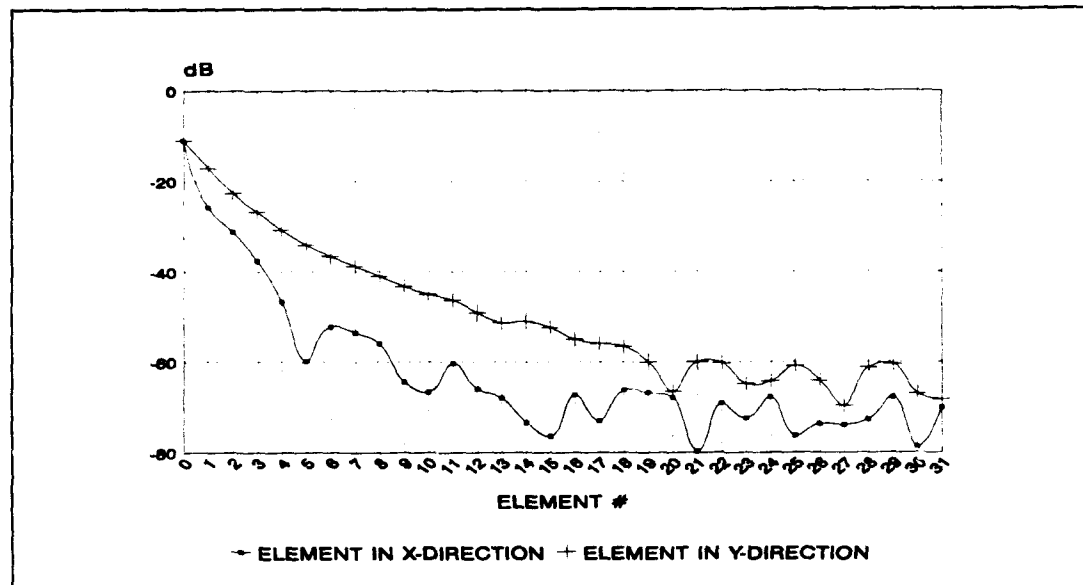


Figure 7: Amplitude coupling coefficients relative to centre element,  $f=5.3$ GHz;  $TE_{10}$ -mode polarisation

We see a sharp decrease in mutual coupling when moving away from the centre element as expected. Moving away more than 31 elements from the centre element does not seem to be meaningful, since the coupling coefficients can not be calculated anymore with enough accuracy.

For  $M=31$ , reflection coefficients in E-, D- and H-plane are recalculated with the obtained coupling coefficients. The results, together with the infinite array reflection coefficients, are shown in figures 8, 9 and 10.

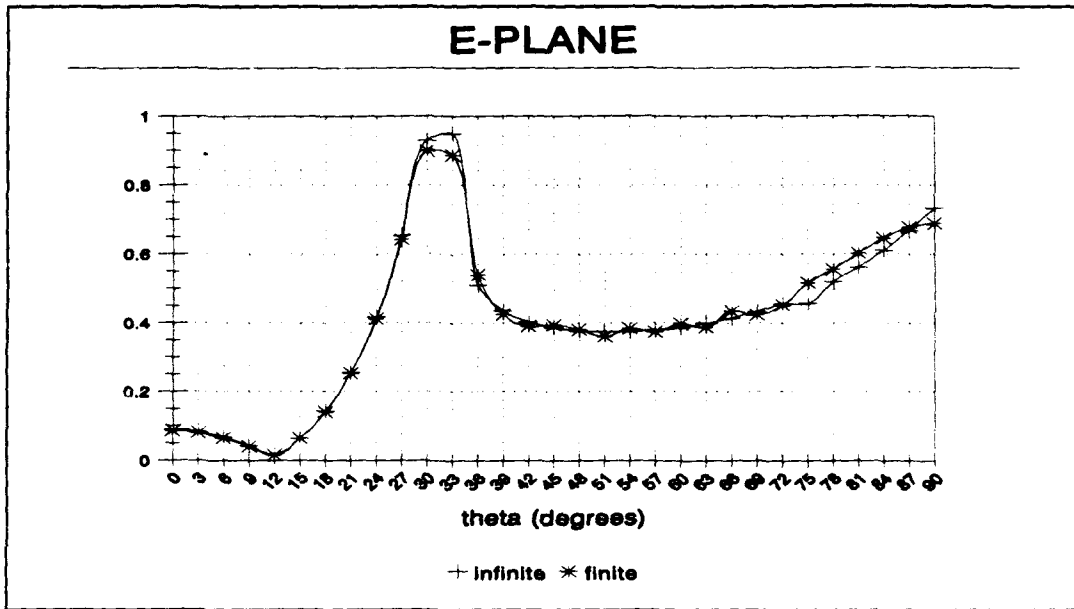


Figure 8: Amplitude infinite and approximate E-plane finite array reflection,  $f=5.3\text{GHz}$ ,  $TE_{10}$ -mode polarisation

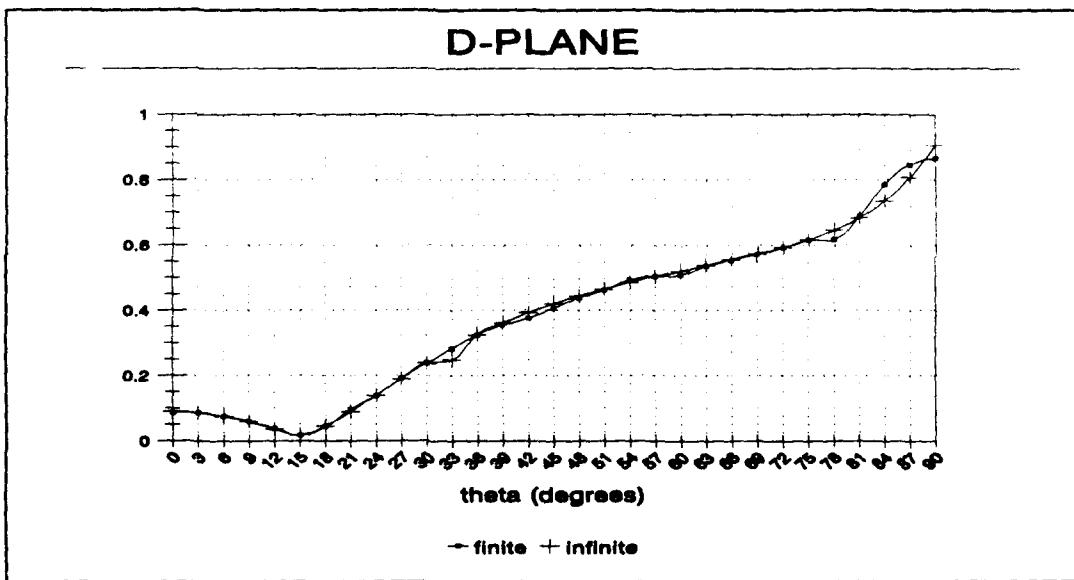


Figure 9: Amplitude infinite and approximate D-plane finite array reflection,  $f=5.3\text{GHz}$ ,  $TE_{10}$ -mode polarisation

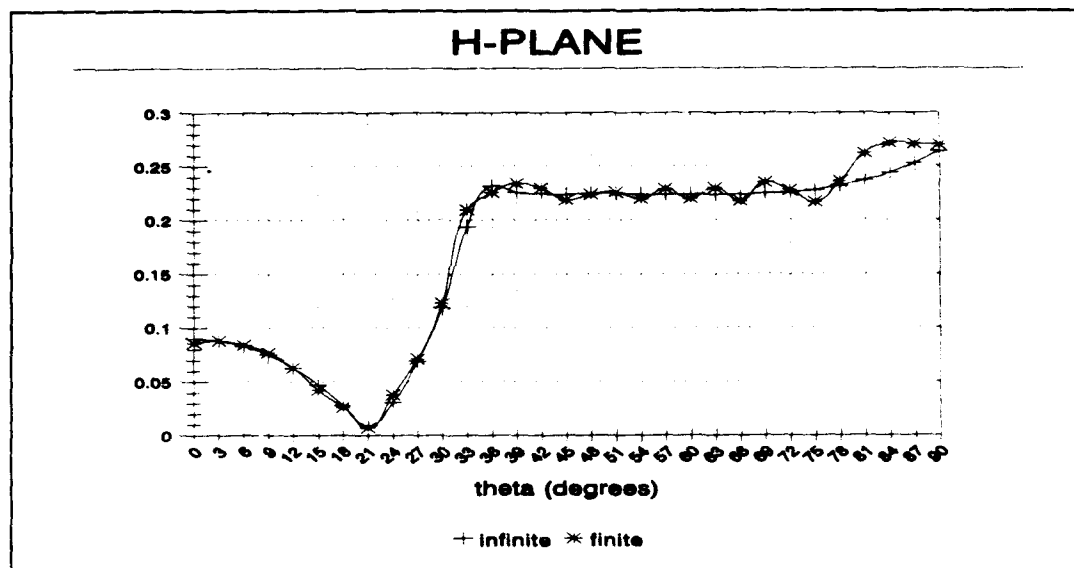


Figure 10: Amplitude infinite and approximate H-plane finite array reflection,  $f=5.3\text{GHz}$ ,  $TE_{10}$ -mode polarisation

The above figures show a near perfect match between infinite array reflection coefficients and approximate finite array reflection coefficients for  $M=31$ . This indicates that for this particular array a  $63 \times 63$  element array can be regarded as being infinite.

In the far scan region we see a fluctuation on the finite array reflection coefficient. This phenomenon is due to the finiteness of the array and is well described in [16, 17]. This phenomenon is also observed in measurements on a finite array [14]. When more elements are added to a finite array, the frequency of the fluctuation increases and the amplitude decreases. To show this, in figure 11 finite array reflection coefficients for different values of  $M$  are compared with the infinite array reflection coefficients in the H-plane.

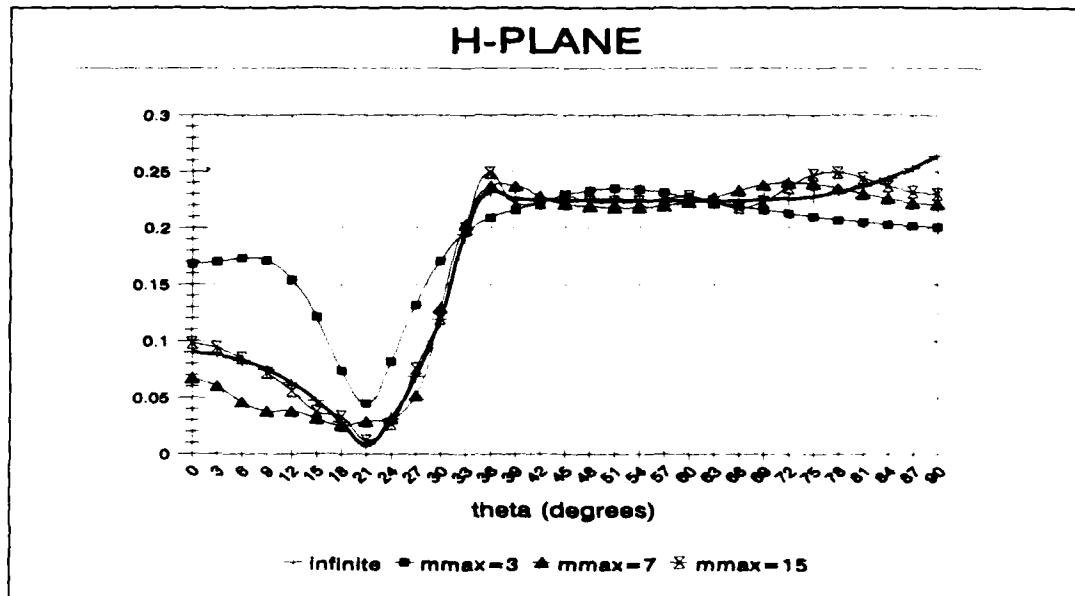


Figure 11: Amplitude reflection coefficient finiteness effects,  $f=5.3\text{GHz}$ ,  $TE_{10}$ -mode polarisation ( $m_{\text{max}}=M$ )

## 4 SOFTWARE VALIDATION

Our waveguide phased array antenna analysis software (program PHASAR) has been tested by calculating the unit cell reflection coefficients for two realised waveguide phased array antennas. The first antenna is CAISSA: a planar, space-fed, phased array antenna of about 850 radiating elements and operating in the C-band. The second antenna is an EXPAR (EXperimental Phased ARray) test antenna, a 255 element array antenna operating in the X-band.

For both antennas the dimensions are such that within the scan range 0-90 degrees, only a single propagating mode is radiated in free space.

### 4.1 CAISSA antenna

The CAISSA antenna is shown in figure 12 [12]. The dimensions, with reference to figure 4, are stated in table 1.

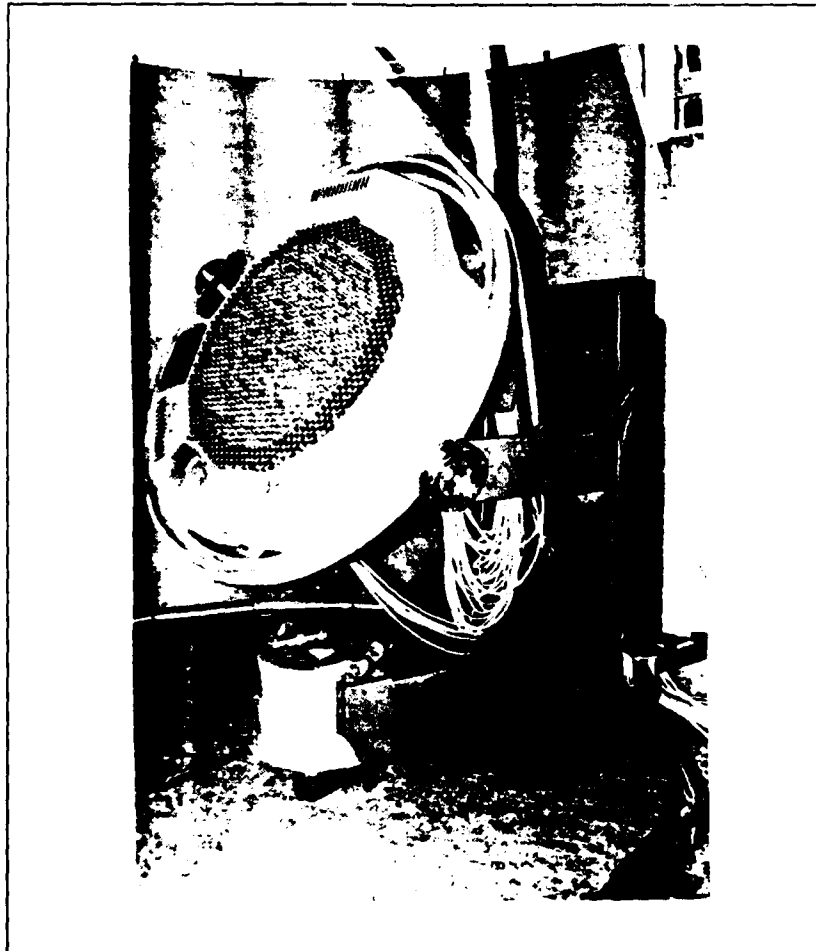


Figure 12: CAISSA antenna without dielectric matching sheet



Table 1: Dimensions CAISSA antenna

a	0.035m	s	0.05m
b	0.0115m	t	0.0289m
c	0.028m	$\tau_2$	0.005m
d	0.0115m	$\tau_3$	0.005m
$\Omega$	30.1°	$\epsilon_r$	2.3

The reflection coefficients calculated with PHASAR are compared with the results obtained from the no longer available program TSCHEBY [12] and results obtained from a computer program written by K.K. Chan (Chan Technologies Inc., Quebec Canada) based on a generalised scattering matrix method in combination with mode matching.

The calculated reflection coefficient amplitudes obtained with the three different programmes are shown in table 2a. The related phases are shown in table 2b.

Table 2a: Amplitudes reflection coefficient  $TE_{10}$ -mode CAISSA at 5.65GHz

$\varphi$ (degrees)	$\theta$ (degrees)	$ \Gamma $ -PHASAR	$ \Gamma $ -TSCHEBY	$ \Gamma $ -CHAN
0	0	<b>0.24</b>	0.24	0.29
0	20	<b>0.21</b>	0.21	0.25
0	40	<b>0.17</b>	0.17	0.19
0	60	<b>0.21</b>	0.21	0.18
45	20	<b>0.19</b>	0.19	0.24
45	40	<b>0.04</b>	0.04	0.09
45	60	<b>0.21</b>	0.21	0.16
90	20	<b>0.19</b>	0.19	0.23
90	40	<b>0.10</b>	0.10	0.11
90	60	<b>0.08</b>	0.08	0.06

Table 2b: Phases reflection coefficient  $TE_{10}$ -mode CAISSA at 5.65GHz (degr.)

$\varphi$ (degrees)	$\theta$ (degrees)	$\angle \Gamma$ -PHASAR	$\angle \Gamma$ -TSCHEBY	$\angle \Gamma$ -CHAN
0	0	<b>105.74</b>	105.50	103.2
0	20	<b>90.56</b>	90.25	92.4
0	40	<b>40.20</b>	39.90	55.5
0	60	<b>329.48</b>	329.60	327.0
45	20	<b>102.63</b>	102.21	100.1
45	40	<b>58.64</b>	56.79	73.7
45	60	<b>279.75</b>	279.87	289.0
90	20	<b>115.78</b>	115.31	108.6
90	40	<b>159.27</b>	158.96	127.1
90	60	<b>194.18</b>	194.71	134.9

From the above it can be concluded that, in comparison with similar purpose programs, the waveguide phased array antenna analysis program PHASAR is working well. The ultimate validation will of course be found in comparison with measurements. This will be discussed in the next paragraph.

## 4.2 EXPAR test antenna

The EXPAR test antenna is shown in figure 13 [14]. The dimensions are classified.

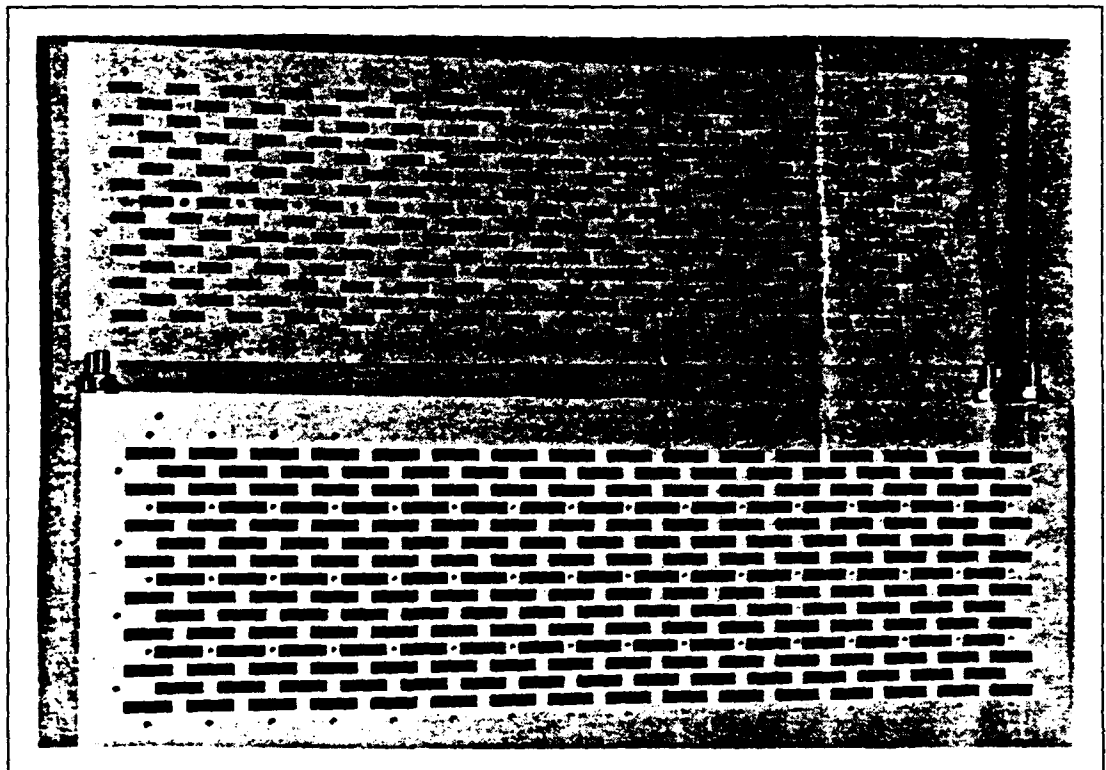


Figure 13: EXPAR test antenna with iris sheet and dielectric matching sheet on top

### 4.2.1 Infinite array calculations

For a certain frequency  $f_0$ , the EXPAR unit cell reflection coefficients as function of scan angle  $\theta$  are measured for H-, D- and E-plane. These measurements, together with the calculated reflection coefficients are shown in figure 14. Coupling coefficients are measured with a vector network analyser and these are fed into equation (3.5.2) to get the 'measured' reflection coefficients.

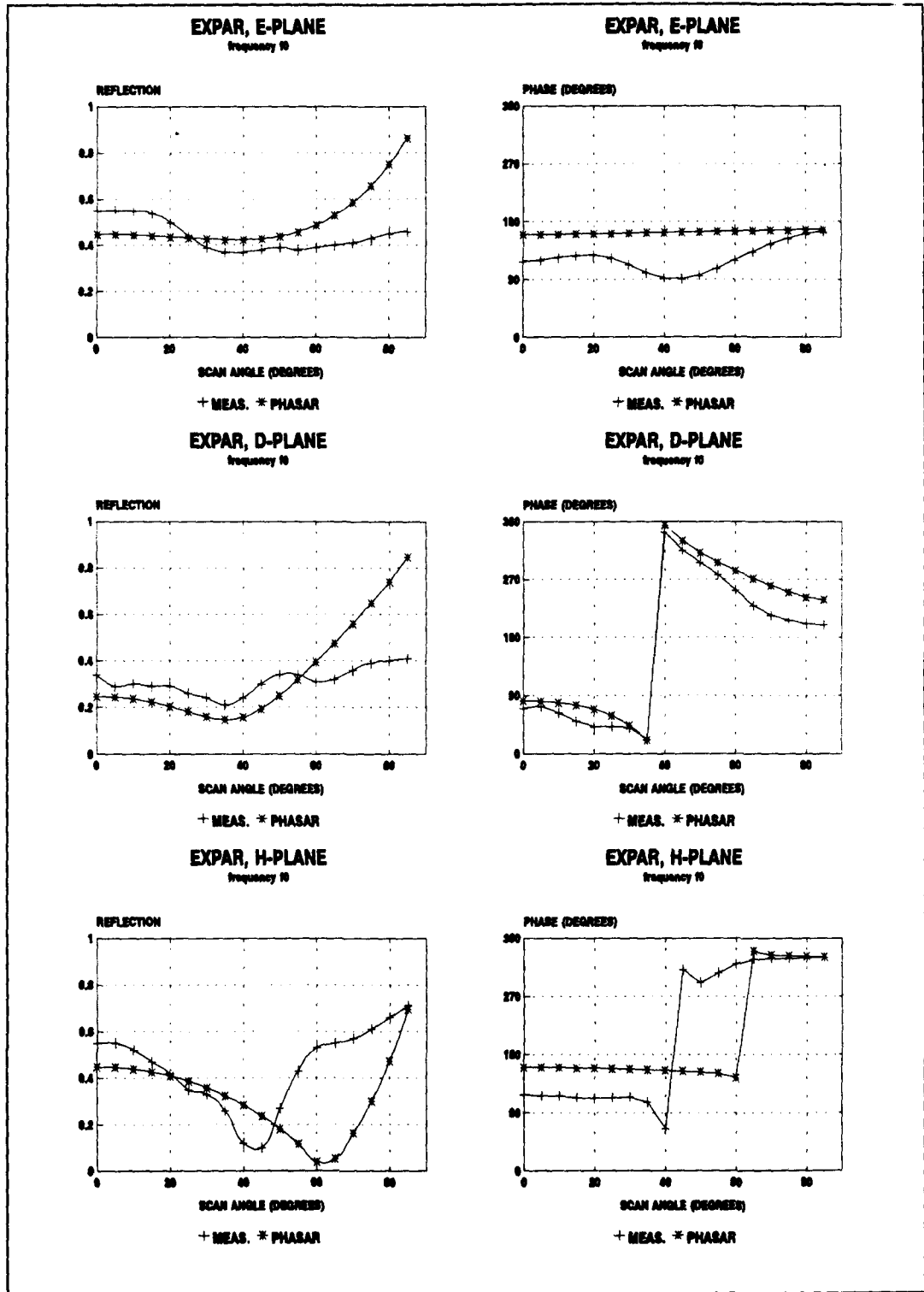


Figure 14: Amplitude and phase of EXPAR unit cell reflection coefficient

The above figure is self-evident: for a basic antenna design the infinite waveguide phased array analysis program PHASAR will do.

Next to investigate are finiteness effects for EXPAR.

#### 4.2.2 Finite array calculations

Since we are dealing with a *wide-angle* waveguide phased array antenna with phaseshifters applied on element to element basis, finiteness effects can be analysed by integrating infinite array reflection coefficients over visible space only, as discussed in paragraph 3.5.1.

Equation (3.5.1) is now expressed as an integration over  $\vartheta_0$  and  $\varphi_0$ . A phase correction factor is added to deal with the triangular lattice. Furthermore, the integration is simplified by making use of symmetry properties in the integration over  $\varphi_0$ . Equation (3.5.1) is replaced by [18]:

$$S(m,n) = 4 \cdot k_0^2 \cdot \frac{d_x d_y}{4\pi^2} \int_0^{\frac{\pi}{2}} \int_0^{\frac{\pi}{2}} \Gamma(\vartheta_0, \varphi_0) \cos \left[ \Psi_x d_x \left( m + \frac{p}{2} \right) \right] \cos \left[ \Psi_y d_y n \right] \cos \vartheta_0 \sin \vartheta_0 d\vartheta_0 d\varphi_0 \quad (4.2.1a)$$

with:

$$p = \begin{cases} 1 & n \text{ odd} \\ 0 & n \text{ even} \end{cases} \quad (4.2.1b)$$

Equation (3.5.2) remains unchanged.

Figure 15 shows H-, D- and E-plane results for a frequency  $f_1$

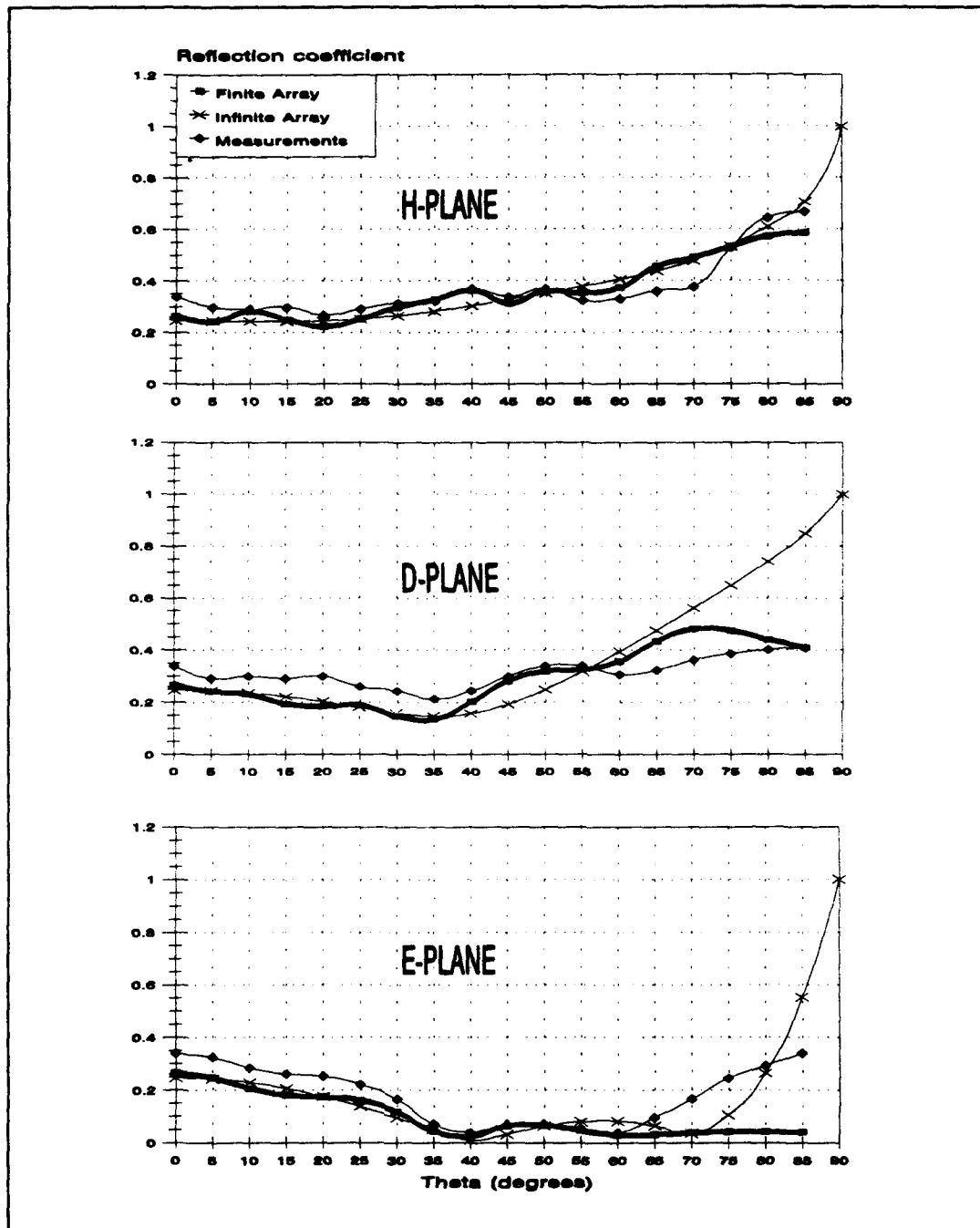


Figure 15: Amplitude EXPAR infinite and approximate finite array reflection coefficient

The above figure clearly shows that by approximating a finite array we get very close to reality.

It is thoroughly demonstrated now that we have the tools necessary to design, in a reliable way, a SAR waveguide phased array antenna.

## 5 ANTENNA SYNTHESIS TOOLS

At TNO-FEL a computer code is developed for analysing infinite arrays of open ended waveguides [12, 15]. The antenna geometry is shown in figure 16. The array lattice can be triangular or rectangular. The waveguides can be rectangular (single polarisation) or square (dual polarisation). For impedance matching purposes, thin irises can be placed in the waveguide apertures and a dielectric sheet can be placed in front of and parallel to the waveguide apertures.

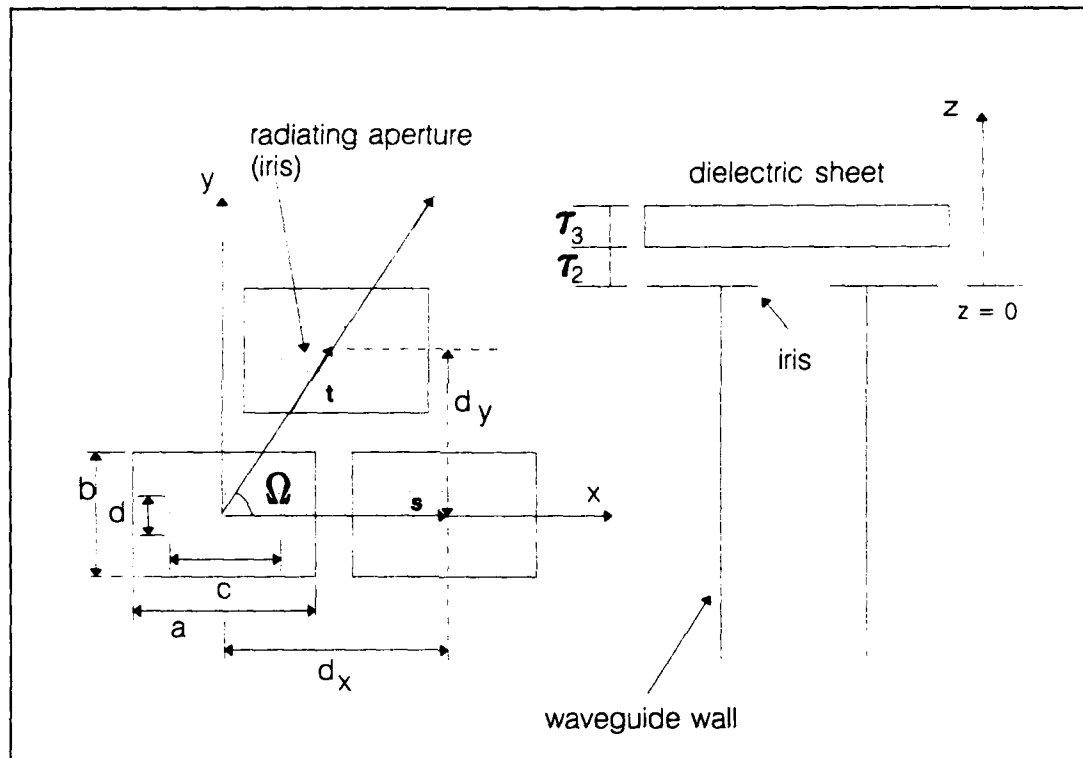


Figure 16: Open-ended waveguide phased array antenna geometry

Design parameters are:

- $a$  : waveguide width
- $b$  : waveguide length
- $c$  : iris width
- $d$  : iris length
- $d_x$  : element spacing in x-direction
- $d_y$  : element spacing in y-direction
- $\Omega$  : triangular lattice angle ( $90^\circ$  for rectangular lattice)
- $\tau_2$  : width air gap
- $\tau_3$  : width dielectric sheet
- $\epsilon_r$  : dielectric constant sheet

Given a set of antenna design specifications, an antenna can be designed by varying the design parameters and using the mentioned analysis code. Due to the number of design parameters and the existence of many local optima in the solution space, this is a very time consuming task and the finding of an optimum antenna design can not be guaranteed.

An optimisation program -using the analysis code- has been developed, that allows for automatically generating an antenna design given a set of design specifications as input.

The optimisation method used is an intermixed combination of simulated annealing and the downhill simplex method due to Nelder and Mead [19]. In this chapter, first the basics of simulated annealing and the downhill simplex method will be explained, after which the intermixed combination of both methods for continuous optimisation will be discussed.

## 5.1 Simulated annealing

Simulated annealing methods are known to have solved some problems previously thought to be practically insoluble (for example the *traveling salesman problem* [20]) and have a direct bearing on the problem of finding global extrema in the presence of large numbers of (undesired) local extrema [21-24]. The latter makes this method very attractive for our synthesis problem.

At the heart of the method of simulated annealing is an analogy with thermodynamics [20], specifically with the way that liquids freeze and crystallise, or metals cool and anneal. At high temperatures, the molecules of a liquid move freely with respect to one another. If the liquid is cooled slowly, thermal mobility is lost. The atoms are often able to line themselves up and form a pure crystal that is completely ordered over a distance up to billions of times the size of the individual atom in all directions. This crystal is the state of minimum energy for this system. If, however, a liquid metal is cooled quickly, it does not reach this state but rather ends up in a polycrystalline or amorphous state having somewhat higher energy.

The so-called Boltzmann probability distribution:

$$\text{Prob}(E) \approx \exp(-E / kT) \quad (5.1.1)$$

expresses the idea that a system in thermal equilibrium at temperature T has its energy probabilistically distributed among all different energy states E. Even at low temperature, there is a chance of a system being in a high energy state. *Therefore, there is a corresponding chance for the system to get out of a local energy minimum in favor of finding a better, more global, one.* The quantity k is Boltzmann's constant that relates temperature to energy.

In other words, the system sometimes goes *uphill* as well as downhill; but the lower the temperature, the less likely is any significant uphill excursion.

In order to use the method described above for optimisation purposes, one needs:

- A description of possible system configurations
- A random generator to probe the solution field
- A function E to be minimised (optimised)
- A control parameter T and an annealing schedule to lower it

In case of the optimisation of our waveguide antenna, the possible system configurations are given in a set of design parameter ranges. The function to be minimised is the unit cell reflection coefficient. The control parameter  $T$  is also the unit cell reflection coefficient. Starting value of  $T$  and annealing schedule are problem dependent and require some experimentation [20]. This is the major drawback of this method. But, if for a specific problem the annealing schedule is figured out, an optimum is found that is better than found by any other method.

A downhill move is always accepted; the chance of accepting an uphill move is prescribed by the Boltzmann probability distribution if no additional information of the minimisation function is known. The optimisation can be speeded up by taking a modified probability distribution [21]. This technique is known as Fast Simulated Annealing.

## 5.2 Downhill simplex method

The downhill simplex method is due to Nelder and Mead [19]. A big advantage is that this method requires only function evaluations, not derivatives. It is an advantage because we can calculate the unit cell reflection coefficient [12, 15], but we do not have an implicit function description describing the transformation from input parameters to reflection coefficient.

A simplex is the geometrical figure consisting, in  $N$  dimensions, of  $N+1$  points (or vertices) and all their interconnecting line segments, polygonal faces, etc.[20]. In two dimensions, a simplex is a triangle. In three dimensions it is a tetrahedron. Only nondegenerate simplexes - i.e. enclosing a finite inner  $N$ -dimensional vector space - are taken into account.

The downhill simplex method must be started with  $N+1$  points, defining an initial simplex. The downhill simplex method now takes a series of steps, most steps just moving the point of the simplex where the function is largest through the opposite face of the simplex to a lower point. These steps are called reflections, and they are constructed to conserve the volume of the simplex (hence maintain its nondegeneracy). When it can do so, the method expands the simplex in one or another direction to take larger steps. When it reaches a "valley floor", the method contracts itself in the transverse direction and tries to ooze down the valey. Note that this method, in contradiction to simulated annealing, does not pretend to find a global minimum; it gets stuck in a local minimum.

Basic moves for a general 3-dimensional minimisation problem are shown in figure 17 [20]



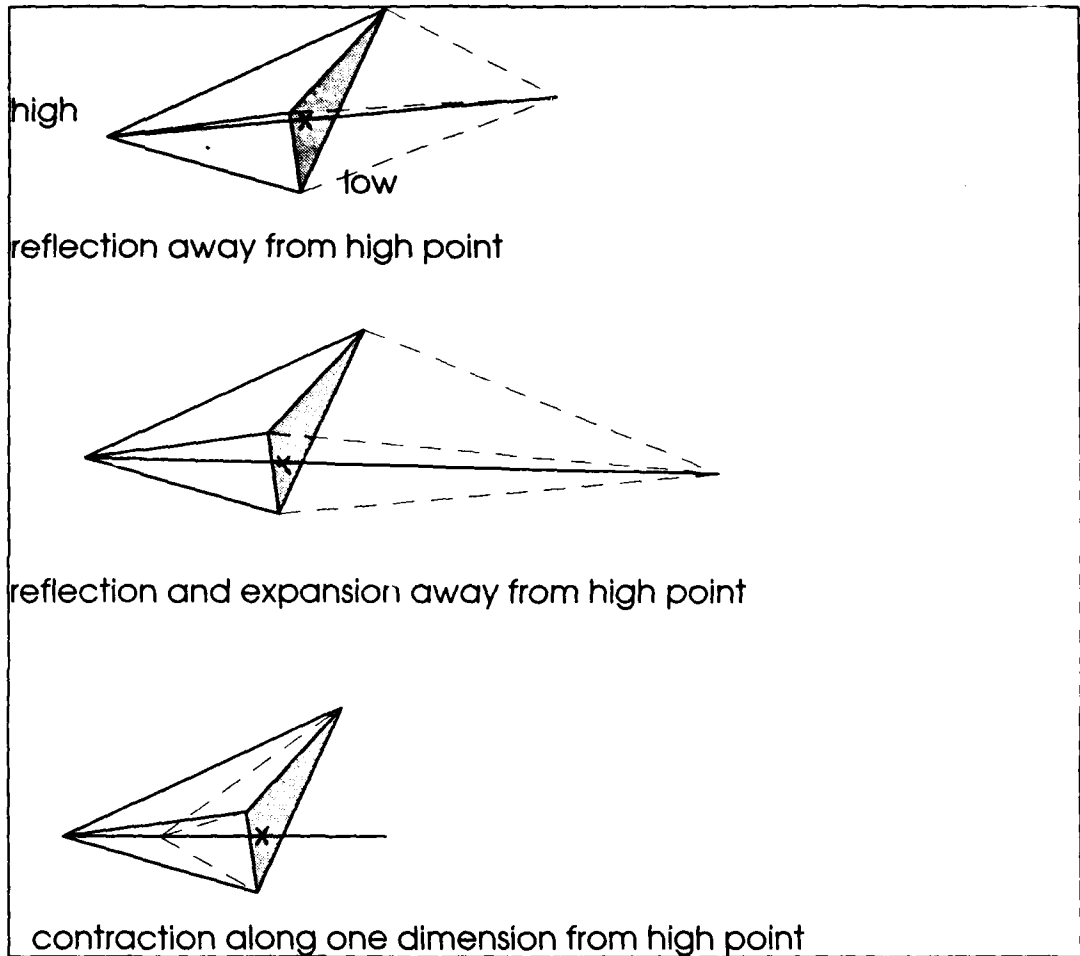


Figure 17: Possible outcomes for a step in the downhill simplex method

### 5.3 Continuous optimisation by simulated annealing

The simulated annealing method described in paragraph 5.1 is initially meant for optimising multidimensional discrete functions. It can be used for continuous optimisation but tends to become inefficient as mentioned in [20] and as experienced by the author. The inefficiency is due to two phenomena [20]: Inefficiency of the random changes generator when proposing an uphill move even when local downhill moves exist and, most of all, inefficiency in convergence when an optimum is approached.

Therefore, a method proposed in [20] is used that is an intermixed combination of simulated annealing and downhill simplex. The optimisation starts as a simulated annealing method and gradually changes to a downhill simplex method as the temperature is lowered. Thus at least an efficient endgame is guaranteed; when the global optimum area is found by simulated annealing, the downhill simplex method rapidly isolates the optimum.

The system state is described by a simplex of  $N+1$  points,  $N$  being the dimension of the optimisation problem. Optimisation moves are as described in paragraph 5.2: reflections, expansions and contractions of the simplex. The simulated annealing is implemented in the following way: added is a positive, logarithmically distributed random variable, proportional to the temperature, to the stored function value associated with every vertex of the simplex, and a similar random variable is subtracted from the function value of every new point that is tried as a replacement point. The method always accepts a true downhill step, but sometimes accepts an uphill one. In the limit  $T \rightarrow 0$ , this algorithm reduces exactly to the downhill simplex method and converges to a local minimum.



## 6 BASIC ANTENNA DESIGNS OF CANDIDATE SOLUTIONS

With the tools described in the previous chapters, designs are generated based on a single element in an infinite array environment. These designs will serve as basis for the design of a subarray. The design of the subarray is described in chapter 7. The designs are obtained by optimisation with and without matching structure (irises in combination with a dielectric sheet). The optimisation is performed for rectangular as well as triangular array lattices. Optimisation parameters are obtained from the specifications [2, 3]:

- **Number of ports per subarray** : 2 (one per polarisation)
- **Frequency** : 5300 MHz
- **Bandwidth** : 100 MHz (operational)  
± 25 MHz (margin)
- **Scan volume** : ± 15 degees (elevation)  
± 2 degrees (azimuth)
- **Polarisation** : Dual polarisation H and V (baseline)  
with agility (TBC)
- **Co to cross polarisation for each scan direction for each port** : >30 dB
- **Input reflection coefficient for each port** : <-15 dB (<-20 dB goal)
- **Maximum value of active reflection coefficient over scan volume for each port** : <-12.5 dB (<-15 dB goal)
- **Ohmic losses in subarray** : <1 dB/m
- **Minimum element spacing** : 0.5 mm

Before optimisation is performed, we need to know the number of elements in one subarray, because this parameter will determine the allowable element spacings. After the size of the subarray is determined, 4 designs will be presented.

### 6.1 Number of elements in subarray

We start with expressing the *element* distance as fraction of  $\lambda$ :

$$d_{el} = \frac{\lambda}{i} \quad (6.1.1)$$

with  $i$  to be determined.

The *subarray* distances for elevation scanning and azimuth scanning are now given by:

$$d_{sub,el} = M \frac{\lambda}{i}; \text{elevation} \quad (6.1.2a)$$

with  $M$  the number of elements in the subarray in vertical direction.

$$d_{sub,c} = N \frac{\lambda}{j}; azimuth \quad (6.1.2b)$$

with  $N$  the number of elements in the subarray in horizontal direction.

The positions of the first grating lobe in elevation and azimuth, respectively, are given by [14]:

$$\sin(\vartheta_{el_g}) = \sin(\vartheta_{el_0}) - \frac{i}{M}; elevation \quad (6.1.3a)$$

$$\sin(\vartheta_{az_g}) = \sin(\vartheta_{az_0}) - \frac{j}{N}; azimuth \quad (6.1.3b)$$

In the above equations  $\vartheta_{el_g}$  and  $\vartheta_{az_g}$  are the positions of the first grating lobes in elevation and azimuth, respectively.  $\vartheta_{el_0}$  and  $\vartheta_{az_0}$  are the main beam positions in elevation and azimuth, respectively.

The assurance that the first grating lobes are positioned outside the scan volume for all main beam positions within this volume is not enough for determining the allowable number of elements in the subarray. We have to be sure that the level of the first grating lobe is sufficiently suppressed within the scan volume. Therefore we look at the angle where the subarray radiation pattern is 20 dB down. With use of [25], we find in first order approximation for this angle:

$$\vartheta_{el-20dB} = 52.03 \frac{i}{M} (\text{degrees}); elevation \quad (6.1.4a)$$

$$\vartheta_{az-20dB} = 52.03 \frac{j}{N} (\text{degrees}); azimuth \quad (6.1.4b)$$

In table 3, grating lobe angles (degrees) and -20dB angles (degrees) are given as function of the number of elements in the subarray and as function of  $i$  (elevation) or  $j$  (azimuth) for the main beam scanned to the maximum angle (15 degrees for elevation; 2 degrees for azimuth):

Table 3: Array angles as function of element spacing and number of elements

M(el.) or N(az.)	i (M) or j (N)	GL-angle el.	GL-angle az.	-20dB-angle
2	10/5	48	75	52
	10/6	35	53	43
	10/7	27	43	37
	10/8	21	36	33
3	10/5	24	39	34
	10/6	17	31	29
	10/7	13	26	25
	10/8	9.1	22	22
4	10/5	14	28	26
	10/6	9.1	22	22
	10/7	5.6	19	19
	10/8	3.1	16	16
5	10/5	8.1	21	21
	10/6	4.3	17	17
	10/7	1.5	15	15
	10/8	-	12	13
6	10/5	4.3	17	17
	10/6	1.1	14	14
	10/7	-	12	12
	10/8	-	10	11
7	10/5	1.5	15	15
	10/6		12	12
	10/7		9.7	11
	10/8		8.3	9.3
8	10/5		12	13
	10/6		10	11
	10/7		8.3	9.3
	10/8		7.0	8.1
9	10/5		11	12
	10/6		8.6	9.6
	10/7		7.1	8.3
	10/8		6.0	7.2

With the aid of the above table, we decide to use subarrays of 8 by 1 elements, horizontally orientated and with an element spacing around  $0.7\lambda$ .

## 6.2 Rectangular grid with matching structure

The antenna geometry is shown in figure 18; the dimensions obtained by optimisation are stated in table 4:

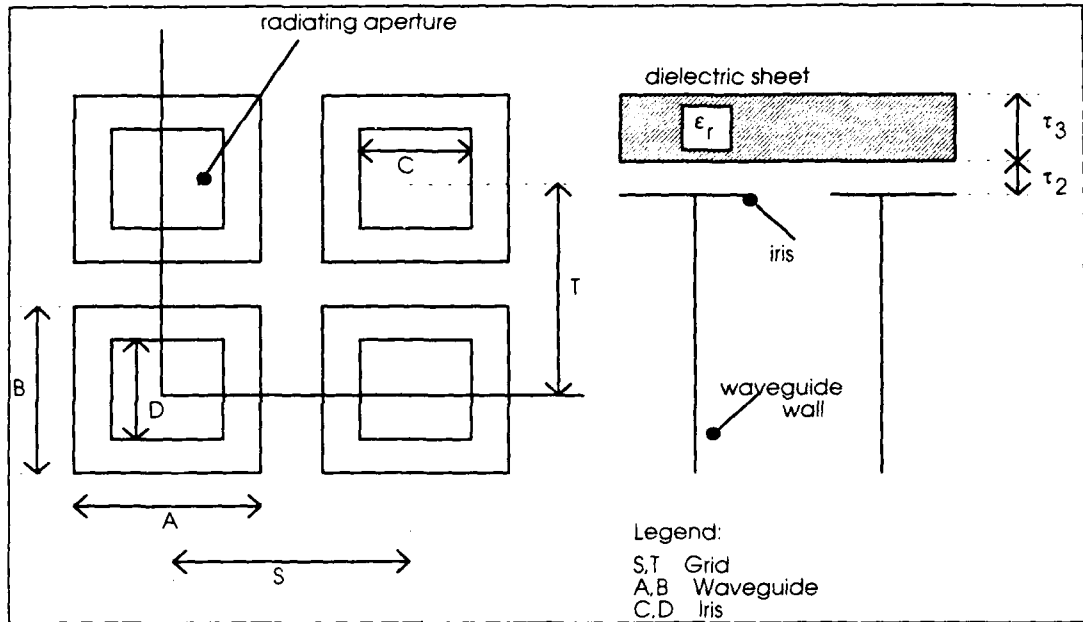


Figure 18: Antenna geometry

Table 4: Dimensions rectangular grid antenna with matching structure

S (mm)	36.26	D (mm)	22.14
T (mm)	36.26	$\tau_2$ (mm)	0.00
A (mm)	32.94	$\tau_3$ (mm)	0.77
B (mm)	32.94	$\epsilon_r$	6.36
C (mm)	22.14		

The worst case return loss for the two orthogonal polarisations as function of the frequency over the scan volume ( $\pm 15^\circ$  azimuth,  $\pm 2^\circ$  elevation) is shown in figure 19.

The worst case polarisation isolation for the two orthogonal polarisations as function of the frequency over the scan volume ( $\pm 15^\circ$  azimuth,  $\pm 2^\circ$  elevation) is shown in figure 20.

The 150 MHz bandwidth (operational with margins) is indicated with vertical lines.

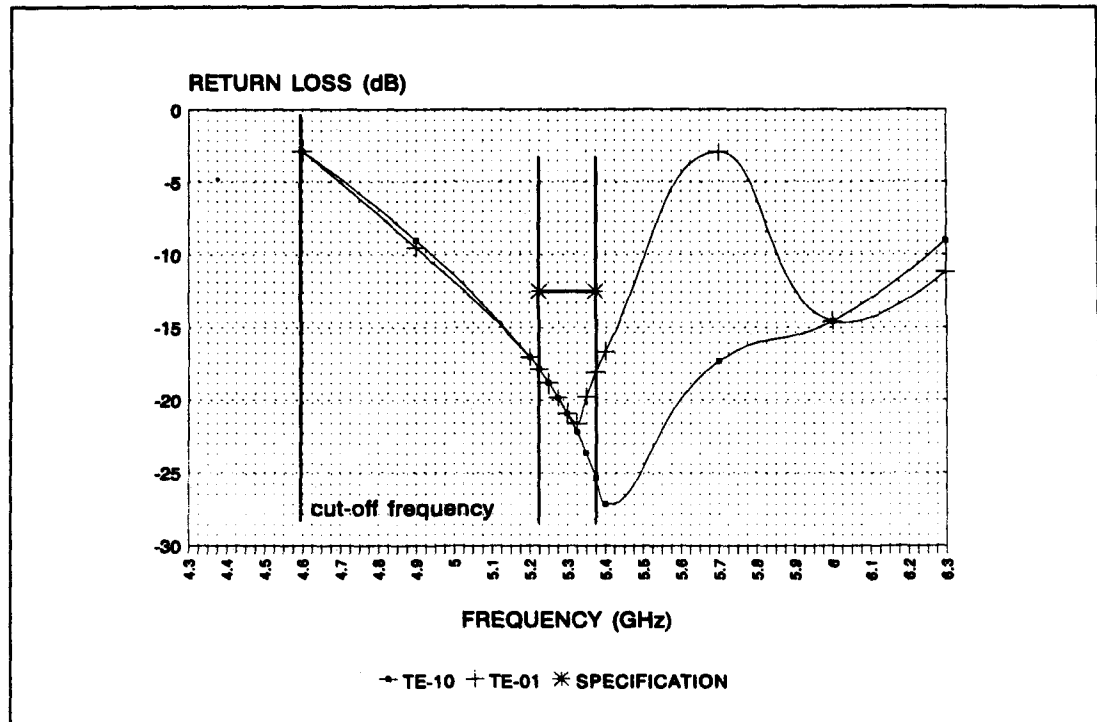


Figure 19: Worst case return loss over scan volume vs frequency; rectangular grid with matching structure



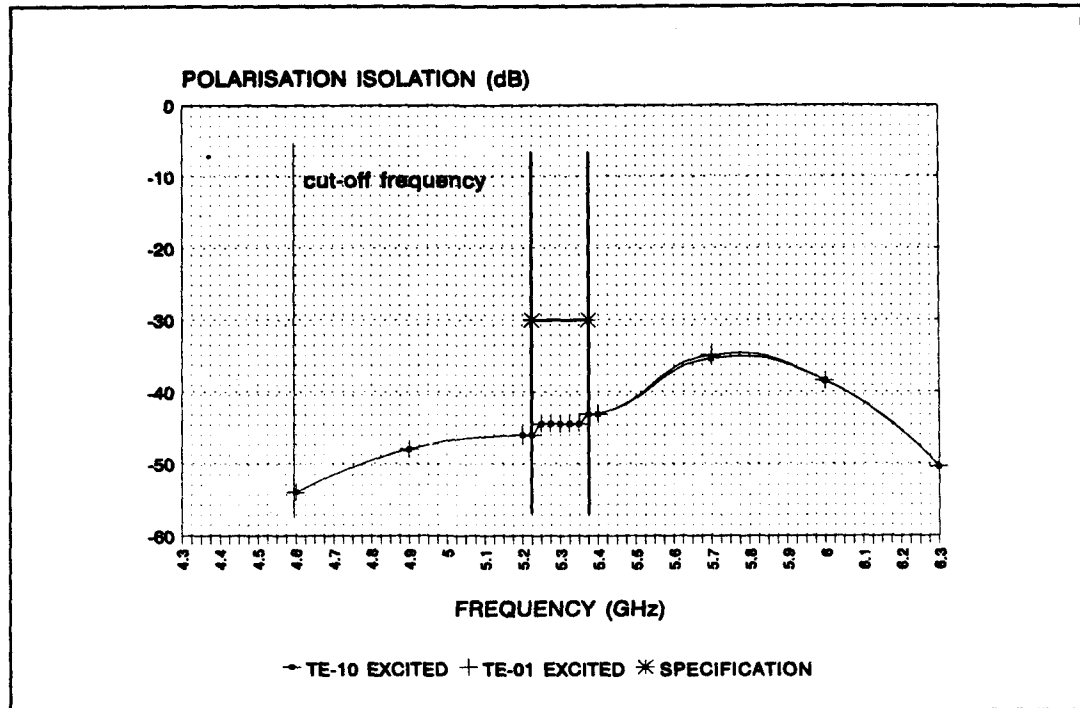


Figure 20: Worst case polarisation isolation over scan volume vs frequency; rectangular grid with matching structure

### 6.3 Rectangular grid without matching structure

The antenna geometry is shown in figure 21; the dimensions obtained by optimisation are stated in table 5:

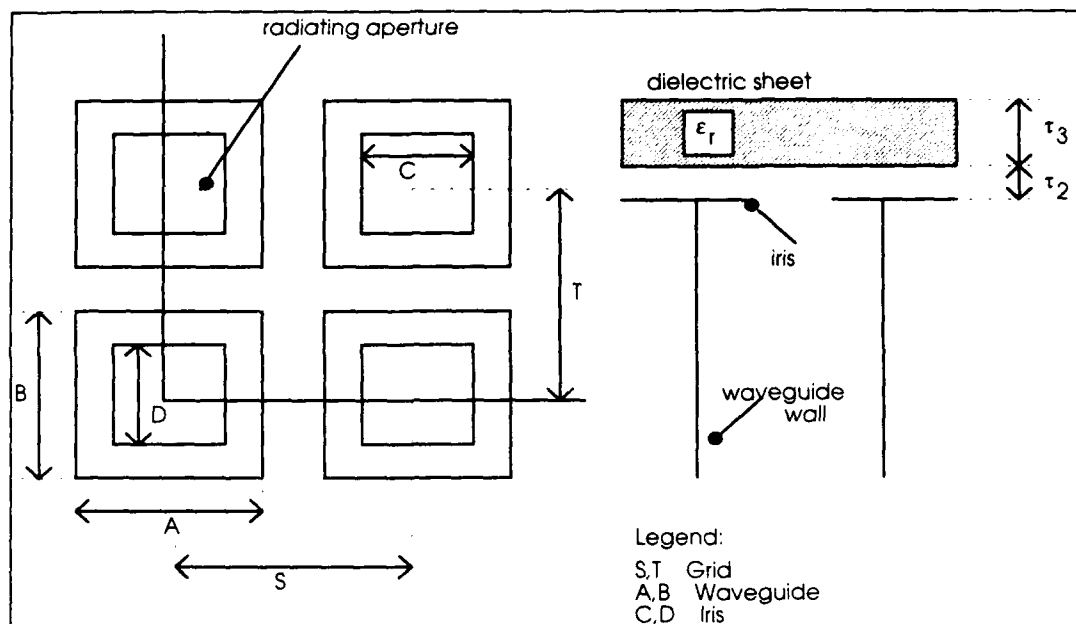


Figure 21: Antenna geometry

Table 5: Dimensions rectangular grid antenna without matching structure

S (mm)	39.60	D (mm)	35.88
T (mm)	39.60	$\tau_2$ (mm)	0.00
A (mm)	35.88	$\tau_3$ (mm)	0.00
B (mm)	35.88	$\epsilon_r$	
C (mm)	35.88		

The worst case return loss for the two orthogonal polarisations as function of the frequency over the scan volume ( $\pm 15^\circ$  azimuth,  $\pm 2^\circ$  elevation) is shown in figure 22.

The worst case polarisation isolation for the two orthogonal polarisations as function of the frequency over the scan volume ( $\pm 15^\circ$  azimuth,  $\pm 2^\circ$  elevation) is shown in figure 23.

The 150 MHz bandwidth (operational with margins) is indicated with vertical lines.

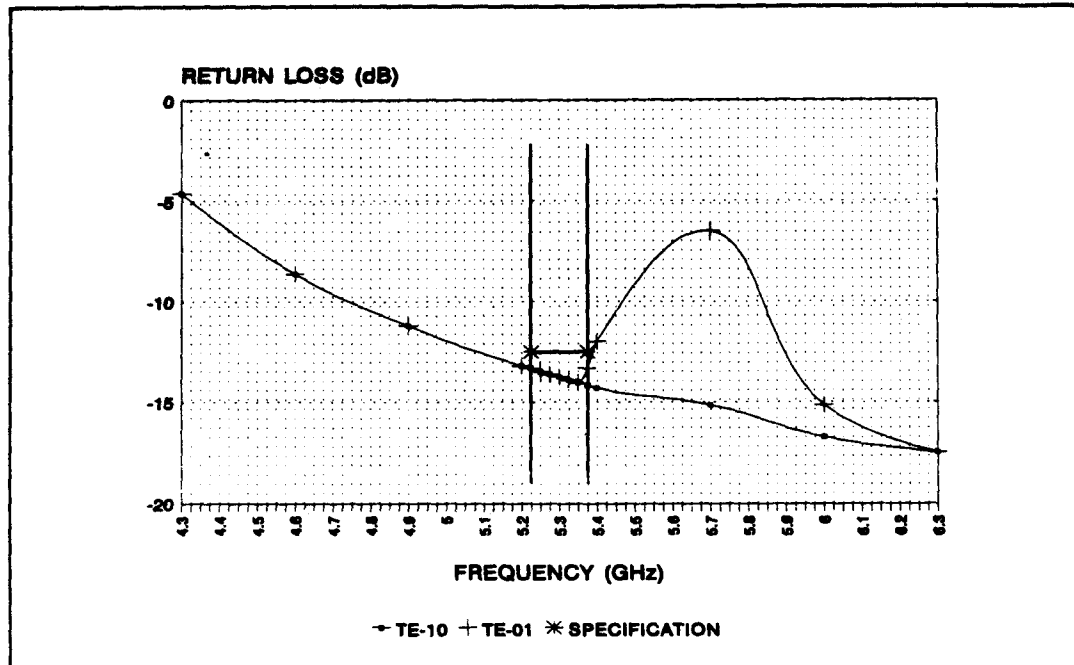


Figure 22: Worst case return loss over scan volume vs frequency; rectangular grid without matching structure

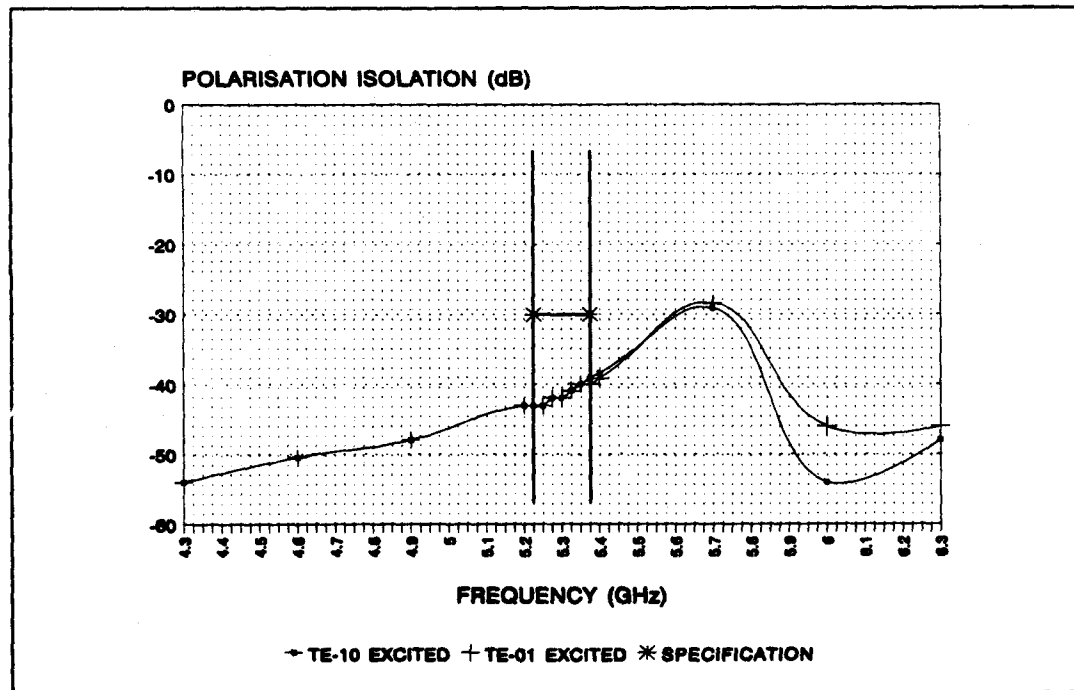


Figure 23: Worst case polarisation isolation over scan volume vs frequency; rectangular grid without matching structure

### 6.4 Triangular grid with matching structure

The antenna geometry is shown in figure 24; the dimensions obtained by optimisation are stated in table 6:

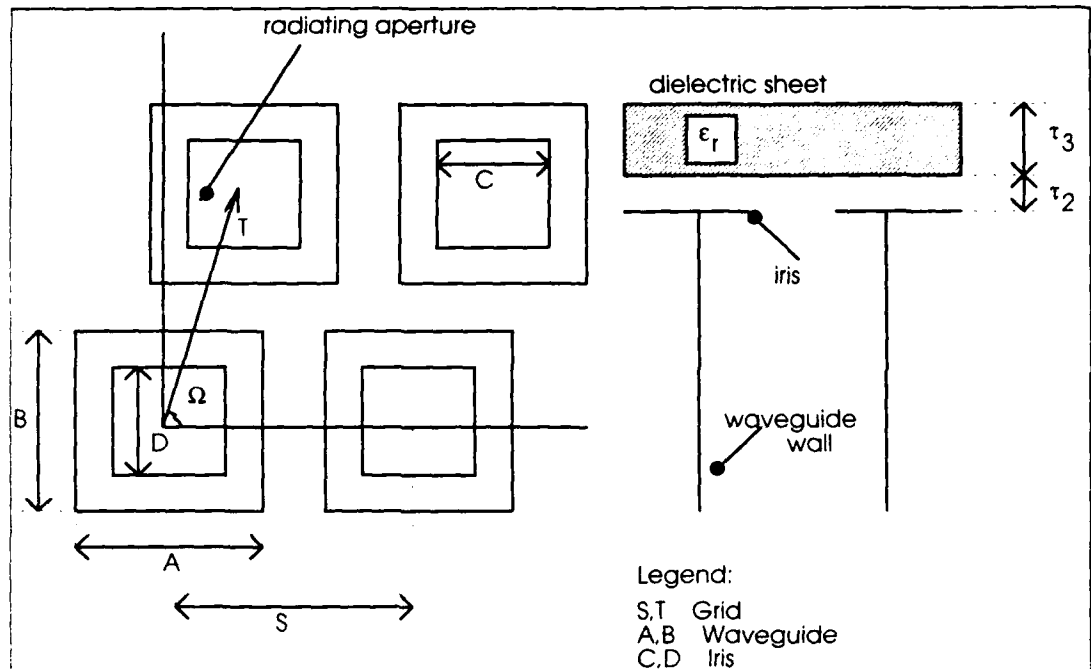


Figure 24: Antenna geometry

Table 6: Dimensions rectangular grid antenna with matching structure

S (mm)	37.87	D (mm)	21.47
T (mm)	37.50	$\tau_2$ (mm)	0.00
A (mm)	32.94	$\tau_3$ (mm)	0.95
B (mm)	32.94	$\epsilon_r$	5.58
C (mm)	21.47	$\Omega$ (degrees)	69.41

The worst case return loss for both orthogonal polarisations as function of the frequency over the scan volume ( $\pm 15^\circ$  azimuth,  $\pm 2^\circ$  elevation) is shown in figure 25.

The worst case polarisation isolation for both orthogonal polarisations as function of the frequency over the scan volume ( $\pm 15^\circ$  azimuth,  $\pm 2^\circ$  elevation) is shown in figure 26.

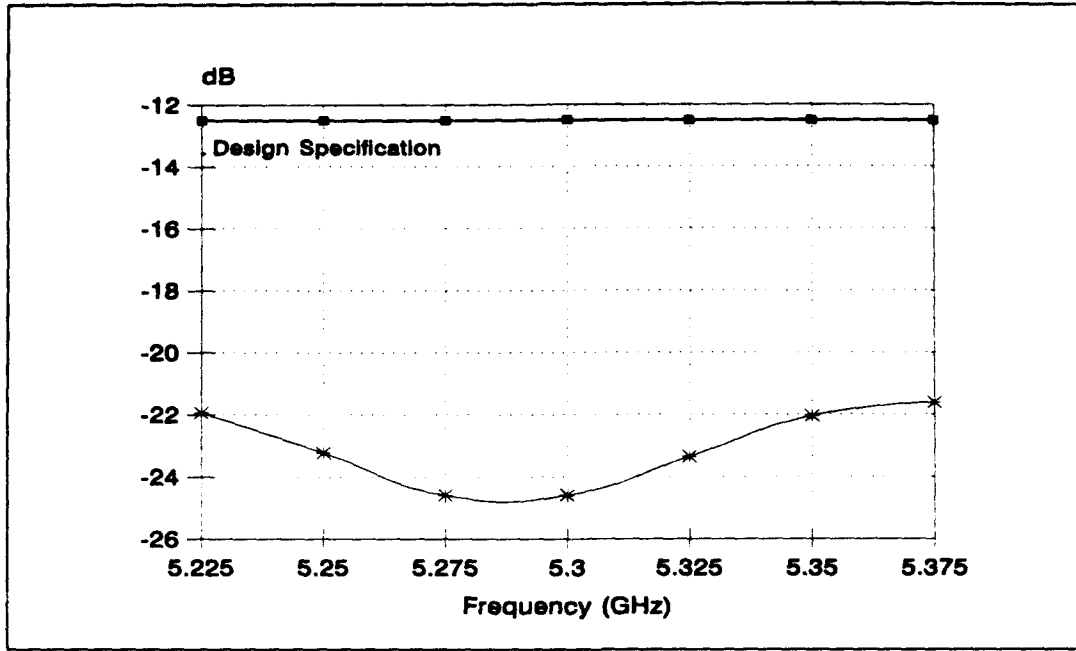


Figure 25: Worst case return loss over scan volume vs frequency; triangular grid with matching structure

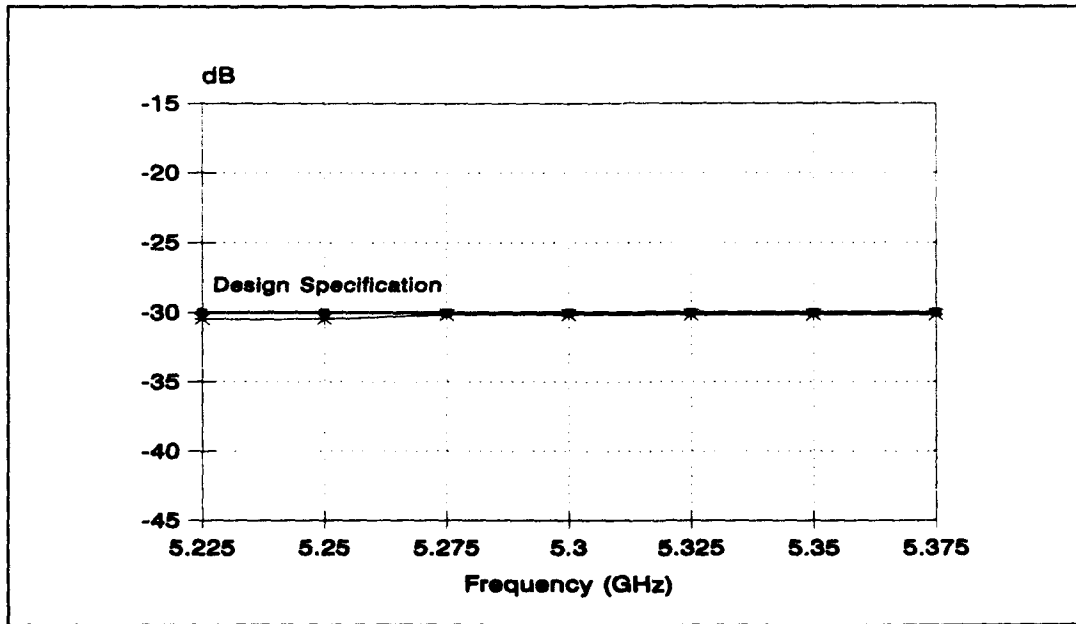


Figure 26: Worst case polarisation isolation over scan volume vs frequency; triangular grid with matching structure

### 6.5 Triangular grid without matching structure

The antenna geometry is shown in figure 27; the dimensions obtained by optimisation are stated in table 7:

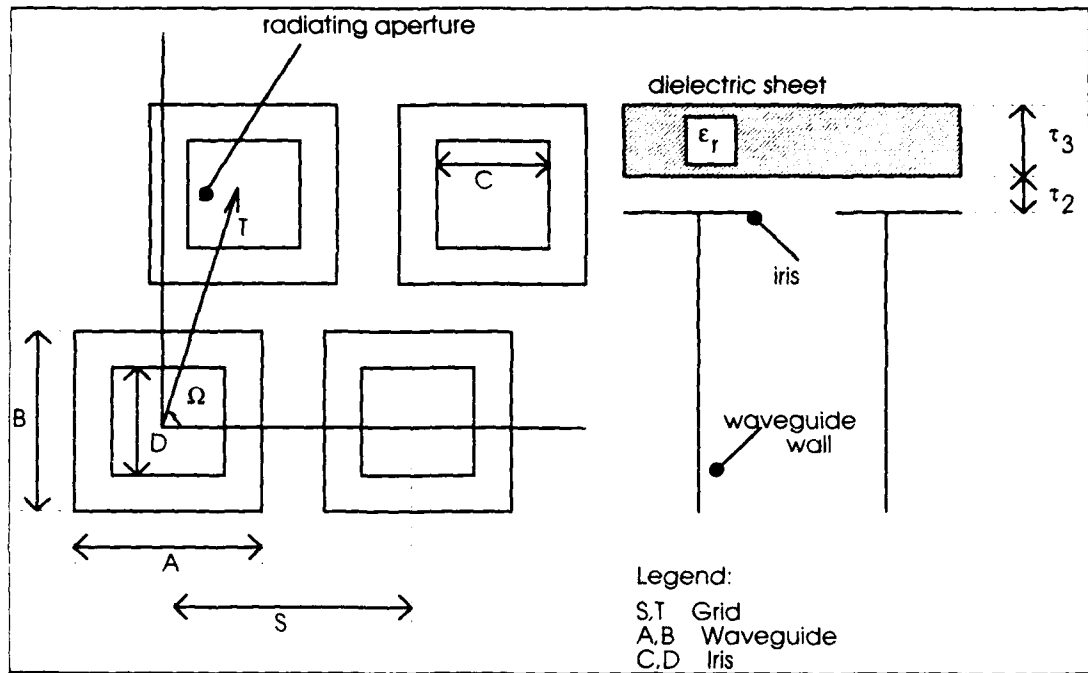


Figure 27: Antenna geometry

Table 7: Dimensions rectangular grid antenna with matching structure

S (mm)	39.60	D (mm)	37.00
T (mm)	43.84	$\tau_2$ (mm)	0.00
A (mm)	37.00	$\tau_3$ (mm)	0.00
B (mm)	37.00	$\epsilon_r$	
C (mm)	37.00	$\Omega$ (degrees)	62.76

The worst case return loss for both orthogonal polarisations as function of the frequency over the scan volume ( $\pm 15^\circ$  azimuth,  $\pm 2^\circ$  elevation) is shown in figure 28.

The worst case polarisation isolation for both orthogonal polarisations as function of the frequency over the scan volume ( $\pm 15^\circ$  azimuth,  $\pm 2^\circ$  elevation) is shown in figure 29.

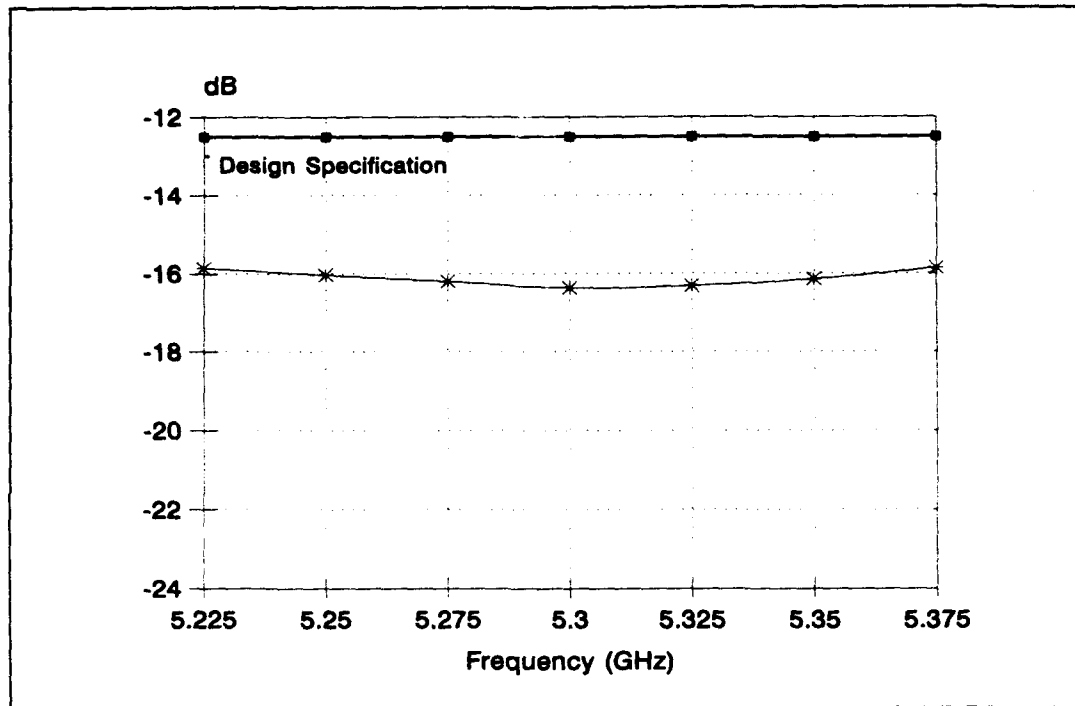


Figure 28: Worst case return loss over scan volume vs frequency; triangular grid without matching structure

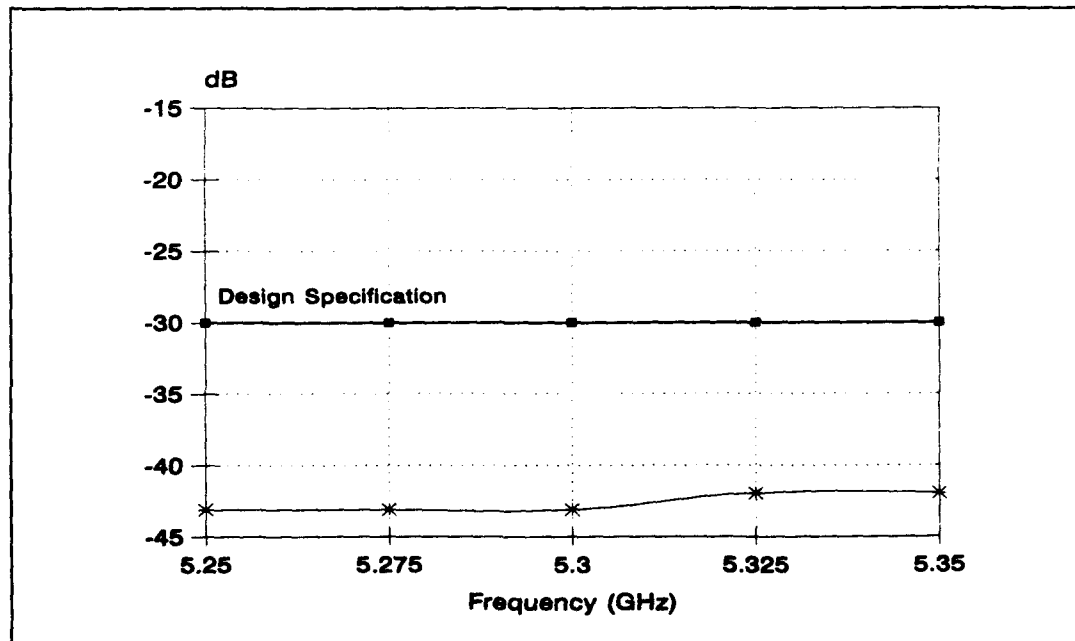


Figure 29: Worst case polarisation isolation over scan volume vs frequency; triangular grid without matching structure

## 7 DESIGN OF THE SUBARRAY

With the results presented in chapter 6 as basis we can design a subarray to be used in the SAR antenna. In order to reduce the costs of the antenna, phase shifting on element to element basis is not recommended. Due to the limited scan volume, elements can be grouped in subarrays.

In the following the subarray design method, using the software described in the foregoing will be described and finally some subarray designs will be presented.

From now on, triangular lattices will not be taken into account any more because of the problems that will arise due to the gaps that will appear at the tile boarders.

### 7.1 Subarray design strategy

Figure 30 shows an array composed of 8x1 subarrays. Elements in the centre subarray are numbered from 1 to 8:

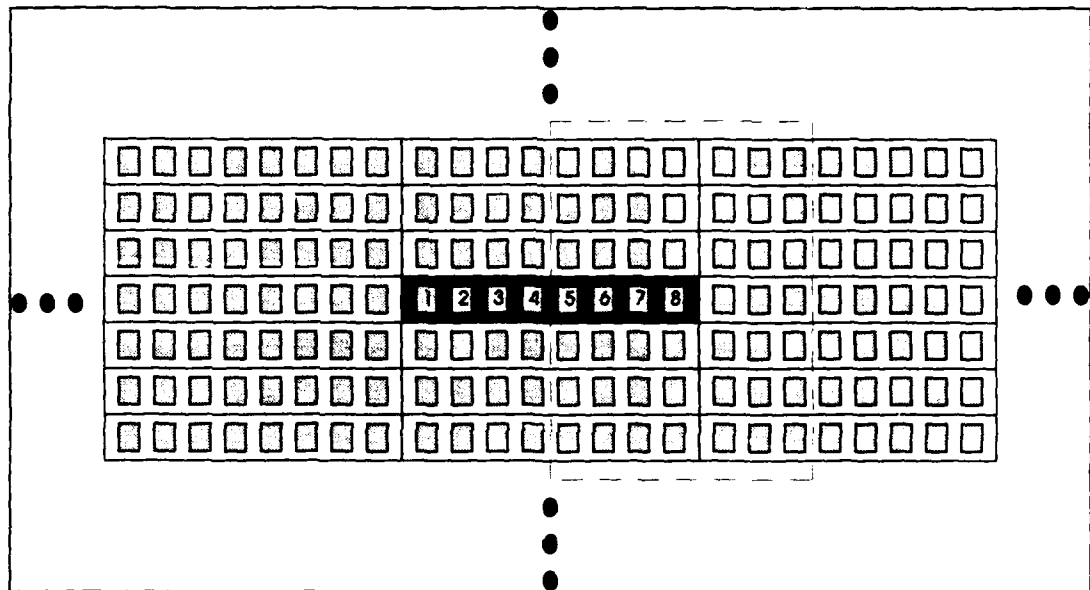


Figure 30: Centre subarray in array environment

To calculate the centre subarray reflection coefficient, three steps need to be performed:

- 1. Calculate the coupling coefficients for a finite set of elements using infinite array data.
- 2. Recalculate the reflection coefficient for element  $i$ ;  $i = 1, 2, \dots, 8$ . In other words: Sum the coupling coefficients within a window around each element with the appropriate subarray phase factors. (Figure 18 shows a 7x7 window for element 8).
- 3. Combine the so obtained element in subarray reflection coefficients to get the overall subarray reflection coefficient.



Step 1 is obvious: Apply a two dimensional Fourier transformation on the infinite array reflection coefficients to obtain a finite set of coupling coefficients. Step 2 needs some further explanation:

Since phaseshifters are applied on subarray level, equation (3.5.2) needs to be modified. The element in subarray reflection coefficient is now given by:

$$\Gamma_i(\vartheta_0, \varphi_0) = \sum_{m=-M}^M \sum_{n=-N}^N S(m, n) e^{-j\Psi_{msub}} e^{-j\Psi_{nsub}}; i = 1, 2, \dots, 8 \quad (7.1.1)$$

with:

$$\Psi_{msub} = \Psi_x \cdot (8d_x) \cdot msub \quad (7.1.2a)$$

$$\Psi_{nsub} = \Psi_y \cdot d_y \cdot nsub \quad (7.1.2b)$$

and:

$$\Psi_x = k_0 \sin(\vartheta_0) \cos(\varphi_0) \quad (7.1.3a)$$

$$\Psi_y = k_0 \sin(\vartheta_0) \sin(\varphi_0) \quad (7.1.3b)$$

$$k_0 = \frac{2\pi}{\lambda} \quad (7.1.3c)$$

Further:

$$nsub = n \quad (7.1.4a)$$

$$msub = \begin{cases} a & \text{if } (m \geq 0) \wedge \left( a < \frac{i+m}{8} \leq b \right); a, b \in \mathbf{N} \\ c & \text{if } (m \leq 0) \wedge \left( c < \frac{i+m}{8} \leq d \right); c, d \in \mathbf{N} \end{cases} \quad (7.1.4b)$$

With this design strategy, the subarray reflection coefficient for the element presented in paragraph 6.2, using an ideal combining network, was calculated as function of scan angles  $\theta_0$  and  $\varphi_0$  for a frequency of 5.3 GHz. A 63x63 window was applied. The results are shown in figure 31:

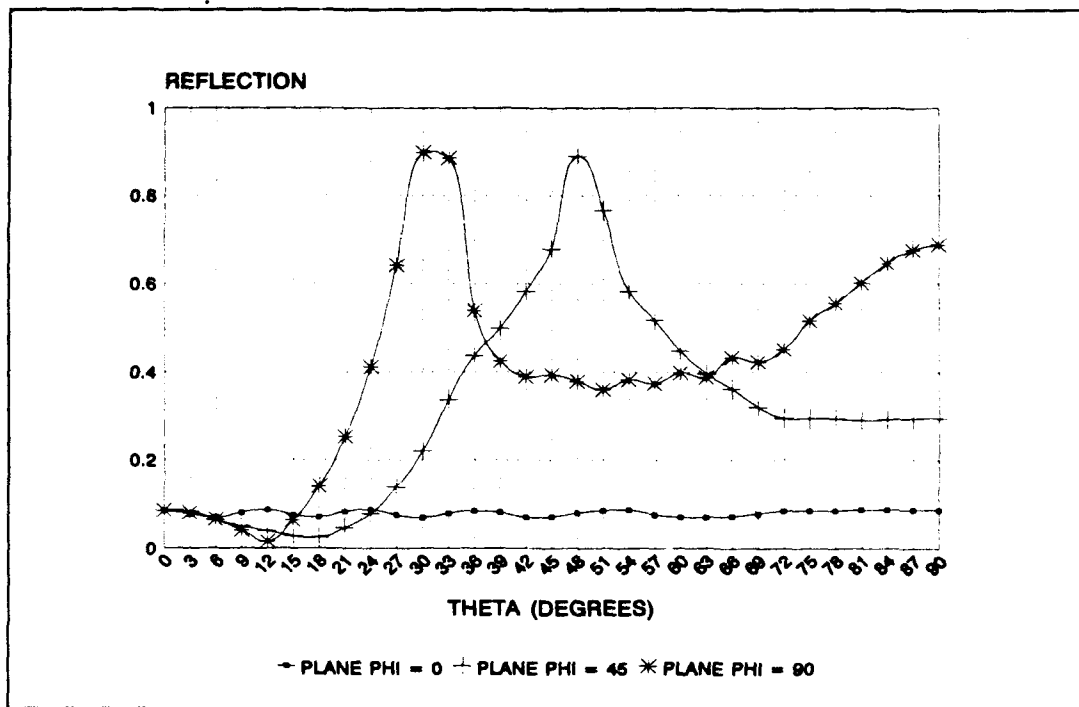


Figure 31: Amplitude subarray reflection coefficients vs scan angles,  $f = 5.3\text{GHz}$ ,  $TE_{10}$ -mode polarisation

As a check, comparison with figures 8,9,10 shows that the reflection coefficient at broadside is the same as for an element in an array scanned on element to element basis. This is in agreement with the expectations.

Also note that the reflection coefficient in the plane  $\varphi_0=90$  degrees is the same as the reflection coefficient shown in figure 8 where phaseshifters were applied on element to element basis. This too is in agreement with the expectations, since in the plane  $\varphi_0=90$  degrees nothing has changed due to the width of the subarray (1 element). Of course the behaviour in the planes  $\varphi_0=0$  and  $\varphi_0=45$  has changed in respect with the situation in which phaseshifters were applied on element to element basis.

In order to demonstrate the influence of the coupling coefficients, subarray reflection coefficients as function of the scan angles, for this particular design, are shown in figure 32 for different applied window sizes:

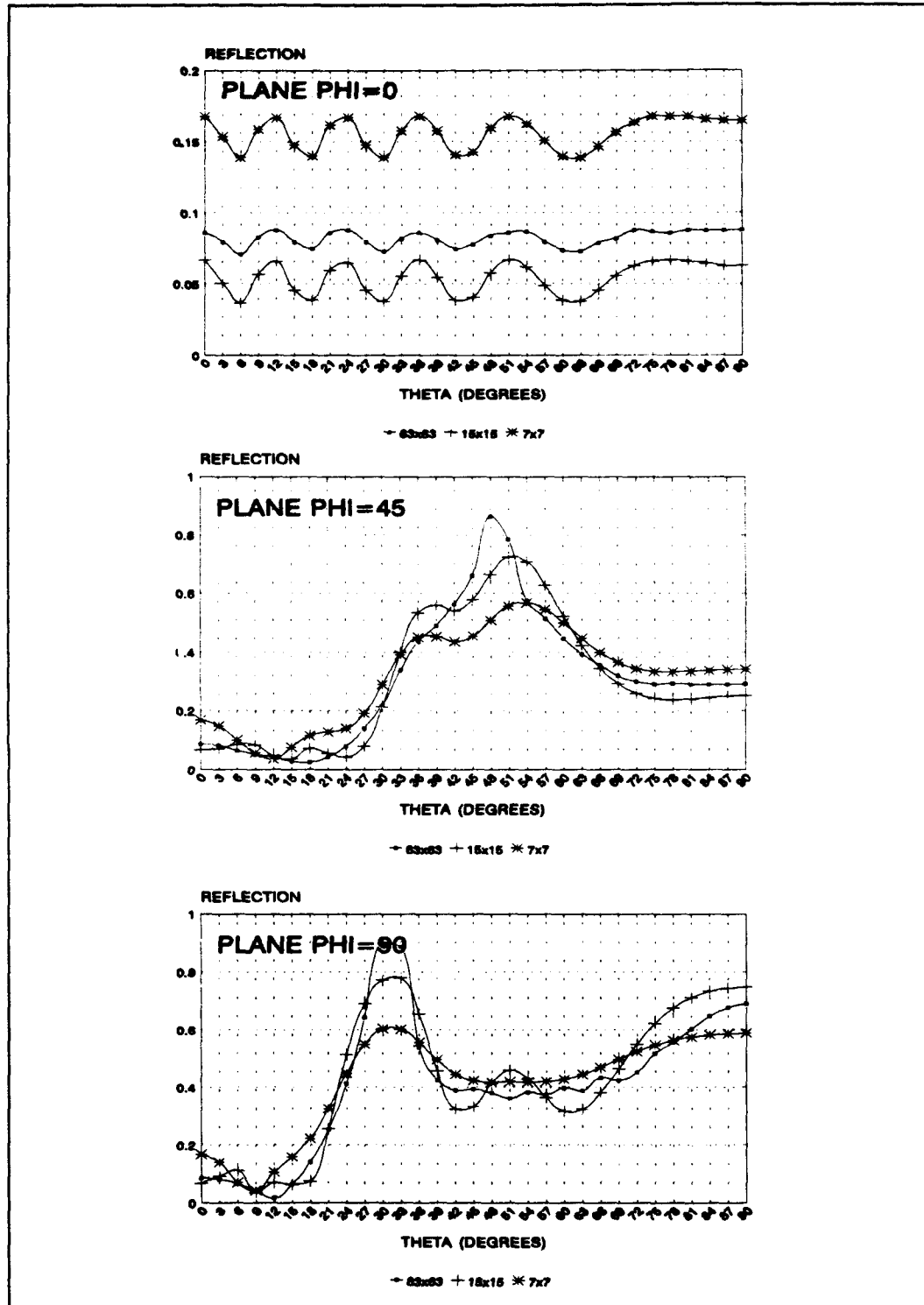


Figure 32: Amplitude subarray reflection coefficients vs scan angles for different applied window sizes;  $f = 5.3\text{GHz}$ ,  $TE_{10}$ -mode polarisation

The above figure shows again that adding more elements leads to a higher fluctuation frequency and a lower fluctuation amplitude.

The figure also shows the importance of taking enough coupling coefficients in consideration. The figure gives the impression that when only the coupling coefficients within the centre subarray are taken into account, highly erroneous reflection coefficients will result.

To test this assumption, the centre subarray reflection coefficients as function of the scan angles are calculated taking into account only the coupling coefficients within this subarray. The results, together with the results when a 63x63 window is applied are shown in figure 33.

The results clearly show the validity of the above stated assumption. Thus:

**One can not design a phased array antenna that is scanned on subarray level, taking into account only the isolated subarray behaviour, even when this isolated subarray shows the same behaviour as one isolated element. The element to element coupling may be low, but due to the size of the complete phased array antenna, inclusion of total array coupling behaviour is of paramount importance!**

To demonstrate that the above statement is more or less radiator type independent, we performed a similar analysis on a microstrip patch array antenna.

With coupling coefficients of a 7x7 single polarisation, single layer, probe fed microstrip patch array antenna, we calculated the reflection coefficient of an embedded 4x1 subarray and the reflection coefficient of an isolated 4x1 subarray<sup>1</sup>. The results are shown in figure 34 for a frequency of 3 GHz. Element distances are 50 mm, the thickness of the dielectric substrate ( $\epsilon_r=2.94$ ) is 6 mm.

Comparison of figures 33 and 34 shows that for an element optimised in an infinite array environment, the embedded subarray reflection coefficient is better than the isolated subarray reflection coefficient, proving the validity of our design strategy.

---

<sup>1</sup> These coupling coefficients were kindly supplied by A.B. Smolders, Electromagnetics Division, Faculty of Electrical Engineering, Eindhoven University of Technology, P.O. Box 513, 5600 MB Eindhoven, The Netherlands.

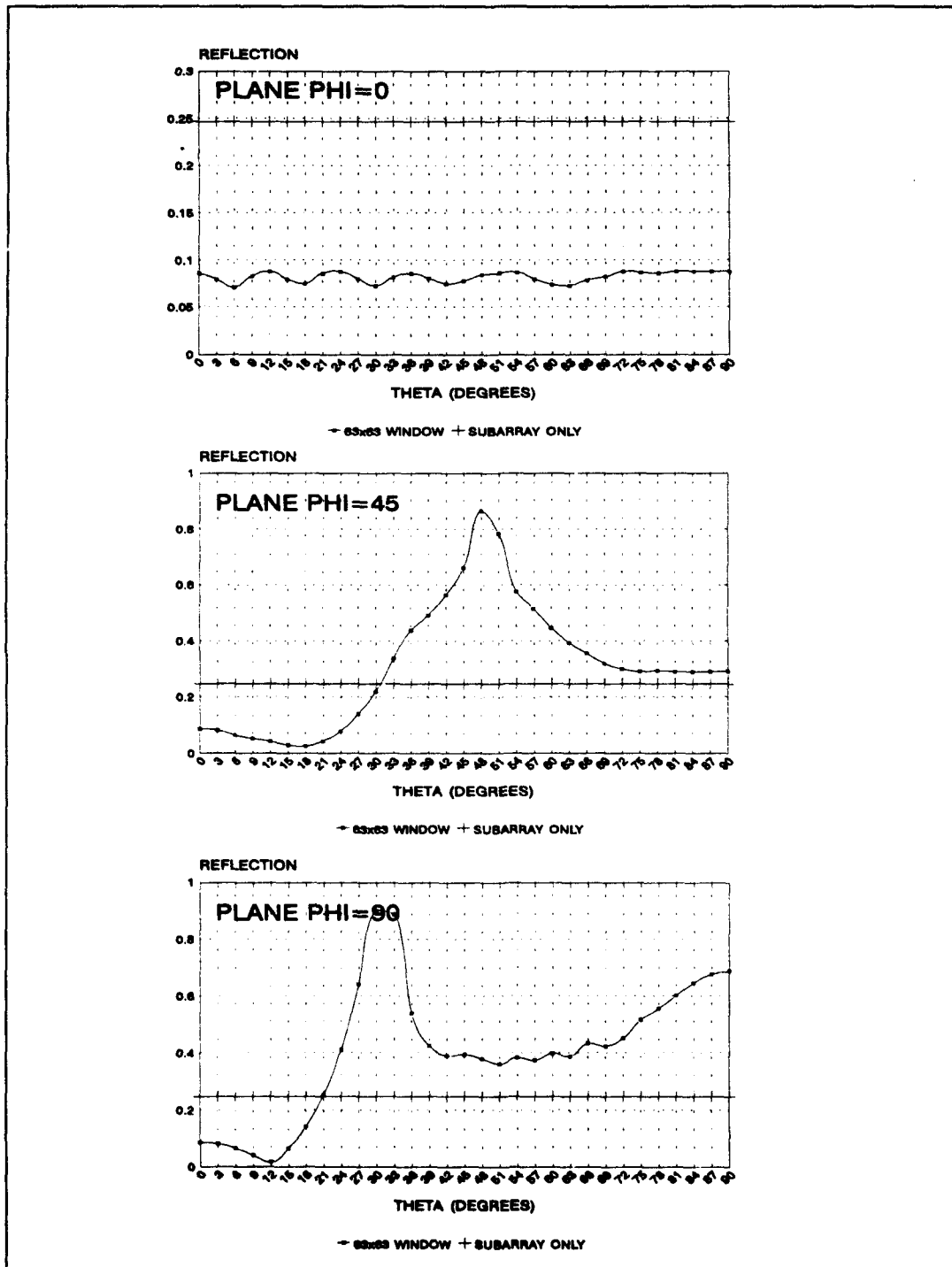


Figure 33: Amplitude waveguide subarray reflection coefficients vs scan angles, with and without taking into account the array environment;  $f = 5.3\text{GHz}$ ,  $TE_{10}$ -mode polarisation,  $8 \times 1$  subarray

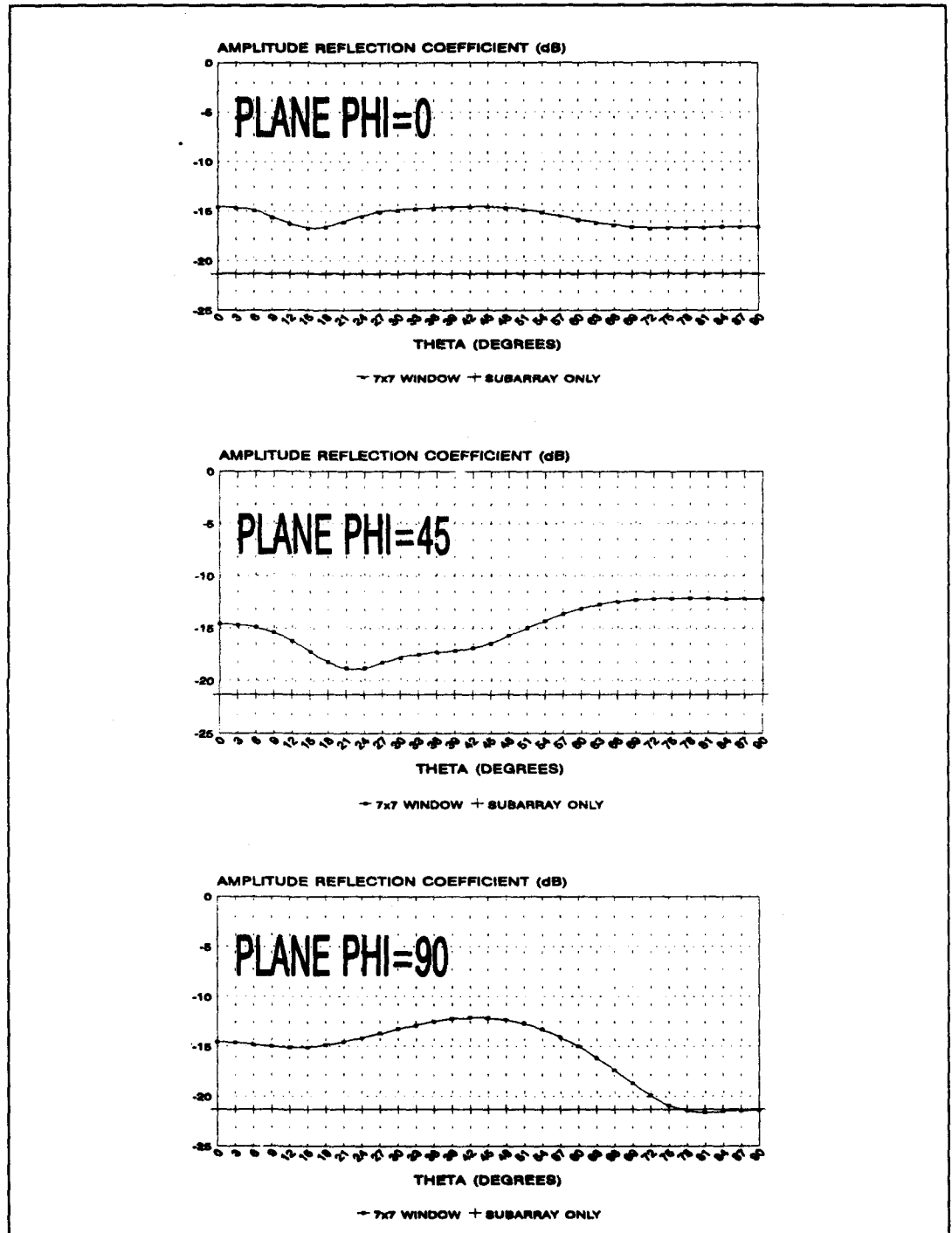


Figure 34: Amplitude patch antenna subarray reflection coefficients vs scan angles, with and without taking into account the array environment;  $f = 3\text{GHz}$ ,  $TE_{10}$ -mode polarisation,  $4 \times 1$  subarray

## 7.2 Subarray designs

Because in the subarray designs to be presented, co and cross polarisation radiation patterns will be shown, we start with a brief discussion on the calculation of co and cross polarisation behaviour. These radiation patterns are based on radiation patterns of a singly excited element in an infinite array environment. We present this discussion, because of the fact that calculating the radiation pattern of a singly excited element in an infinite array environment - bearing in mind that our analysis program is based on a uniform excited infinite array - is not at all that obvious.

### 7.2.1 Co and cross polarisation analysis method

Use will be made of the fact that by taking a Fourier series transform of the field solution for the infinitely excited array one may obtain, uniquely, the field solution for the singly excited element in the environment of the array [26]. More precisely: If a Fourier analysis is made of the aperture fields of an active infinite array, which by Floquet's theorem are periodic functions of the steering angles, the  $m$ th Fourier coefficient is then the aperture fields across the  $m$ th element when the zeroth element is excited alone [27].

#### 7.2.1.1 Aperture fields

Started is with the Huygen's principle, see figure 35:

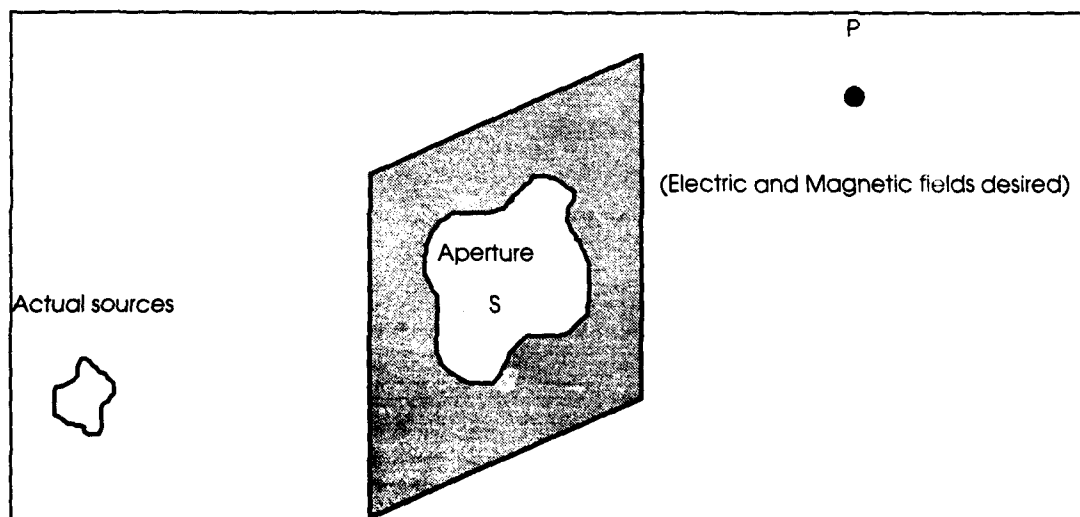


Figure 35: Radiation through an aperture; Huygens' principle

The tangential components of the electric and magnetic fields in the aperture need to be known. Although these fields arise from sources to the left, they may be considered to be produced by equivalent sources located in the aperture plane. The fields are described by [28];

$$\vec{E} = -j\omega\vec{A} - \frac{j\omega}{k^2}\nabla(\nabla\cdot\vec{A}) - \frac{1}{\epsilon}\nabla\times\vec{F} \quad (7.2.1)$$

with:

$$\vec{A} = \mu \frac{e^{-jkr}}{4\pi r} \vec{N} \quad (7.2.2a)$$

$$\vec{F} = \epsilon \frac{e^{-jkr}}{4\pi r} \vec{L} \quad (7.2.2b)$$

$$\vec{N} = \int_S \vec{J}_s e^{+jkr\cos(\Psi')} dS \quad (7.2.3a)$$

$$\vec{L} = \int_S \vec{M}_s e^{+jkr\cos(\Psi')} dS \quad (7.2.3b)$$

$$\vec{J}_s = \hat{n}\times\vec{H} \quad (7.2.4a)$$

$$\vec{M}_s = -\hat{n}\times\vec{E} \quad (7.2.4b)$$

with  $\vec{E}$  the electric field,  $\vec{A}$  and  $\vec{F}$  retarded magnetic and electric vector potentials,  $\vec{L}$  and  $\vec{N}$  magnetic and electric radiation vectors,  $\vec{M}_s$  and  $\vec{J}_s$  surface magnetic and electric currents and  $k$  the wavenumber:

$$k = \frac{2\pi}{\lambda} \quad (7.2.5)$$

$\hat{n}$  is a unit vector normal to the aperture plane.  $r'$  and  $\Psi'$  are defined in figure 36 [28]:



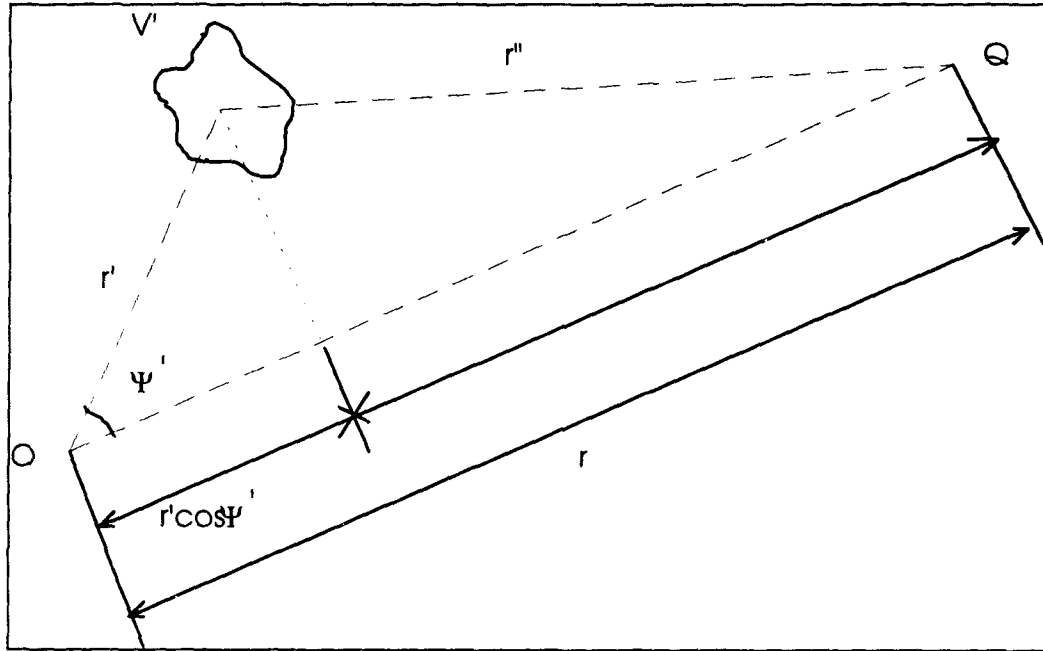


Figure 36: Coordinates of a general current element in the volume  $V'$  and a distant point  $Q$ , where fields are to be evaluated, with respect to an origin of coordinates near the sources

### 7.2.1.2 Infinite waveguide array

When the waveguide properties are described in a Cartesian  $x,y,z$ -coordinate system, with the wave propagation directed along the  $z$ -axis, equation (7.3.4a) can be written as:

$$\vec{J}_S = \hat{n} \times \vec{H} = -H_y \hat{e}_x + H_x \hat{e}_y = J_{sx} \hat{e}_x + J_{sy} \hat{e}_y \quad (7.2.6)$$

The tangential magnetic field strengths (the Fourier coefficients mentioned in paragraph 7.2.1) are given by equations (3.3.27) and (3.3.28):

$$H_{x,pq} = \left( -\gamma^{(4)}_{pq} \mu_{p0} T^{(4)+}_{pq} + \omega \epsilon_{r_4} \epsilon_0 \nu_{pq} \bar{T}^{(4)+}_{pq} \right) X_{pq} / k_{T,pq}^2 \quad (7.2.7a)$$

$$H_{y,pq} = \left( -\gamma^{(4)}_{pq} \nu_{pq} T^{(4)+}_{pq} - \omega \epsilon_{r_4} \epsilon_0 \mu_{p0} \bar{T}^{(4)+}_{pq} \right) X_{pq} / k_{T,pq}^2 \quad (7.2.7b)$$

with:

$$X_{pq} = e^{-j(\mu_{p0}x + \nu_{q0}y)} \quad (7.2.8)$$

and the other quantities defined in chapter 3 and [12].

Equation (7.2.8) is a phased array term, related to the element positions in the array, and is only valid for discrete x and y.

Now, we want to calculate the radiation pattern of the singly excited unit cell in the infinite array environment. Since antennas are designed such that only one grating mode is radiating in free space, we take  $p=q=0$ . Since we look at the unit cell, we take  $x=y=0$ . This yields:

$$H_x = \left( -\gamma^{(4)}_{00} \mu_{00} T^{(4)+}_{00} + \omega \epsilon_{r_4} \epsilon_0 \nu_{00} \bar{T}^{(4)+}_{00} \right) / k_{T_{00}}^2 \quad (7.2.9a)$$

$$H_y = \left( -\gamma^{(4)}_{00} \nu_{00} T^{(4)+}_{00} - \omega \epsilon_{r_4} \epsilon_0 \mu_{00} \bar{T}^{(4)+}_{00} \right) / k_{T_{00}}^2 \quad (7.2.9b)$$

Since our origin is placed in the aperture plane, we take  $r'=\Psi'=0$  in equation (7.2.3a). With unit cell area  $s.t.\sin(\Omega)$  (see chapter 3) and use of equations (7.2.2a), (7.2.3a), (7.2.6) and (7.2.9):

$$\bar{A} = \mu_0 \cdot s.t.\sin(\Omega) \frac{e^{-jkr}}{4\pi r} \left\{ \frac{\gamma^{(4)}_{00} \nu_{00} T^{(4)+}_{00} + \omega \epsilon_{r_4} \epsilon_0 \mu_{00} \bar{T}^{(4)+}_{00}}{k_{T_{00}}^2} \hat{e}_x - \frac{\gamma^{(4)}_{00} \mu_{00} T^{(4)+}_{00} - \omega \epsilon_{r_4} \epsilon_0 \nu_{00} \bar{T}^{(4)+}_{00}}{k_{T_{00}}^2} \hat{e}_y \right\} \quad (7.2.10)$$

Since  $\nabla \times \bar{F} = \bar{0}$  and  $\nabla \cdot \bar{A} = 0$ , equation (7.3.1) reduces to:

$$\bar{E} = -j\omega \bar{A} \quad (7.2.11)$$

So, finally:

$$E_x = -j\omega A_x = -j\omega \mu_0 \cdot s.t.\sin(\Omega) \cdot \frac{e^{-jkr}}{4\pi r} \cdot \frac{\gamma^{(4)}_{00} \nu_{00} T^{(4)+}_{00} + \omega \epsilon_{r_4} \epsilon_0 \mu_{00} \bar{T}^{(4)+}_{00}}{k_{T_{00}}^2} \quad (7.2.12a)$$

$$E_y = -j\omega A_y = +j\omega \mu_0 \cdot s.t.\sin(\Omega) \cdot \frac{e^{-jkr}}{4\pi r} \cdot \frac{\gamma^{(4)}_{00} \mu_{00} T^{(4)+}_{00} - \omega \epsilon_{r_4} \epsilon_0 \nu_{00} \bar{T}^{(4)+}_{00}}{k_{T_{00}}^2} \quad (7.2.12b)$$

$$E_z = -j\omega A_z = 0 \quad (7.2.12c)$$

### 7.2.1.3 Co and cross polarisation

Applying Ludwig's third definition [29] and omitting the terms  $\exp(-jkr)/4\pi r$ , we get, after normalisation:

$$E_{copol} = +\{1 - \cos(\vartheta)\} \sin(\varphi) \cos(\varphi) \cdot \frac{\omega}{k_{T_{in}}^2} \cdot \left( \gamma^{(4)}_{00} v_{00} T^{(4)+}_{00} + \omega \epsilon_{r_4} \epsilon_0 u_{00} \bar{T}^{(4)+}_{00} \right) + \\ \{1 - \sin^2(\varphi)(1 - \cos(\vartheta))\} \cdot \frac{\omega}{k_{T_{in}}^2} \cdot \left( \gamma^{(4)}_{00} u_{00} T^{(4)+}_{00} - \omega \epsilon_{r_4} \epsilon_0 v_{00} \bar{T}^{(4)+}_{00} \right) \quad (7.2.13a)$$

$$E_{cpol} = -\{1 - \cos^2(\varphi)(1 - \cos(\vartheta))\} \cdot \frac{\omega}{k_{T_{in}}^2} \cdot \left( \gamma^{(4)}_{00} v_{00} T^{(4)+}_{00} + \omega \epsilon_{r_4} \epsilon_0 u_{00} \bar{T}^{(4)+}_{00} \right) + \\ -(1 - \cos(\vartheta)) \sin(\varphi) \cos(\varphi) \cdot \frac{\omega}{k_{T_{in}}^2} \cdot \left( \gamma^{(4)}_{00} u_{00} T^{(4)+}_{00} - \omega \epsilon_{r_4} \epsilon_0 v_{00} \bar{T}^{(4)+}_{00} \right) \quad (7.2.13b)$$

Figure 37 shows measured and calculated active element co and crosspolarisation radiation patterns for the EXPAR test antenna (see chapter 4) in the worst case plane ( $f = f_2$ , plane  $\varphi = 55$  degrees):

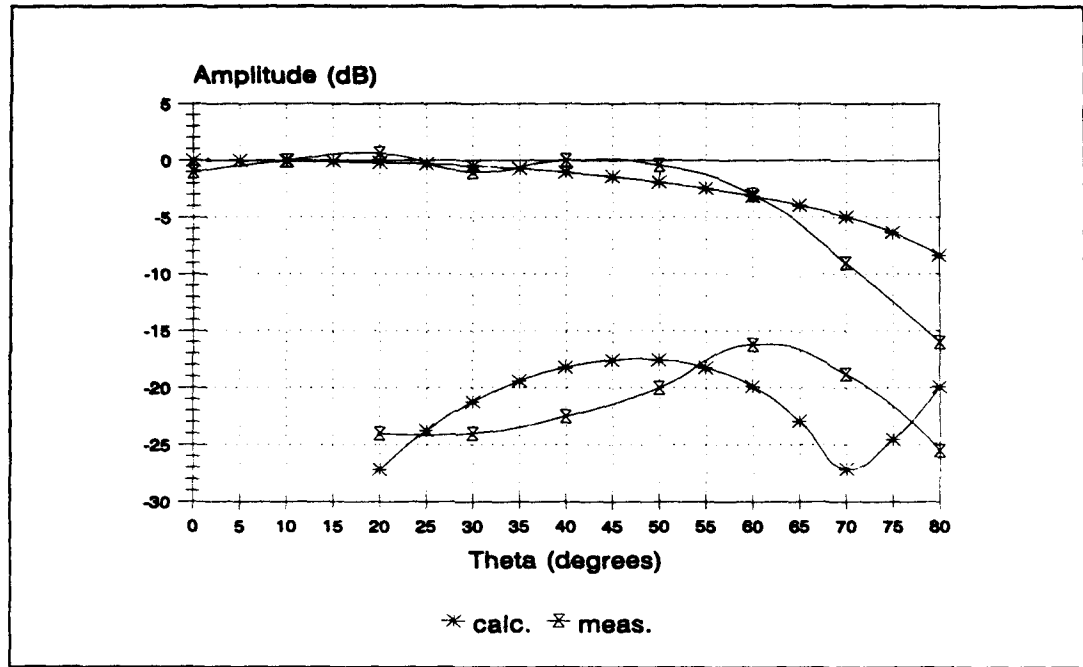


Figure 37: *EXPAR worst case plane active element co and cross polarisation radiation patterns*

Note the fluctuations in the measured patterns due to the finiteness of the array (255 elements), as discussed before.

### 7.2.2 Subarray with matching structure

For a 8x1 subarray with dimensions as stated in paragraph 6.2, the worst case return loss over the scanvolume as function of frequency is calculated, following the strategy explained in paragraph 7.2. The results for the two orthogonal modes are shown in figure 38:

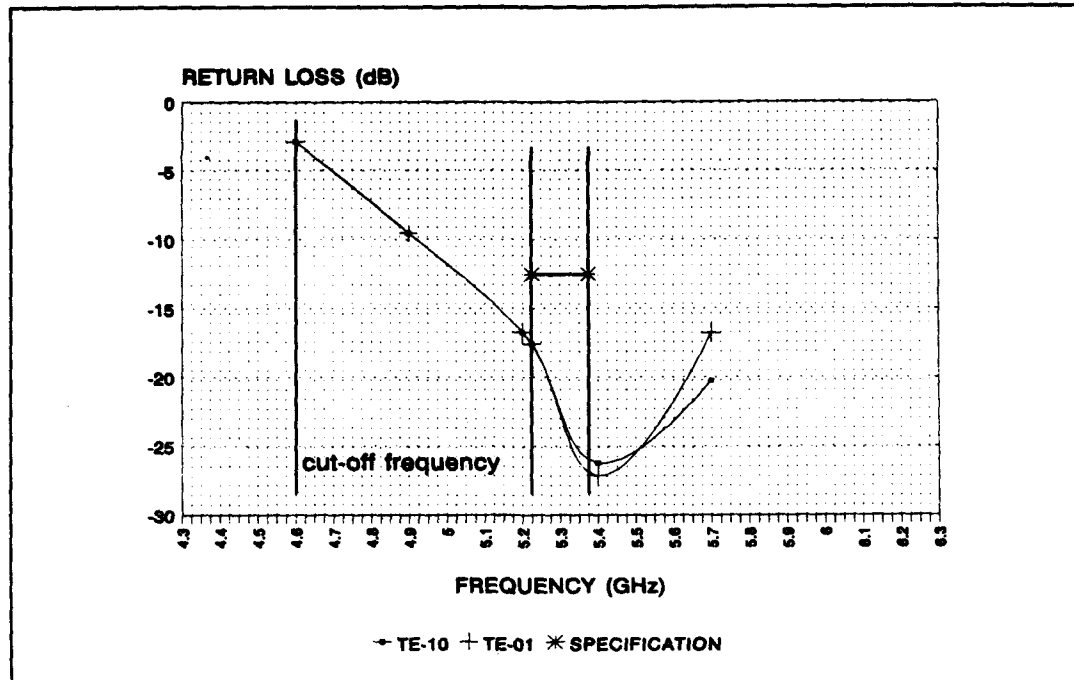


Figure 38: Subarray worst case return loss over scan volume vs frequency; rectangular grid with matching structure

Due to the very low values of the coupling coefficients for the not excited mode, it is not possible to calculate the subarray polarisation isolation in the same way as outlined in paragraph 7.2. Because of the agreement between worst case return loss for the subarray (above figure) and worst case return loss for the element in an infinite array environment (see paragraph 6.2, figure 19), it is allowed to conclude that the polarisation isolation will be comparable to that of the element in an infinite array environment (see paragraph 6.2, figure 20).

For the same reason, it is allowed to construct subarray radiation patterns based on the radiation patterns of an element in an infinite array environment. Figure 39 shows the element patterns and figure 40 shows the subarray radiation patterns based on these element patterns.

The aperture efficiency can be approximated in first order approximation by [30]:

$$\begin{aligned}
 \text{Aperture efficiency} &= \frac{\text{Embedded subarray gain at input port}}{\frac{4\pi \cdot \text{Subarray aperture}}{\lambda^2}} \\
 &\approx \frac{\frac{4\pi}{\lambda^2} \cdot 8 \cdot S \cdot T \cdot \cos(\vartheta_0) \cdot (1 - |\Gamma(\vartheta_0, \varphi_0)|_{sub}^2)}{\frac{4\pi \cdot 8 \cdot S \cdot T}{\lambda^2}} \Big|_{\vartheta_0 = \varphi_0 = 0} \quad (7.2.14) \\
 &= 1 - |\Gamma(0, 0)|_{sub}^2
 \end{aligned}$$

with S and T the element spacings in x and y directions, respectively.

Ohmic losses in the subarray feeding network are not taken into account in the above equation.

The aperture efficiency is shown in figure 41. The bandwidth (operational with margins) is indicated with vertical lines.

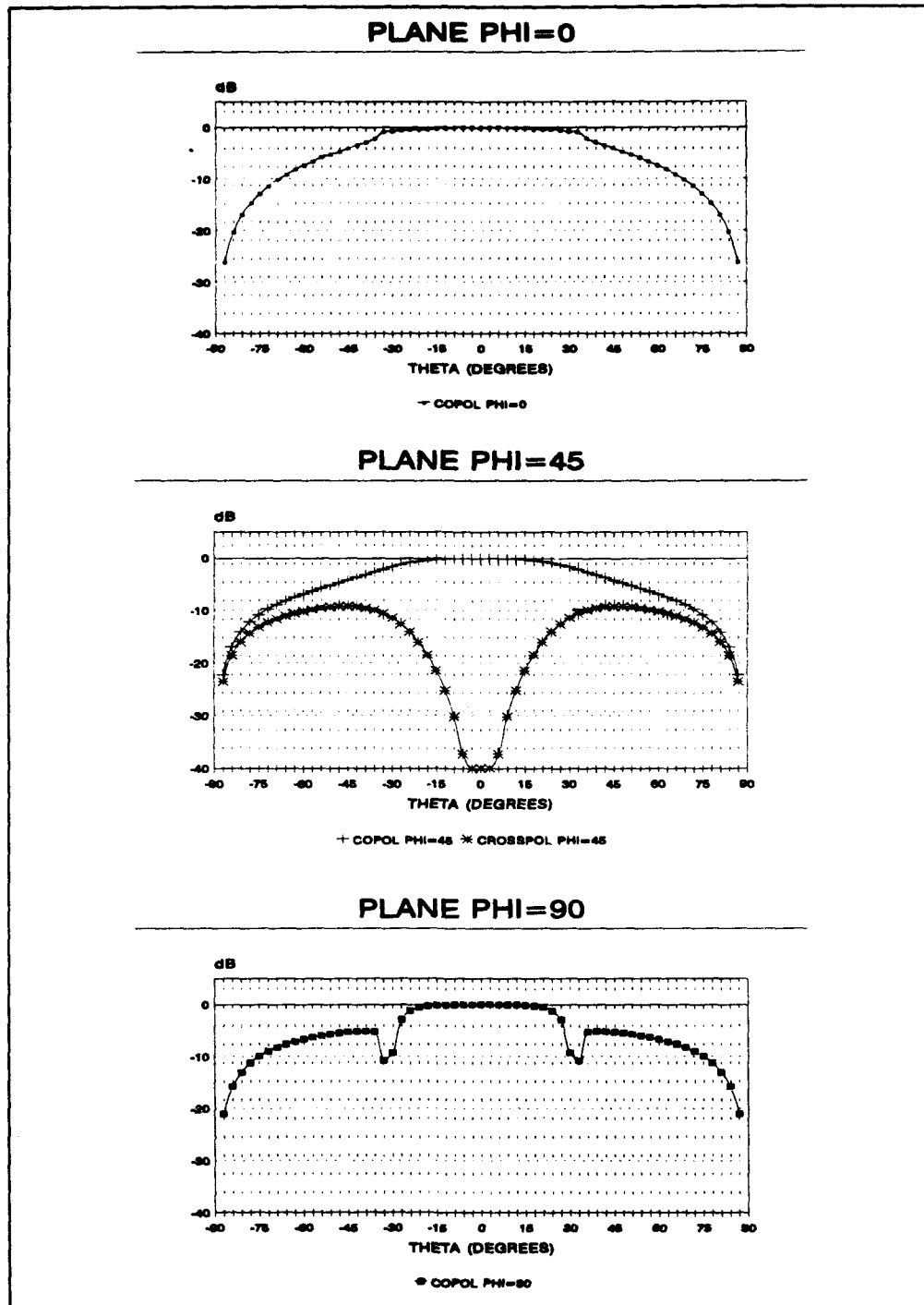


Figure 39: *Element radiation patterns in infinite array environment;  $f = 5.3\text{GHz}$ , rectangular grid with matching structure,  $TE_{10}$ -mode polarisation*

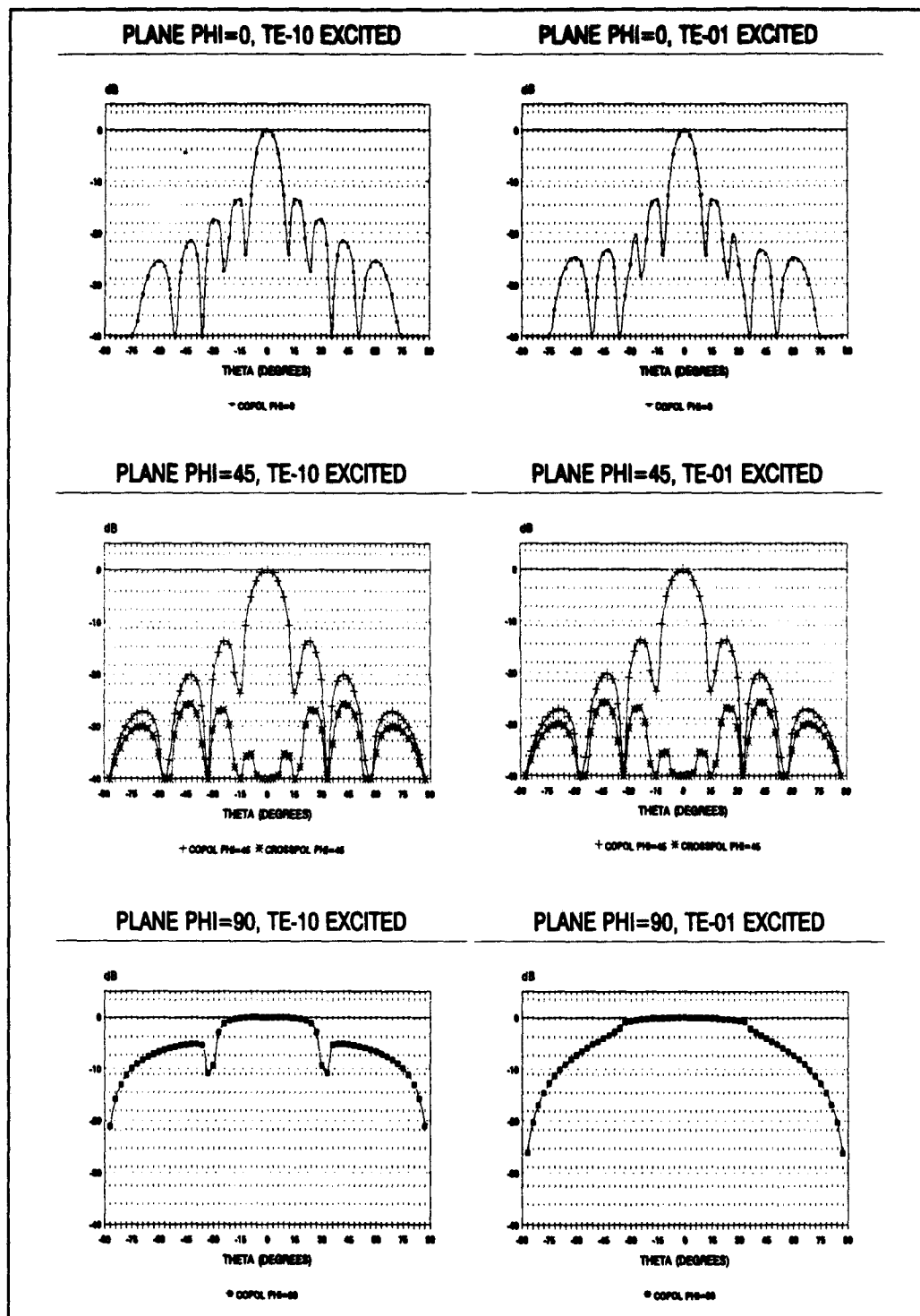


Figure 40: Radiation patterns subarray in array environment; rectangular grid with matching structure,  $f = 5.3\text{GHz}$



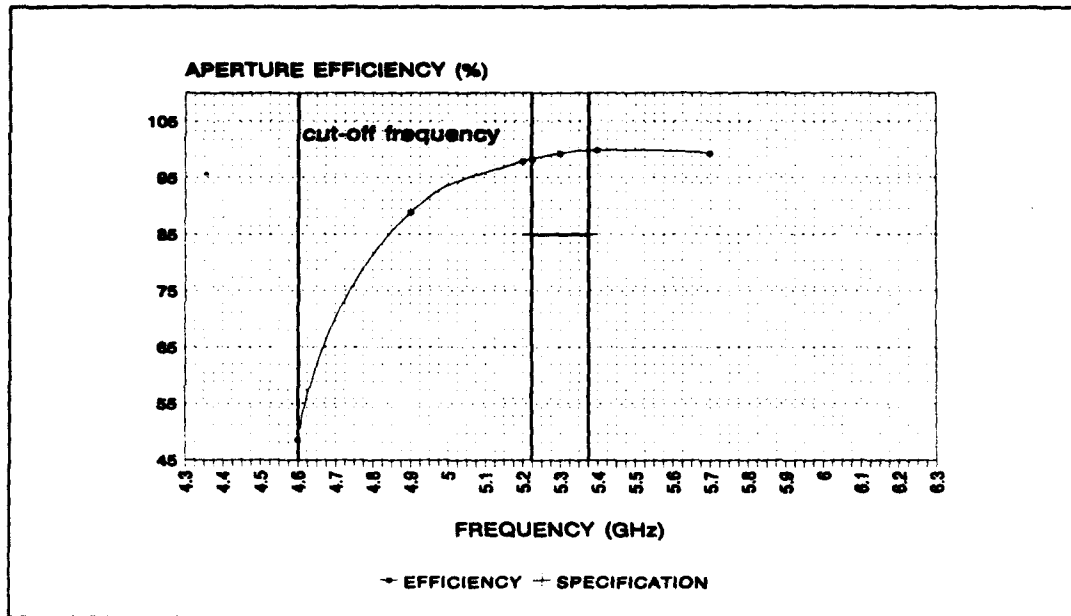


Figure 41: Aperture efficiency subarray; rectangular grid with matching structure, ideal lossless feeding network

### 7.2.3 Subarray without matching structure

For a  $8 \times 1$  subarray with dimensions as stated in paragraph 6.3, the worst case return loss over the scanvolume as function of frequency is calculated, following the strategy explained in paragraph 7.2. The results for the two orthogonal modes are shown in figure 42:

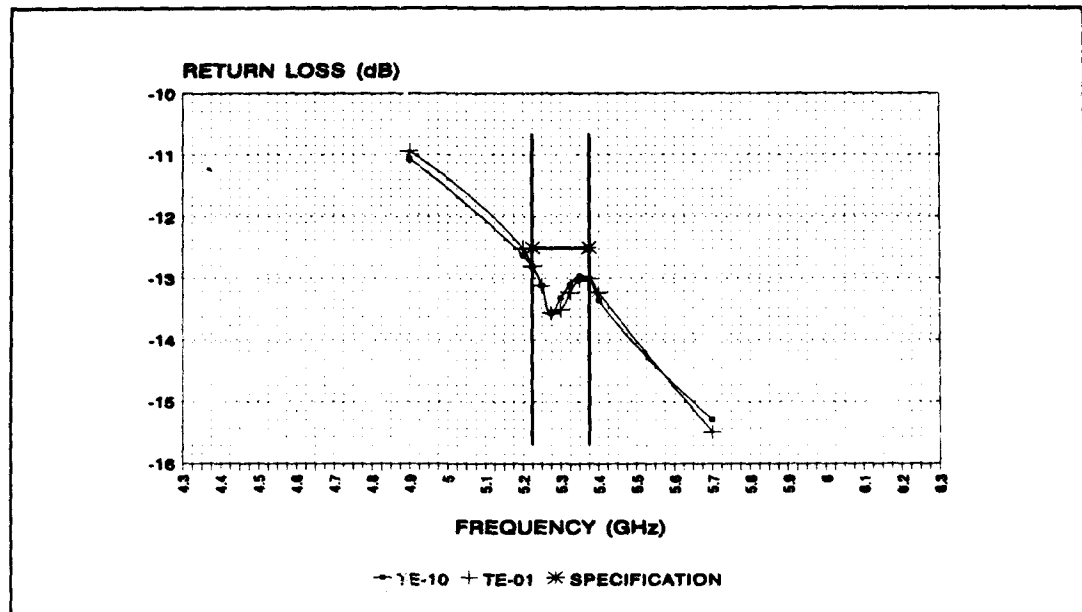


Figure 42: Subarray worst case return loss over scan volume vs frequency; rectangular grid without matching structure

For this configuration, it also was impossible to calculate the polarisation isolation, following the rules of paragraph 7.2, due to the very low values of the coupling coefficients for the not excited mode.

Because of the agreement between worst case return loss for the subarray (above figure) and worst case return loss for the element in an infinite array environment (see paragraph 6.3, figure 22), it is allowed to conclude that the polarisation isolation will be comparable to that of the element in an infinite array environment (see paragraph 6.3, figure 23).

For the same reason, it is allowed to construct subarray radiation patterns based on the radiation patterns of an element in an infinite array environment. Figure 43 shows the element patterns and figure 44 shows the subarray radiation patterns based on these element patterns.

The subarray aperture efficiency is shown in figure 45.

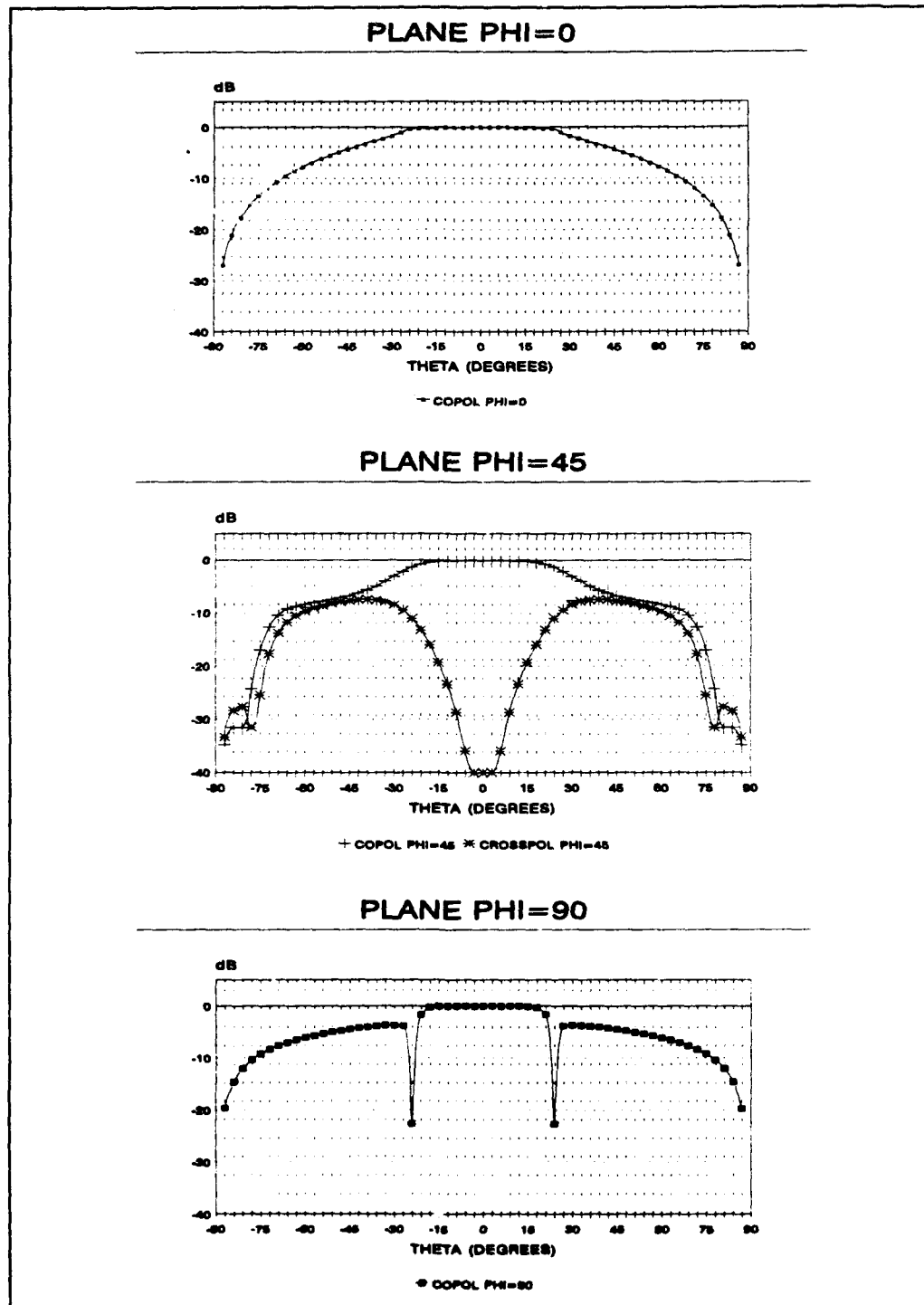


Figure 43: Element radiation patterns in infinite array environment;  $f = 5.3\text{GHz}$ , rectangular grid without matching structure,  $TE_{10}$ -mode polarisation

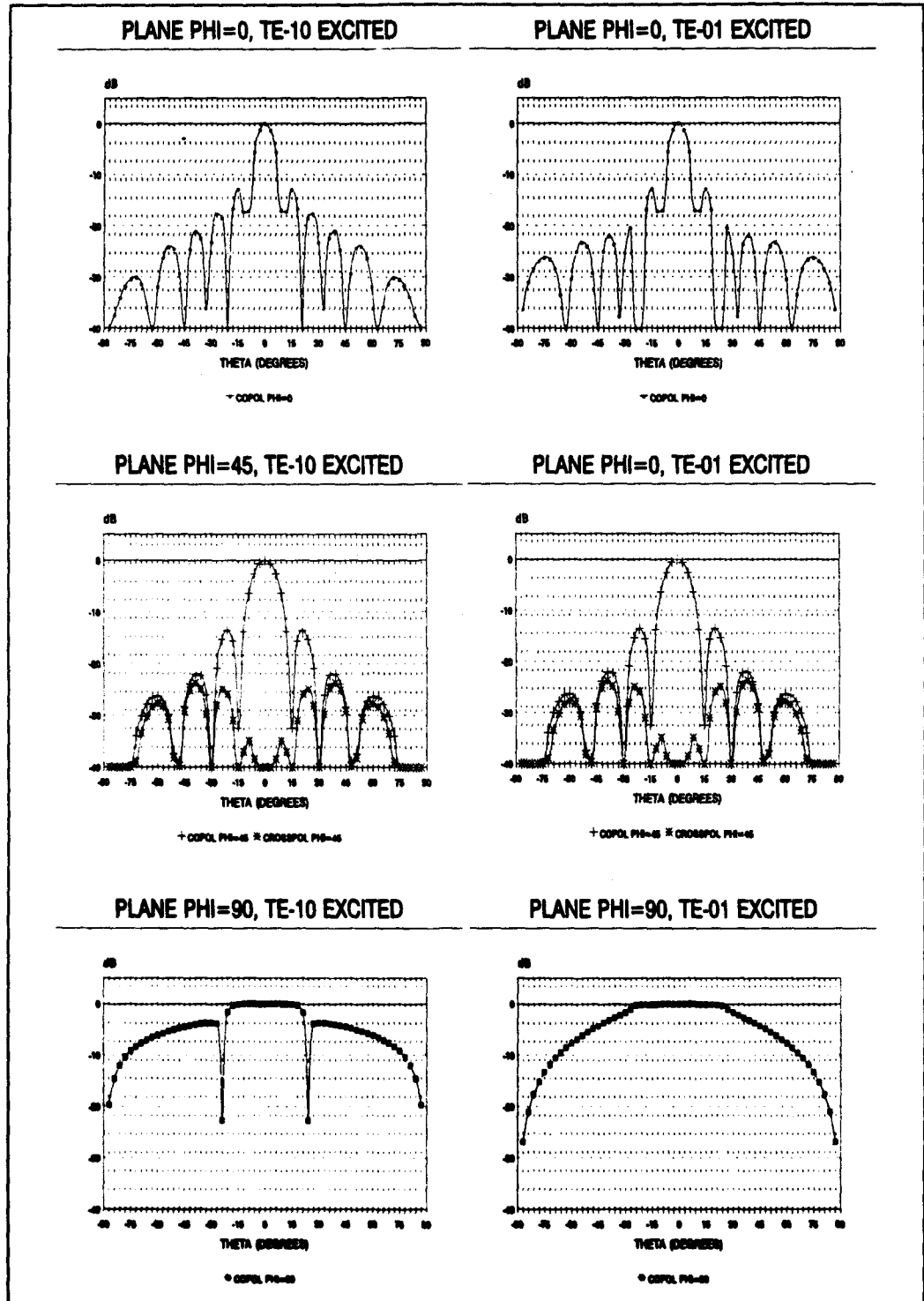


Figure 44: Radiation patterns subarray in array environment; rectangular grid without matching structure,  $f = 5.3\text{GHz}$

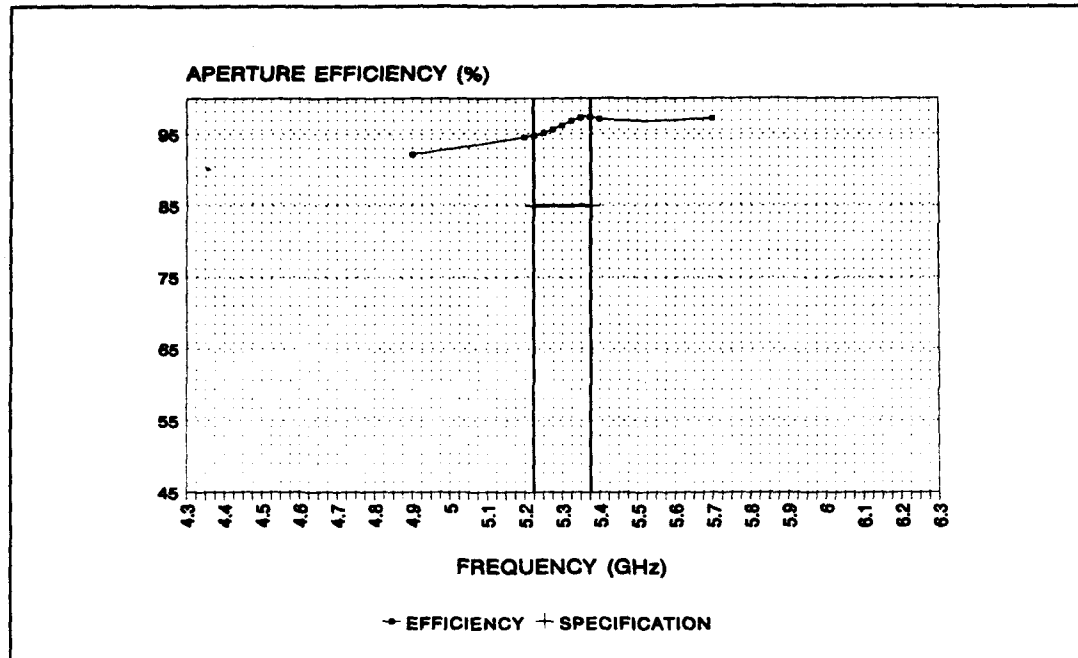


Figure 45: Aperture efficiency subarray; rectangular grid without matching structure, ideal lossless feeding network

### 7.3 Choice subarray design

In an earlier stage we already rejected designs with a triangular lattice. At this stage we have to make a choice between the design of paragraph 6.2 (7.2.2) and the design of paragraph 6.3 (7.2.3).

Although the characteristics of the design presented in paragraph 6.2 (7.2.2) are better, we choose for the design of paragraph 6.3 (7.2.3).

The reason for this choice is that this design is much easier to construct (no irises and dielectric matching sheet). Furthermore, we do not have to deal with tolerance problems in applying the dielectric sheet and the characteristics of this design still meet the specifications.

## 8 WAVEGUIDE EXCITER & SUBARRAY FEEDING NETWORK

In the foregoing chapters, we assumed that the  $TE_{10}$ -mode and/or the  $TE_{01}$ -mode were excited in the waveguide without specifying how this was accomplished. In calculating the subarray reflection coefficient we assumed perfectly excited waveguide modes and an ideal 1 to 8 combining network.

This chapter deals with the practical implementation of exciting the waveguide modes and combining the elements in the subarray.

The waveguide exciter, to be discussed in the next paragraph, is ment for breadboard purposes only. The exciter is not optimal for space qualification, but a first step in the development of a completely space qualified design. The space qualified design will be generated under workpackage 2000 [1]. Since workpackage 1000 only asks a preliminary space borne SAR antenna design, the exciter to be discussed will do for the moment.

### 8.1 Preliminary waveguide exciter design

In order to make an exciter as flat as possible - radiator thickness is an important design parameter - we use a microstrip patch structure to excite the  $TE_{10}$ -mode and  $TE_{01}$ -mode.

This may seem odd at first sight, since one of the antenna options is a microstrip patch antenna [1], but - and this can not be emphasised enough - *the patch structure in itself is not used as an antenna element.*

We do not have to deal with microstrip patch mutual coupling, ground waves and other effects of microstrip patch array antennas. The patch is used as exciter of the waveguides, and the behaviour of waveguide antennas can be simulated with great accuracy, as is thoroughly demonstrated in the foregoing chapters.

The idea of using a microstrip patch antenna is not new; results have recently been published [31].

Because of the involvement of TNO-FEL in the design and realisation of a C-band airborne SAR antenna (PHARUS: PHased ARray Universal SAR) [32], single layered dual polarised probe-fed patch elements were available and these were used as basis for the waveguide exciter. The exciter is shown in figure 46. For the sake of clarity, quarter lambda airstripline transformers in the coaxial connectors, are not drawn.

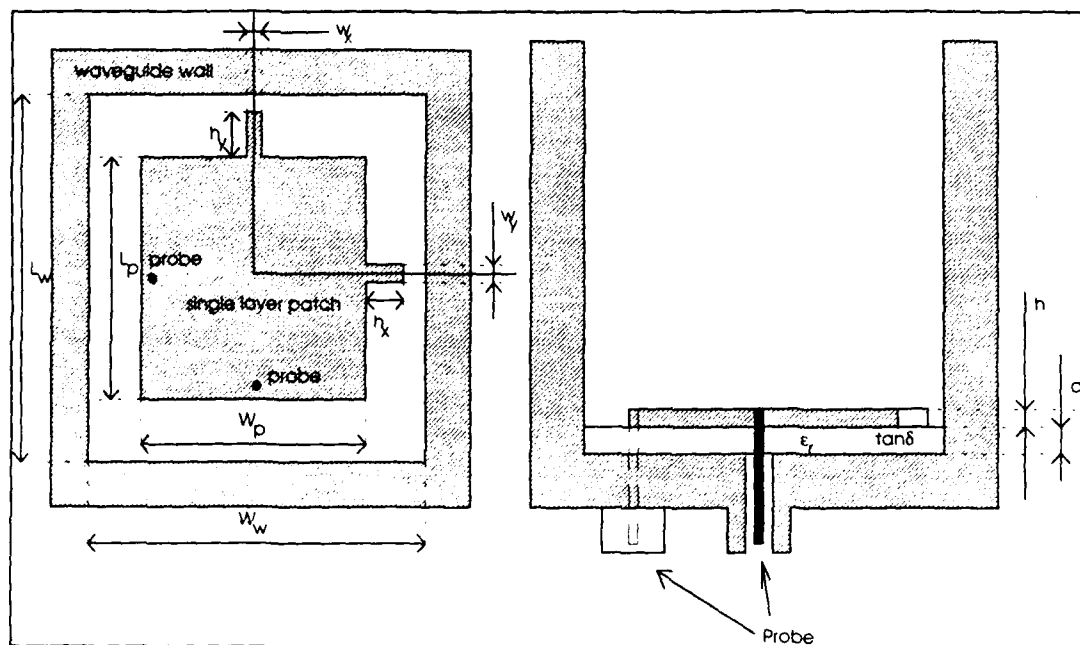


Figure 46: Top and side view waveguide exciter

A demonstrator has been realised. The dimensions, with reference to the above figure, are stated in table 8. Results of a electromagnetic 3D simulator as well as measurement results are shown in figure 47a and 47b. Measured and simulated are the behaviour of the exciter placed in the waveguide

Table 8: Dimensions waveguide exciter demonstrator

$W_w$ (mm)	34.38	$h_x$ (mm)	2.50
$L_w$ (mm)	34.38	$h_y$ (mm)	2.50
$W_p$ (mm)	17.50	$h$ (mm)	0.035
$L_p$ (mm)	17.50	$d$ (mm)	1.57
$w_x$ (mm)	0.8	$\epsilon_r$	2.33
$w_y$ (mm)	0.8	$\tan\delta$	0.0012

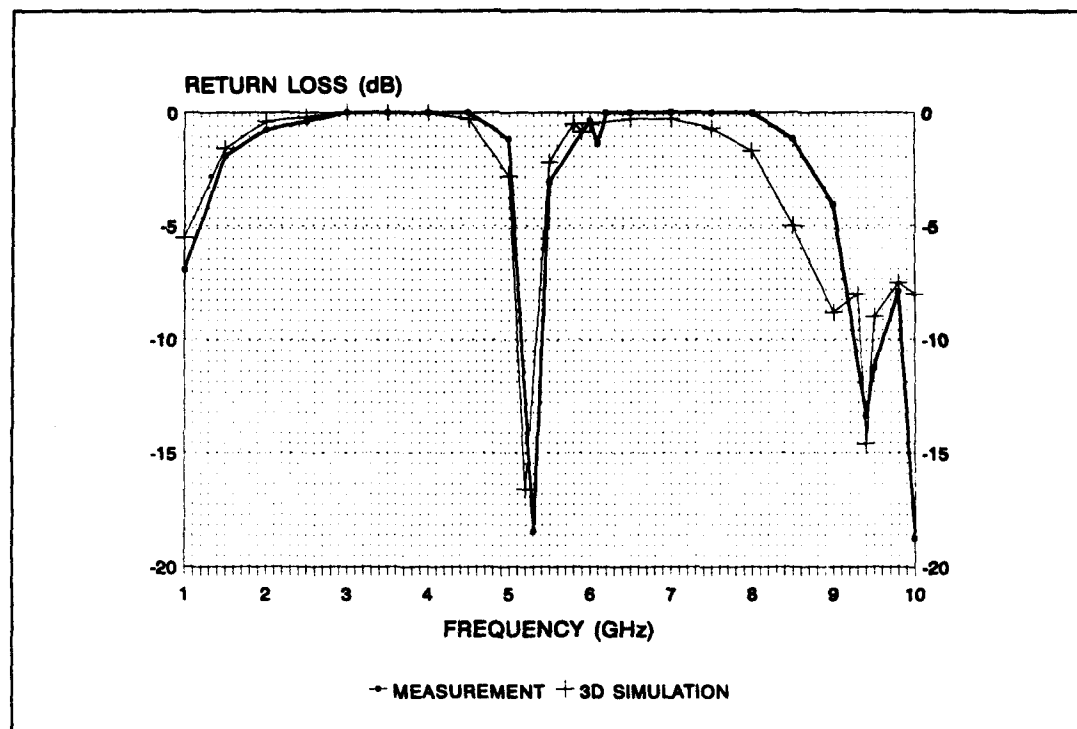


Figure 47a: Measured and simulated waveguide exciter return loss



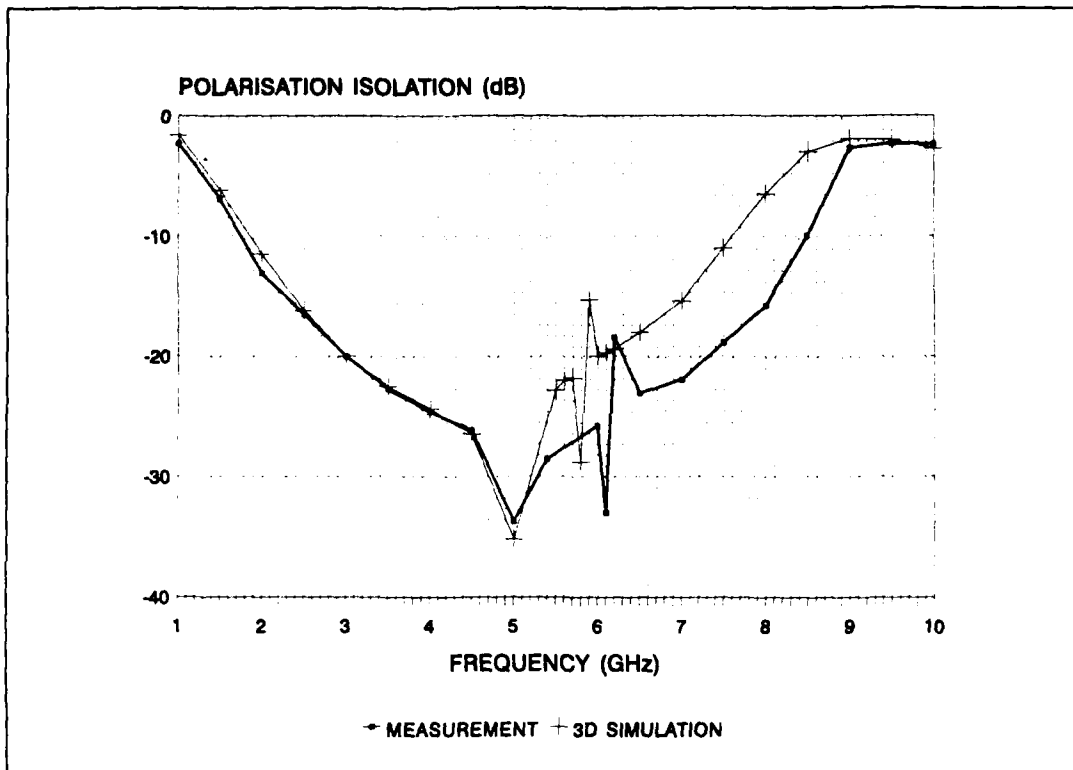


Figure 47b: Measured and simulated waveguide exciter polarisation isolation

The mismatch between simulations and measurements in the second half of the frequency band considered is most probably due to differences in the stub dimensions (see figure 25) in simulations and measurements. During the measurements, the stubs were lost and replaced with wires of length equal to the stublengths as shown in figure 46.

Nevertheless, the figures clearly show that we are able to simulate the behaviour of the exciter placed in the waveguide.

It is interesting to note that the behaviour measured at the right side of the resonance frequency also shows up in the simulations. This behaviour must be due to a mismatch of the quarter lambda transformers mentioned before.

Furthermore, the exciter satisfies the specifications within the 150 MHz frequency band.

## 8.2 Space qualified waveguide exciter design

The foregoing paragraph has shown that we have the tools necessary to design a microstrip patch waveguide exciter.

At the moment, running ahead of workpackage 2000, we are working on a aperture coupled microstrip patch waveguide exciter that has no soldering connections and will therefore be space qualified.

### 8.3 Subarray feeding network design

In order to demonstrate our ability to design a subarray feeding network, running ahead of workpackage 2000 and the space qualified exciter design, a feeding network in microstrip is designed. Material parameters are given in table 9:

Table 9: Subarray feeding network material parameters

PARAMETER	VALUE
$\epsilon_r$	2.33
$\tan(\delta)$	0.0012
substrate height	0.4 mm
metal thickness	0.035 mm
metal rho	1.25
metal roughness	0

Figures 48a, b and c show the patches in the waveguides, the feeding network and the combination of these, respectively:

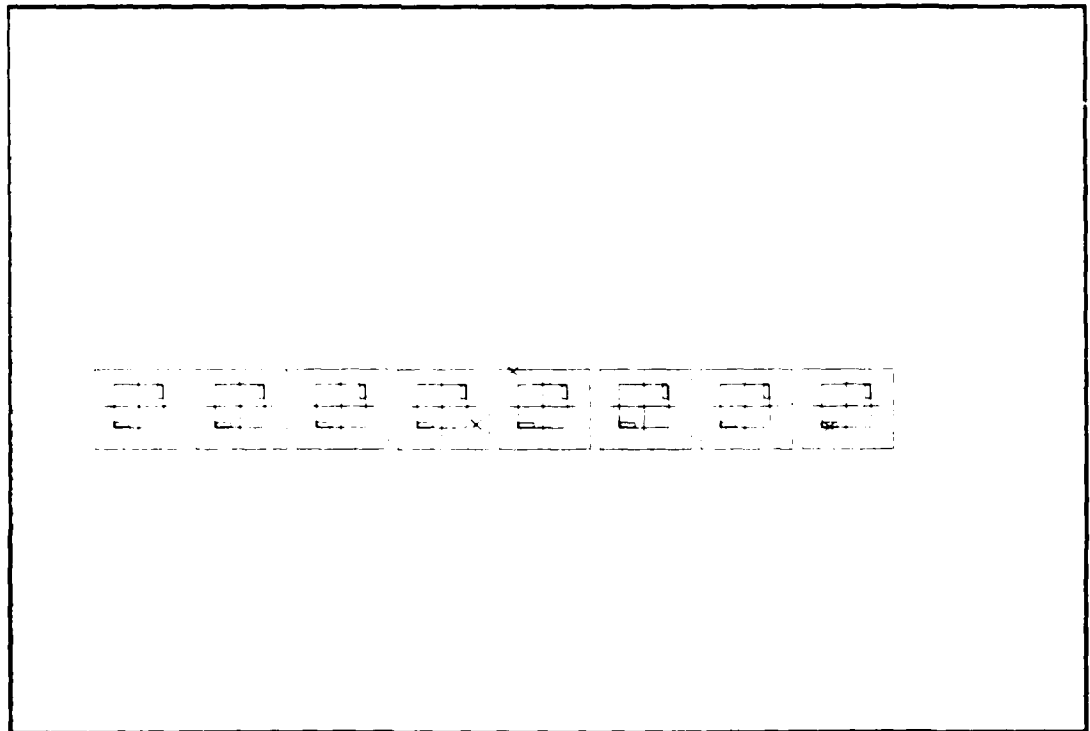


Figure 48a: Subarray: exciters within waveguides

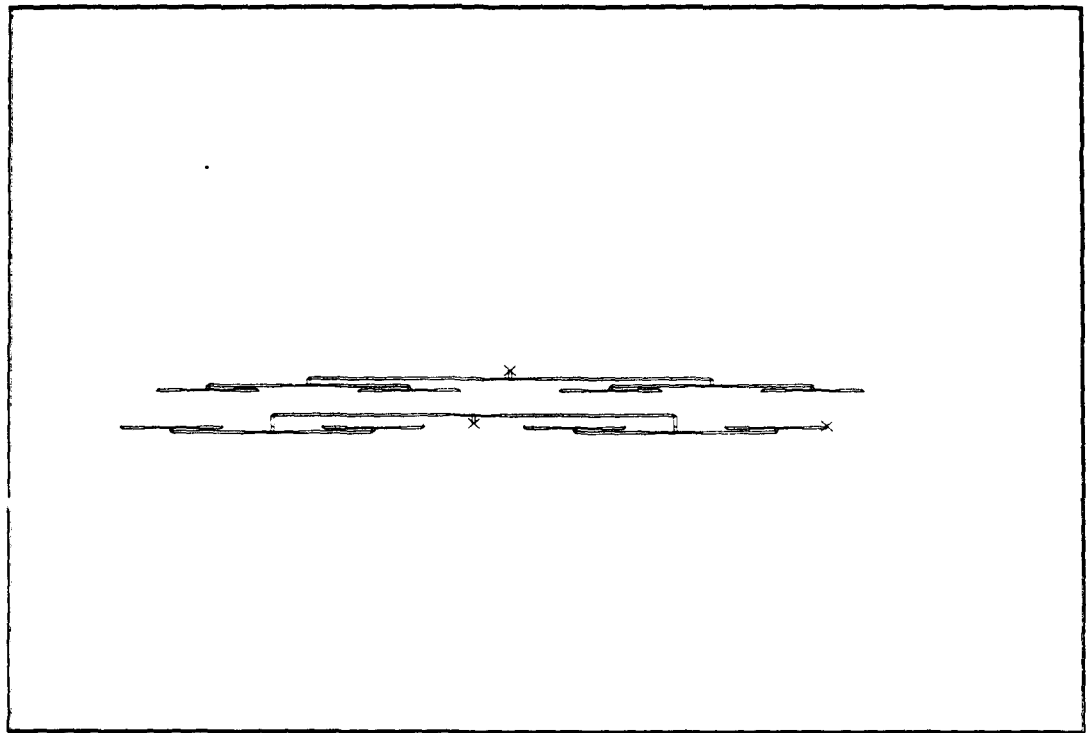
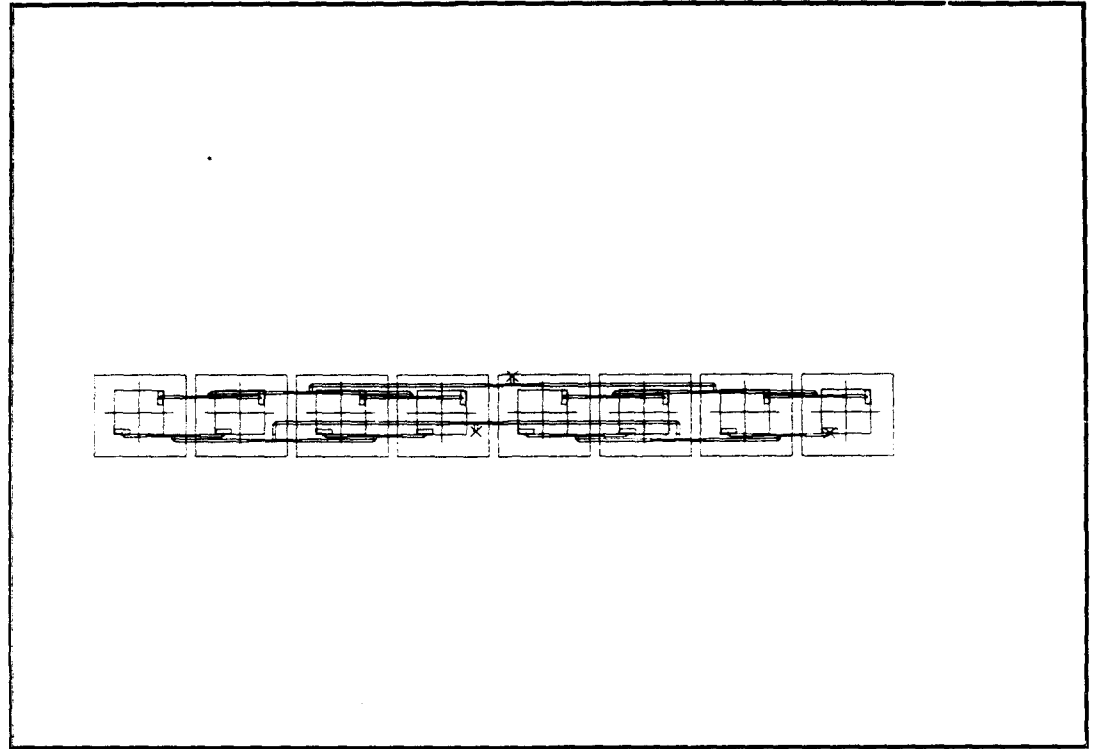


Figure 48b: Subarray: microstrip feeding network



*Figure 48c: Subarray: exciters within waveguides and microstrip feeding network*

Note that the feeding network completely fits in the subarray.

The behaviour of this feeding network has been simulated. The results are shown in figures 49, 51 and 52.

These figures show that all specifications are met, except for the loss goal of 1dB/m. With a subarray length of 31.68 cm (design of paragraph 6.2), figure 49 indicates that the loss will be 1.19dB/m. Since this feeding network is a preliminary design, we are convinced that we can design a feeding network that even meets this rather tight specification. This can be accomplished by using a thicker substrate. A thickness of 1 mm seems to be possible without getting problems like surface waves.

Shown is that we have the tools and experience to design a subarray feeding network.

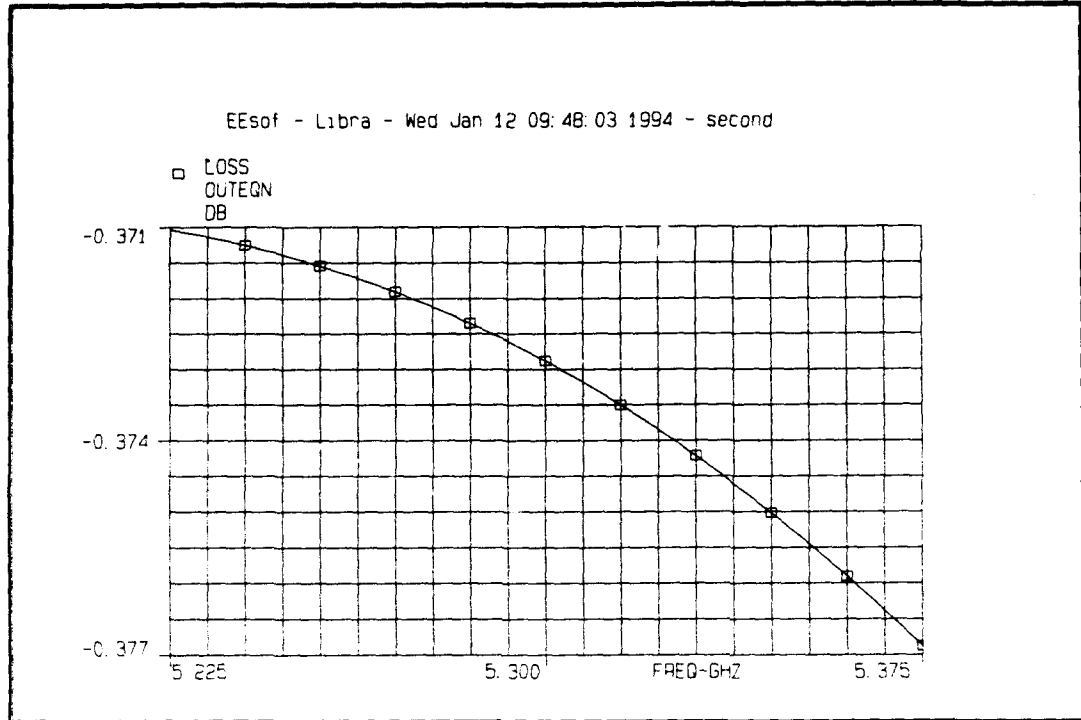


Figure 49: Microstrip subarray feeding network loss

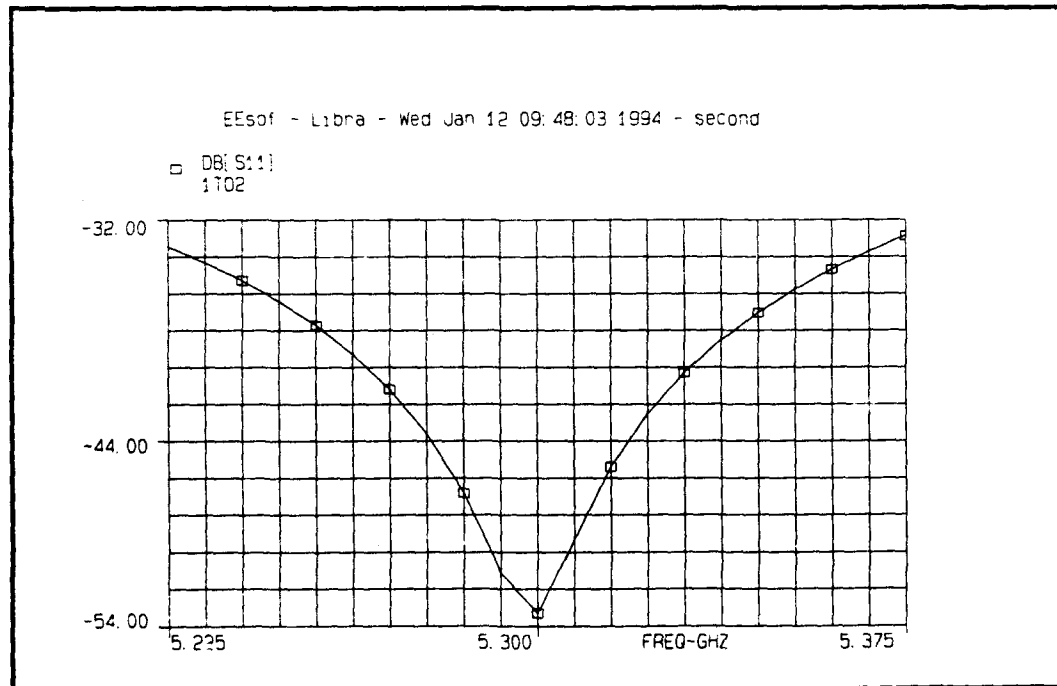


Figure 50: Microstrip subarray feeding network return loss

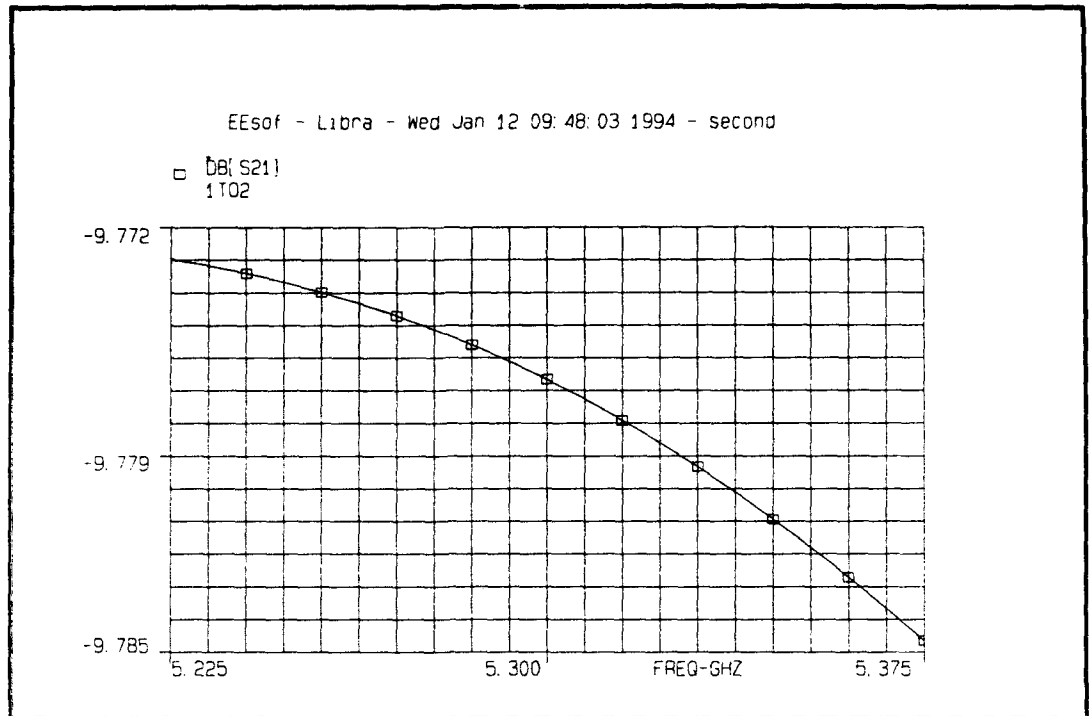


Figure 51: Transmission coefficient 1:8 subarray power divider



## 9 RADIATING PLANE THICKNESS

In order to estimate the depth of the waveguides, we have to look at the non-propagating waveguide modes. These modes are introduced at the exciter side of the waveguide and at the aperture (iris) side of the waveguide. The length of the waveguide must be chosen such, that these non propagating higher order modes - the waveguides can only propagate the TE<sub>10</sub>-mode and the TE<sub>01</sub>-mode - are sufficiently attenuated, so that no higher order mode interaction between exciter side and aperture side can occur.

### 9.1 Attenuation constant

Since waves are propagating or decaying with a factor  $\exp(-j\gamma^{(1)}_{mn}z)$ ,  $z$  being the distance in the waveguide direction, the attenuation constant for non propagating modes is given by

$$\alpha = -\text{Real}(-j\gamma^{(1)}_{mn}).$$

The attenuation constants for the waveguide modes of the design presented in paragraph 6.2 at the centre frequency are stated in table 10 and figure 52. These attenuation constants change very little over the frequency band of 150 MHz.

Table 10: Attenuation constants higher order modes at 5.3 GHz:

WAVEGUIDE MODE	$\alpha$ (m <sup>-1</sup> )	$\alpha$ (dB/m)
TE-02	155.12	43.81
TE-11	76.62	37.69
TE-12	182.09	45.21
TE-20	155.12	43.81
TE-21	182.09	45.21
TE-22	245.86	47.81
TE-30	263.71	48.42
TE-31	280.43	48.96
TE-32	325.46	50.25
TE-40	364.99	51.25
TE-41	377.24	51.53
TE-42	411.82	52.29
TE-50	463.77	53.33
TE-51	473.47	53.51
TE-52	501.46	54.00
TM-11	76.62	37.69
TM-12	182.09	45.21
TM-21	182.09	45.21
TM-22	245.86	47.81
TM-31	280.43	48.96
TM-32	325.46	50.25
TM-41	377.24	51.53
TM-42	411.82	52.29
TM-51	473.47	53.51
TM-52	501.46	54.00



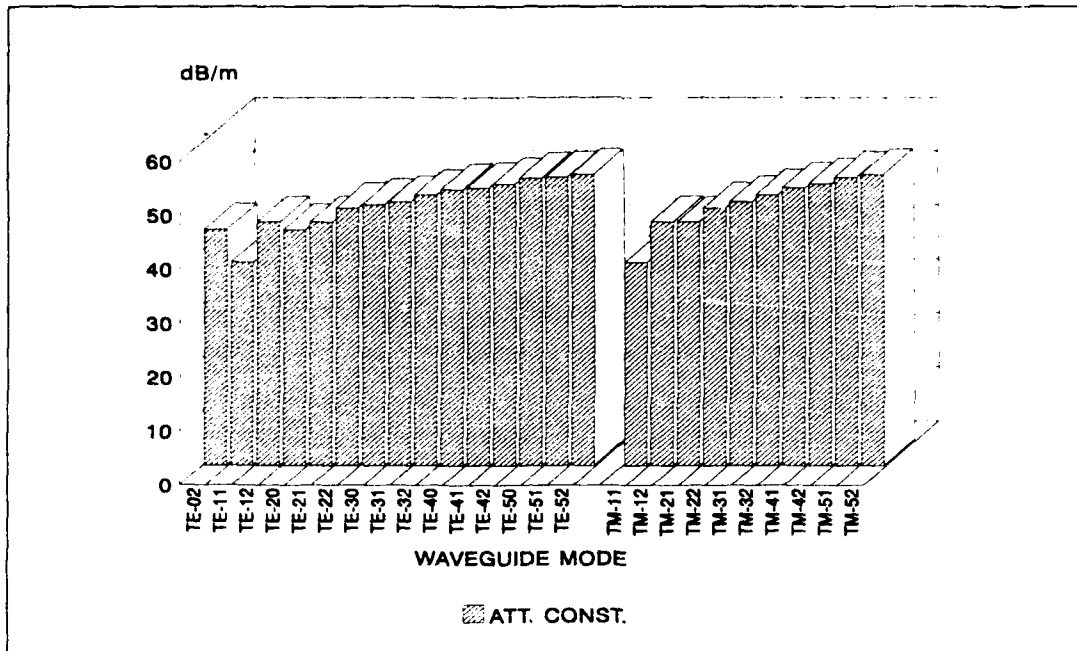


Figure 52: Higher order mode attenuation constants at 5.3GHz

Table 6 and figure 52 show that the  $TE_{11}$ -mode and  $TM_{11}$ -mode are the modes that will determine the waveguide height.

## 9.2 Attenuation levels

Attenuation levels as function of the waveguide height ( $\exp(\alpha z)$ ) are given in table 11 and figure 53.

Table 11: Attenuation levels (dB) as function of waveguide thickness

MODE	z=1cm	z = 2cm	z = 3cm	z = 4cm
TE-02	13.48	26.95	40.43	53.90
TE-11	6.66	13.31	19.97	26.62
TE-12	15.82	31.64	47.45	63.26
TE-20	13.47	26.94	40.42	53.89
TE-21	15.82	31.63	47.45	63.27
TE-22	21.35	42.71	64.06	85.42
TE-30	22.91	45.81	68.72	91.62
TE-31	24.36	48.72	73.08	97.43
TE-32	28.27	56.54	84.81	113.08
TE-40	31.70	66.28	95.11	126.81
TE-41	32.76	65.53	98.30	131.06
TE-42	35.77	71.54	107.31	143.08
TE-50	40.31	80.57	120.85	161.13
TE-51	41.12	82.25	123.37	164.50
TE-52	43.55	87.11	130.66	174.22
TM-11	6.66	13.31	19.97	26.62
TM-12	15.82	31.64	47.45	63.26
TM-21	15.82	31.64	47.45	63.26
TM-22	21.35	42.71	64.06	85.42
TM-31	24.36	48.72	73.08	97.43
TM32	28.27	56.54	84.81	113.08
TM-41	32.76	65.53	98.30	131.06
TM-42	35.77	71.54	107.31	143.08
TM-51	41.12	82.25	123.37	164.50
TM-52	43.55	87.11	130.66	174.22

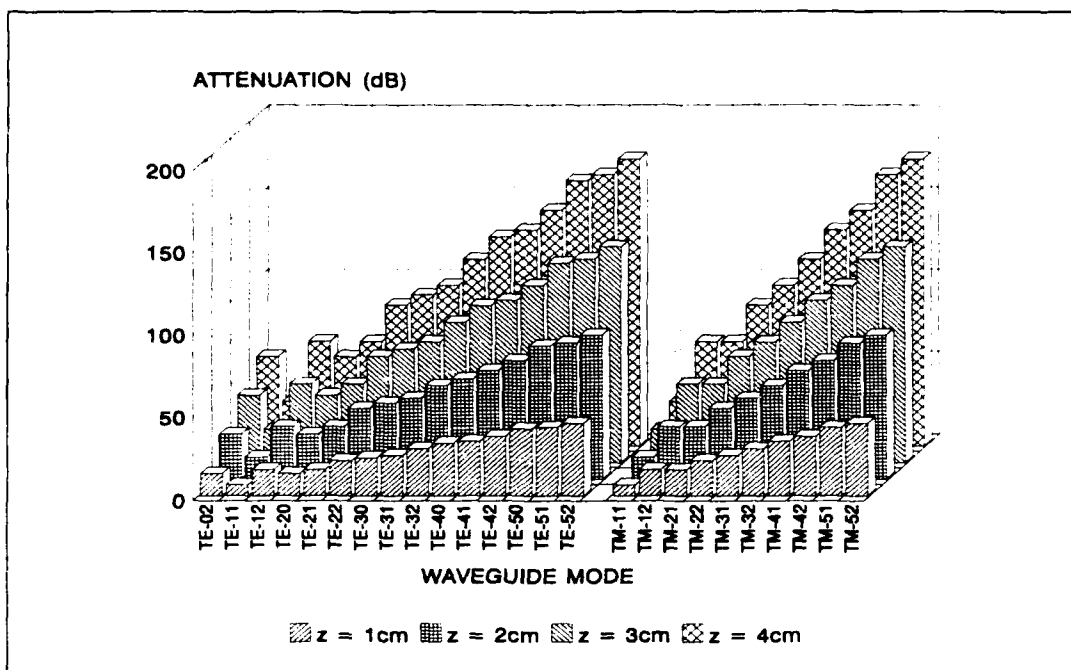


Figure 53: Attenuation levels vs radiator thickness at  $f = 5.3\text{GHz}$

### 9.3 Depth waveguide radiators

Taking into account that the higher order mode amplitudes will be small compared to the excited  $\text{TE}_{10}$ -mode and  $\text{TE}_{01}$ -mode amplitude coefficients and that we have neglected attenuation arising from the finite conductivity of the waveguide walls, looking at the  $\text{TE}_{11}$ -mode and  $\text{TM}_{11}$ -mode, we choose a radiator thickness of 2.5 cm, leaving 0.5 cm for the subarray feeding network.<sup>1</sup>

Because in all our antenna designs (see chapter 6 and 7) the waveguide dimensions are more or less the same, it is permitted to maintain this waveguide depth for all designs.

Since the waveguides will be self-supporting, the support structure, common in printed antenna SAR antennas, is cancelled, see figure 54 [33] and figure 55:

<sup>1</sup>This in agreement with the 3cm for radiator, feed network and support structure settled at the progress meeting held at Dornier GmbH, Friedrichshafen Germany, November 18 1993.

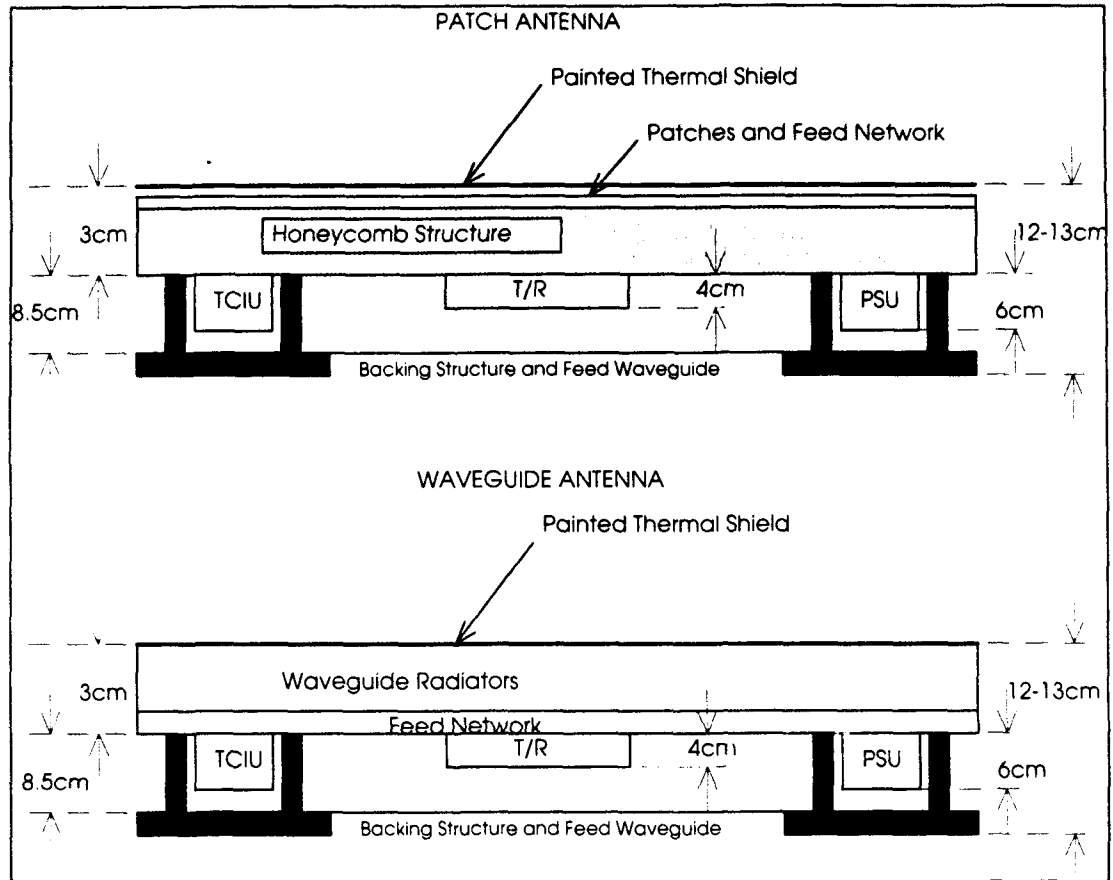


Figure 54: Cross section of a patch antenna tile and waveguide antenna tile

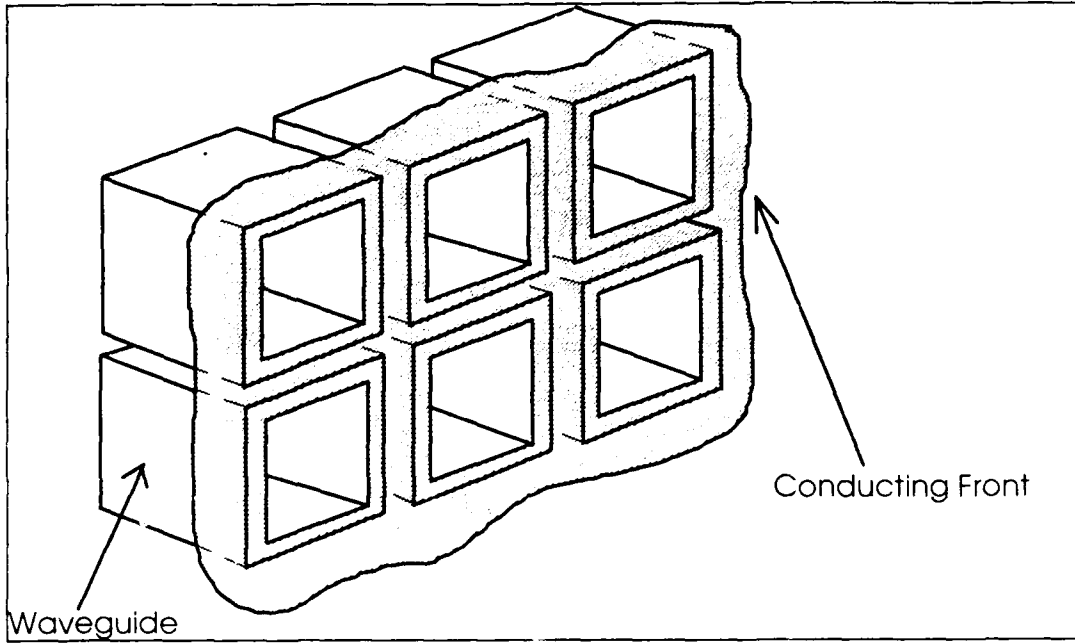


Figure 55: 3D impression part of waveguide antenna

## 10 CONCLUDING REMARKS

In the foregoing it has been shown thoroughly that at TNO-FEL we have all the tools necessary to design a SAR waveguide phased array antenna:

- The antenna can be analysed and synthesised
- Finiteness effects can be taken into account
- The subarray in the array environment can be analysed; it is demonstrated that it is of vital importance to include the array environment in the subarray analysis
- A microstrip patch waveguide exciter can be designed and analysed
- A microstrip subarray feeding network can be designed and analysed

Different waveguide SAR antenna designs are presented which all satisfy the specifications.

All the software tools are available to analyse the complete subarray from feeding network to exciter to waveguides all together.

In the near-future we will perform measurements on a dual polarised (square) waveguide array antenna. This antenna, shown in figure 56, is now under construction.

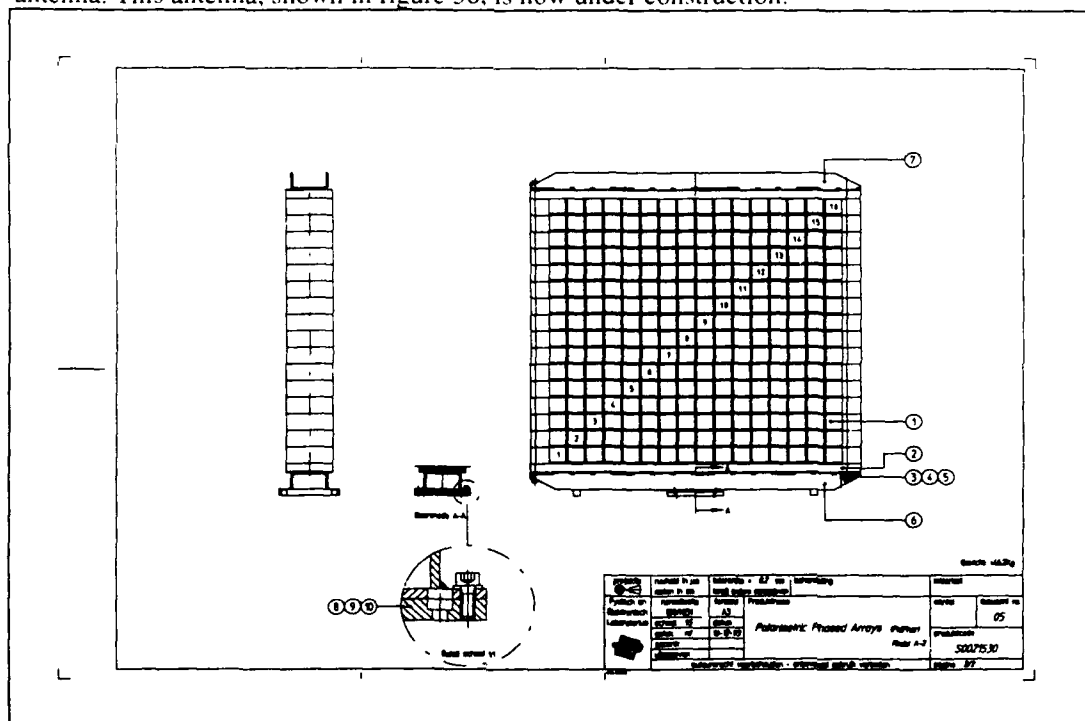


Figure 56: Dual polarised waveguide array test antenna



## 11 ACKNOWLEDGEMENTS

The author wishes to acknowledge ir. A.B. Smolders from Eindhoven University of Technology for supplying coupling coefficients of a planar microstrip patch array antenna and for providing a huge amount of personal computer CPU time for calculating waveguide phased array antenna mutual coupling coefficients.

The author further wishes to acknowledge ir. M.J.M. Geurts for designing the preliminary subarray feeding network and mr. F.A. Nennie for measuring and tuning the waveguide exciter.



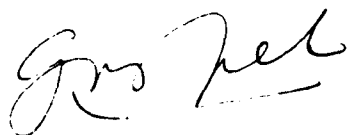


## 12 REFERENCES

- [1] -: '*Study of a Dual Polarised Antenna Element*',  
Dornier proposal No. 16-0-93, January 1993.
- [2] ESA-ESTEC: '*Invitation to Tender AO/I-2641/92/NL/GS Dual Polarisation Antenna Element*',  
ESA/IPC(92)26, Item No. 91.1XE.02, October 15 1992.
- [3] Dornier GmbH: '*Minutes of Meeting Progress Meeting Novemer 18 1993*'.
- [4] A.J. Fenn: '*Element Gain Pattern Prediction for Finite Arrays of V-Dipole Antennas Over Ground Plane*',  
IEEE Transactions on Antennas & Propagation, Vol. 36, No. 11, November 1988,  
pp. 1629-1633.
- [5] L.R. Lewis: '*Practical Phased Array Systems*',  
Microwave Journal Intensive Course, Microwave Journal, pp. 5-1 - 5-18.
- [6] M.J. Povinelli, C.E. Grove: '*Wideband Apertures for Active Planar Multifunction Phased Arrays*',  
Proceedings of the National IEEE Radar Conference, 1984, pp. 125-128.
- [7] M.H. Chen, G.N. Tsandoulas, F.G. Willwerth: '*Modal Characteristics of Quadruple-Ridged Circular and Square Waveguides*',  
IEEE Transactions on Microwave Theory & Techniques, Vol. MTT-22, No. 8,  
August 1974, pp. 801-804.
- [8] S.J. Foti, M.W. Shelley: '*An Experimental Wideband Polarisation Diverse Phased Array*',  
Proceedings of Military Microwaves, 1990, pp. 263-271.
- [9] C.C. Chen: '*Wideband Wide-Angle Impedance Matching and Polarization Characteristics of Circular Waveguide Phased Arrays*',  
IEEE Transactions on Antennas & Propagation, Vol. AP-22, No. 3, May 1974,  
pp. 414-418.
- [10] G.N. Tsandoulas, G.H. Knittel: '*The Analysis and Design of Dual-Polarization Square Waveguide Phased Arrays*',  
IEEE Transactions on Antennas & Propagation, Vol. AP-21, No. 6, November 1973,  
pp. 796-808.
- [11] W.P.M.N. Keizer, A.P. de Hek, A.B. Smolders: '*Theoretical and experimental Performance of a Wideband Wide-Scan Angle Rectangular waveguide Phased Array*',  
IEEE Antennas & Propagation Society Symposium Digest, 1991, Ontario, Canada,  
Vol. 3, pp. 1724-1727.

- [12] H.J. van Schaik: '*Theory and Performance of a Space-Fed, Planar, Phased-Array Antenna With 849 Iris-Loaded Rectangular-Waveguide elements and External Matching Sheet*',  
Ph.D. Thesis, Delft University of Technology, The Netherlands, June 1979.
- [13] S.W. Lee, W.R. Jones: '*On the Suppression of Radiation Nulls and Broadband Impedance Matching of Rectangular Waveguide Arrays*',  
IEEE Transactions on Antennas & Propagation, Vol. Ap-18, pp. 41-51, January 1971.
- [14] A.B. Smolders: '*Mutuele Koppeling Metingen Aan Een Testarray Bestaande Uit 233 Golfpijstralers*',  
TNO Physics & Electronics Laboratory, Report No. FEL-90-B362, January 1991  
(in Dutch)
- [15] H.J. Visser: '*A FORTRAN Code For Analyzing Polarimetric Phased Array Antennas, Phase One: Basic Theory*'  
TNO Physics & Electronics Laboratory, Report No. FEL-92-A336, May 1993.
- [16] N. Amitay, V. Galindo, C.P. Wu: '*Theory and Analysis of Phased Array Antennas*',  
Wiley-Interscience, 1972.
- [17] R.C. Hansen: '*Evaluation of the Large Array Method*',  
IEE Proceedings, Vol.137, Pt.H., No.2, April 1990, pp. 94-98.
- [18] H.J. Visser: '*Simulation of Large Finite Phased Array Antennas Using Infinite Array Data*',  
TNO Physics & Electronics Laboratory, in preparation.
- [19] J.A. Nelder and R. Mead: '*Computer Journal*',  
Vol. 7, p.308.
- [20] W.H. Melder, B.P. Flannery, S.A. Teukolsky, W.T. Vetterling: '*Numerical Recipes, The Art of Scientific Computing*',  
Cambridge University Press, Second Edition, 1990.
- [21] H. Szu And R. Hartley: '*Fast Simulated Annealing*',  
Physics Letters A, Volume 122, Number 3,4, June 8 1987, pp.157-162.
- [22] A. Silverman and J. Adler: '*Animated Simulated Annealing*',  
Computers in Physics, Vol.6, No.3, May/June 1992, pp.277-281.
- [23] S. Kirkpatrick, C.D. Gelatt Jr., M.P. Vecchi: '*Optimization by Simulated Annealing*',  
Science, Volume 220, No. 4598, May 13 1983, pp.671-680.
- [24] G.L. Bilbro, W.E. Snyder, S.J. Garnier, J.W. Gault: '*Mean Field Annealing: A Formalism for Constructing GNC-Like Algorithms*',  
IEEE Transactions on Neural Networks, Vol. 3, No. 1, January 1992, pp.131-138.

- [25] C.A. Balanis: '*Antenna Theory, Analysis and Design*', Harper and Row Publishers, Inc., 1982, pp.457-470.
- [26] V. Galindo and C.P. Wu: '*The Relation Between the Far-Zone Pattern of the Singly Excited Element and the Transmission Coefficient of the Principal Lobe in an Infinite Array*', IEEE Transactions on Antennas & Propagation, May 1966, pp.397-398.
- [27] C.P. Wu and V. Galindo: '*Properties of a Phased Array of Rectangular Waveguides with Thin Walls*', IEEE Transactions on Antennas & Propagation, Vol.AP-14, No.2, March 1966, pp.163-173.
- [28] S. Ramo, J.R. Whinnery, Th. van Duzer: '*Fields and Waves in Communication Electronics*', John Wiley & Sons, 1984, pp.607-610.
- [29] A.C. Ludwig: '*The Definition of Cross Polarisation*', IEEE Transactions on Antennas & Propagation, January 1973, pp.116-119.
- [30] P.W. Hannan: '*The Element-Gain Paradox for a Phased-Array Antenna*', IEEE Transactions on Antennas & Propagation, Vol.AP-12, pp.423-433, July 1964.
- [31] W. Grabherr and W. Menzel: '*A New Transition From Microstrip Line to Rectangular Waveguide*', Conference Proceedings 22nd European Microwave Conference, Helsinki Finland, Vol.2, pp.1170-1175.
- [32] P. Hoogeboom, P.J. Koomen, W.P.M.N. Keizer, M.P.G. Otten, M.H.A. Paquay, H.J. Visser, A.P. de Hek, H. Pouwels, G. van der Burg, H.J. Breeman, P. Snoeij, J.L. Tauritz, A. Vellekoop: '*Definition Study PHARUS: Final Report*', TNO Physics & Electronics Laboratory, Report No. FEL-91-A375, November 1991.
- [33] S. Riegger: '*Telefax Dornier GmbH, Ref: DPA-006-93*', October 4 1993.



G.A. van der Spek  
(Group leader)



H.J. Visser  
(Author)



**APPENDIX A: HELPFUNCTIONS USED IN MATCHING EQUATIONS**

In the determination of the helpfunctions  $F_1$  to  $F_{18}$ , use is made of:

$$NE(n) = 2 \cdot \sin\left(\frac{n}{2}\right) / n \quad (\text{A.1a})$$

$$NC(m, n) = \begin{cases} 1, & m = n = 0 \\ \frac{1}{2}, & m = n \neq 0 \\ 0, & m \neq n \end{cases} \quad (\text{A.1b})$$

$$NS(m, n) = \begin{cases} 0, & m = n = 0 \\ \frac{1}{2}, & m = n \neq 0 \\ 0, & m \neq n \end{cases} \quad (\text{A.1c})$$

$$FCT(m, n) = \pi j J_m\left(\frac{n}{2}\right) / 2 \quad (\text{A.1d})$$

$$FST(m, n) = m\pi J_m\left(\frac{n}{2}\right) / n \quad (\text{A.1e})$$

$$CCT(m, n, \eta) = \begin{cases} \pi \cos\left(\frac{n\pi}{2}\right) J_m\left(\frac{n\eta\pi}{2}\right) / 2; & m = 0, 2, 4, \dots \\ j\pi \sin\left(\frac{n\pi}{2}\right) J_m\left(\frac{n\eta\pi}{2}\right) / 2; & m = 1, 3, 5, \dots \end{cases} \quad (\text{A.1f})$$

$$SST(m, n, \eta) = \begin{cases} -j \left( \frac{m}{n\eta} \right) \cos\left(\frac{n\pi}{2}\right) J_m\left(\frac{n\eta\pi}{2}\right); m = 0, 2, 4, \dots \\ \left( \frac{m}{n\eta} \right) \sin\left(\frac{n\pi}{2}\right) J_m\left(\frac{n\eta\pi}{2}\right); m = 1, 3, 5, \dots \end{cases} \quad (\text{A.1g})$$

With these Bessel function expanded integrals:

$$F_1 = sNE([u_{p'0} - u_{p'0}]s) \quad (\text{A.2a})$$

$$F_2 = t \cdot \sin(\Omega) NE([v_{p'q} - v_{p'q}]t \cdot \sin(\Omega)) \quad (\text{A.2b})$$

$$F_3 = a \cdot NC(m, m') \quad (\text{A.2c})$$

$$F_4 = b \cdot NS(n, n') \quad (\text{A.2d})$$

$$F_5 = a \cdot NS(m, m') \quad (\text{A.2e})$$

$$F_6 = b \cdot NC(n, n') \quad (\text{A.2f})$$

$$F_7 = c \cdot FCT(l, u_{p'0}c) \quad (\text{A.2g})$$

$$F_8 = FCT(w, v_{p'q}d) \quad (\text{A.2h})$$

$$F_9 = c \cdot FST(l, u_{p'0}c) \quad (\text{A.2i})$$

$$F_{10} = d.FCT(w, v_{pq}d) \quad (\text{A.2j})$$

$$F_{11} = c.CCT\left(l, m, \frac{c}{a}\right) \quad (\text{A.2k})$$

$$F_{12} = d.SST\left(w, n, \frac{d}{b}\right) \quad (\text{A.2l})$$

$$F_{13} = c.SST\left(l, m, \frac{c}{a}\right) \quad (\text{A.2m})$$

$$F_{14} = d.CCT\left(w, n, \frac{d}{b}\right) \quad (\text{A.2n})$$

$$F_{15} = c.FST(l, -u_{p0}c) \quad (\text{A.2o})$$

$$F_{16} = d.FCT(w, -v_{pq}d) \quad (\text{A.2p})$$

$$F_{17} = c.FCT(l, -u_{p0}c) \quad (\text{A.2q})$$

$$F_{18} = d.FST(w, -v_{pq}d) \quad (\text{A.2r})$$

and finally:

$$F_1 = s \quad (\text{A.3a})$$



$$F_2 = t \cdot \sin(\Omega) \quad (\text{A.3b})$$

$$F_3 = a\delta_m; \delta_m = \begin{cases} 1; m = 0 \\ \frac{1}{2}; m \neq 0 \end{cases} \quad (\text{A.3c})$$

$$F_4 = b\delta_n; \delta_n = \begin{cases} 0; n = 0 \\ \frac{1}{2}; n \neq 0 \end{cases} \quad (\text{A.3d})$$

$$F_5 = a\delta_m'; \delta_m' = \begin{cases} 0; m = 0 \\ \frac{1}{2}; m \neq 0 \end{cases} \quad (\text{A.3e})$$

$$F_6 = b\delta_n'; \delta_n' = \begin{cases} 1; n = 0 \\ \frac{1}{2}; n \neq 0 \end{cases} \quad (\text{A.3f})$$

$$F_7 = c\pi J_1\left(\frac{u_{p0}c}{2}\right) / 2 \quad (\text{A.3g})$$

$$F_8 = d\omega\pi J_1\left(\frac{v_{pq}d}{2}\right) / v_{pq}d \quad (\text{A.3h})$$

$$F_9 = cl\pi J_1\left(\frac{u_{p0}c}{2}\right) / u_{p0}c \quad (\text{A.3i})$$

$$F_{10} = d\pi J_w \left( \frac{v_{pq}d}{2} \right) / 2 \quad (\text{A.3j})$$

$$F_{11} = \begin{cases} c\pi \cdot \cos\left(\frac{m\pi}{2}\right) J_l \left( \frac{m \frac{c}{a} \pi}{2} \right) / 2; l = 0, 2, 4, \dots \\ jc\pi \cdot \sin\left(\frac{m\pi}{2}\right) J_l \left( \frac{m \frac{c}{a} \pi}{2} \right) / 2; l = 1, 3, 5, \dots \end{cases} \quad (\text{A.3k})$$

$$F_{12} = \begin{cases} -jd \left( \frac{w}{n \frac{d}{b}} \right) \cos\left(\frac{n\pi}{2}\right) J_w \left( \frac{n \frac{d}{b} \pi}{2} \right) / 2; w = 0, 2, 4, \dots \\ d \left( \frac{w}{n \frac{d}{b}} \right) \sin\left(\frac{n\pi}{2}\right) J_w \left( \frac{n \frac{d}{b} \pi}{2} \right) / 2; w = 1, 3, 5, \dots \end{cases} \quad (\text{A.3l})$$

$$F_{13} = \begin{cases} -jc \left( \frac{l}{m \frac{c}{a}} \right) \cos\left(\frac{m\pi}{2}\right) J_l \left( \frac{m \frac{c}{a} \pi}{2} \right) / 2; l = 0, 2, 4, \dots \\ c \left( \frac{l}{m \frac{c}{a}} \right) \sin\left(\frac{m\pi}{2}\right) J_l \left( \frac{m \frac{c}{a} \pi}{2} \right) / 2; l = 1, 3, 5, \dots \end{cases} \quad (\text{A.3m})$$

$$F_{14} = \begin{cases} d\pi \cos\left(\frac{n\pi}{2}\right) J_w \left( \frac{n \frac{d}{b} \pi}{2} \right) / 2; w = 0, 2, 4, \dots \\ jd\pi \sin\left(\frac{n\pi}{2}\right) J_w \left( \frac{n \frac{d}{b} \pi}{2} \right) / 2; w = 1, 3, 5, \dots \end{cases} \quad (\text{A.3n})$$

$$F_{15} = -cl\pi J_l \left( -\frac{u_{p0}c}{2} \right) / u_{p0}c \quad (\text{A.3o})$$

$$F_{16} = d\pi J_w \left( -\frac{v_{p0}d}{2} \right) / 2 \quad (\text{A.3p})$$

$$F_{17} = c\pi J_l \left( -\frac{u_{p0}c}{2} \right) / 2 \quad (\text{A.3q})$$

$$F_{18} = -dw\pi J_n \left( -\frac{v_{pq}d}{2} \right) / v_{pq}d \quad (\text{A.3r})$$

TNO-report

Page  
A.8

---

FEL-94-B062  
Appendix A

## REPORT DOCUMENTATION PAGE (MOD-NL)

<b>1. DEFENCE REPORT NO. (MOD-NL)</b> TD94-0176	<b>2. RECIPIENT'S ACCESSION NO.</b> -	<b>3. PERFORMING ORGANIZATION REPORT NO.</b> FEL-94-B062
<b>4. PROJECT/TASK/WORK UNIT NO.</b> 22448	<b>5. CONTRACT NO.</b> -	<b>6. REPORT DATE</b> February 1994
<b>7. NUMBER OF PAGES</b> 116 (incl. 1 appendix, excl. RDP & distribution list)	<b>8. NUMBER OF REFERENCES</b> 33	<b>9. TYPE OF REPORT AND DATES COVERED</b> -
<b>10. TITLE AND SUBTITLE</b> Analysis & synthesis of (SAR) waveguide phased array antennas (ESA contract no. 10134/93/NL/PB)		
<b>11. AUTHOR(S)</b> H.J. Visser		
<b>12. PERFORMING ORGANIZATION NAME(S) AND ADDRESS(ES)</b> TNO Physics and Electronics Laboratory, P.O. Box 96864, 2509 JG The Hague, The Netherlands Oude Waalsdorperweg 63, The Hague, The Netherlands		
<b>13. SPONSORING AGENCY NAME(S) AND ADDRESS(ES)</b> TNO Physics and Electronics Laboratory, P.O. Box 96864, 2509 JG The Hague, The Netherlands Oude Waalsdorperweg 63, The Hague, The Netherlands		
<b>14. SUPPLEMENTARY NOTES</b> The classification designation Ongerubricenseerd is equivalent to Unclassified, Stg. Confidentieel is equivalent to Confidential and Stg. Geheim is equivalent to Secret.		
<b>15. ABSTRACT (MAXIMUM 200 WORDS (1044 BYTE))</b> <p>This report describes work performed due to ESA contract No. 10134/93/NL/PB. Started is with a literature study on dual polarised waveguide radiators, resulting in the choice for the open ended square waveguide. After a thorough description of the mode matching infinite waveguide array analysis method - including finiteness effects - , that forms the basis for all further described analysis and synthesis methods, the accuracy of the analysis software is validated by comparison with measurements on two realised antennas. These antennas have centred irises in the waveguide apertures and a dielectric wide angle impedance matching sheet in front of the antenna. A synthesis method, using simulated annealing and downhill simplex, is described next and different antenna designs, based on the analysis of a single element in an infinite array environment, are presented. Next, designs of subarrays are presented. Shown is the paramount importance of including the array environment in the design of a subarray. A microstrip patch waveguide exciter and subarray feeding network are discussed and the depth of the waveguide radiator is estimated. Chosen is for the realisation of a rectangular grid array with waveguides of 2.5 cm depth without irises and without dielectric sheet, grouped in linear 8 elements subarrays.</p>		
<b>16. DESCRIPTORS</b> Phased array Synthetic aperture radar Waveguides	<b>IDENTIFIERS</b> -	
<b>17a. SECURITY CLASSIFICATION (OF REPORT)</b> Ongerubricenseerd	<b>17b. SECURITY CLASSIFICATION (OF PAGE)</b> Ongerubricenseerd	<b>17c. SECURITY CLASSIFICATION (OF ABSTRACT)</b> Ongerubricenseerd
<b>18. DISTRIBUTION AVAILABILITY STATEMENT</b> Unlimited Distribution	<b>17d. SECURITY CLASSIFICATION (OF TITLES)</b> Ongerubricenseerd	